Anti-Reflective Dielectric Nanostructures for Solar Cells Analyzed from a Helicity Preservation Perspective

Zur Erlangung des akademischen Grades einer
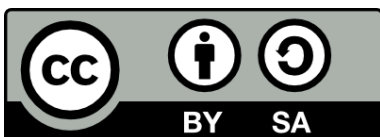Doktorin der Naturwissenschaften
(Dr. rer. nat.)

von der KIT-Fakultät für Physik
des Karlsruher Instituts für Technologie (KIT)

angenommene
DISSERTATION

von

M. Sc. Evgeniia Slivina

Tag der mündlichen Prüfung: 26.11.2021

Referent: Prof. Dr. Carsten Rockstuhl
Korreferent: Tenure-Track-Prof. Dr. Ulrich W. Paetzold

Selbstständigkeitserklärung

Eidesstattliche Versicherung gemäß § 13 Absatz 2 Ziffer 3 der Promotionsordnung des Karlsruher Instituts für Technologie (KIT) für die KIT-Fakultät für Physik:

1. Bei der eingereichten Dissertation zu dem Thema "*Anti-Reflective Dielectric Nanostructures for Solar Cells Analyzed from a Helicity Preservation Perspective*" handelt es sich um meine eigenständig erbrachte Leistung.

2. Ich habe nur die angegebenen Quellen und Hilfsmittel benutzt und mich keiner unzulässigen Hilfe Dritter bedient. Insbesondere habe ich wörtlich oder sinngemäß aus anderen Werken übernommene Inhalte als solche kenntlich gemacht.

3. Die Arbeit oder Teile davon habe ich wie folgt/ bislang nicht* an einer Hochschule des In- oder Auslands als Bestandteil einer Prüfungs- oder Qualifikationsleistung vorgelegt.

    Titel der Arbeit:
    "*Anti-Reflective Dielectric Nanostructures for Solar Cells Analyzed from a Helicity Preservation Perspective*",
    Hochschule und Jahr:
    KIT-Fakultät für Physik des Karlsruher Instituts für Technologie (KIT), 2021,
    Art der Prüfungs- oder Qualifikationsleistung:
    Dissertation.

4. Die Richtigkeit der vorstehenden Erklärungen bestätige ich.

5. Die Bedeutung der eidesstattlichen Versicherung und die strafrechtlichen Folgen einer unrichtigen oder unvollständigen eidesstattlichen Versicherung sind mir bekannt. Ich versichere an Eides statt, dass ich nach bestem Wissen die reine Wahrheit erklärt und nichts verschwiegen habe.

Ort und Datum   Unterschrift

---

*Nicht Zutreffendes streichen. Bei Bejahung sind anzugeben: der Titel der andernorts vorgelegten Arbeit, die Hochschule, das Jahr der Vorlage und die Art der Prüfungs- oder Qualifikationsleistung.

Abstract

Continuing increase of carbon dioxide (CO_2) emissions and subsequent growth of the global average temperature pushes us towards a faster transition from fossil fuels to renewable energy sources. In this respect, photovoltaics (PV) may play a decisive role in achieving net zero CO_2 emissions within the desired time frame. While new PV technologies have been actively researched over recent years, silicon (Si) PV continues to dominate the world market.

Despite the maturity of Si PV, there is still room for improvement. In particular, to keep up with the estimates for the global installed PV capacity for upcoming decades, one has to consider how much energy is actually used for manufacturing Si wafers. Thus, it is feasible to consider a transition to thinner Si absorbers. However, such transition requires adjustments of the industrially accepted processes used to negate optical losses since the standard approach employing random pyramidal textures is no longer feasible for rather thin wafers. Thus, alternative strategies have to be established. For this purpose, nanophotonic structures are of interest. In particular, dielectric scatterers supporting Mie resonances attracted attention from the research community over the last few years.

In this thesis, we perform a holistic study of periodic and disordered anti-reflective (AR) dielectric nanostructures applied to crystalline silicon (c-Si) heterojunction (HJT) solar cells. We optimize the optical performance of these systems and show that the AR properties of the nanostructure arrays on top of solar cell stacks are related to two requirements: a sufficiently high degree of discrete rotational symmetry of an array and the ability to preserve helicity of the incident illumination. For a periodic system, the first condition can be readily met. The second condition generally requires the system to be made from materials with an equal electric permittivity and magnetic permeability. Since this is unfeasible with naturally available materials, this condition has to be relaxed. Indeed, similar effects can be achieved if only the electric and magnetic response from the photonic nanostructure is balanced. This balance is accomplished by tuning the geometrical parameters of scatterers made from high index materials. For a disordered system, the helicity preservation condition can be reduced similarly to a periodic system. However, in such a system, the first condition is not exactly applicable. Luckily, the disorder can be tailored such that it becomes stealthy hyperuniform, and large-scale density fluctuations are suppressed. Such tailored disordered patterns are fully isotropic, thus possessing effective continuous rotational symmetry. Therefore, the AR properties of these systems are also related to the requirements stated above.

Furthermore, we fabricate solar cells coated with periodic and tailored disordered nanodisks based on the optimal designs. We characterize the optical and electrical properties of the samples and observe the improvement of the AR properties and subsequent positive influence on the short-circuit current density. A complementary analysis of the annual energy yield of the solar modules employing solar cells with nanodisk coatings shows that our designs can potentially be integrated into the module with their positive effect preserved.

Contents

List of Figures

List of Tables

List of Acronyms

a-Si:H(n^+) .... n-doped hydrogenated amorphous silicon
a-Si:H(p^+) .... p-doped hydrogenated amorphous silicon
a-Si:H(i) .... Intrinsic hydrogenated amorphous silicon
ALD .... Atomic layer deposition
AM .... Air mass
AM0 .... Irradiance outside earth's atmosphere
AM1.5G .... Air mass 1.5 global tilted irradiance
AR .... Anti-reflective
ARC .... Anti-reflective coating
ARS .... Angular resolved scattering
c-Si .... Crystalline silicon
CCD .... Charge-coupled device
DARC .... Double anti-reflective coating
e-beam .... Electron beam (lithography)
EQE .... External quantum efficiency
EVA .... Ethylene-vinyl acetate
EY .... Energy yield
FDFD .... Finite-difference frequency-domain
FDTD .... Finite-difference time-domain (method)
FEM .... Finite element method
FIB .... Focused ion beam
HJT .... Heterojunction
I-V .... Current-voltage (characteristic)
IQE .... Internal quantum efficiency
ITO .... Indium tin oxide
LCPR .... Localized surface plasmon resonance
LED .... Light-emitting diode
LT .... Light trapping
MPP .... Maximum power point
nc-Si:H .... Hydrogenated nanocrystalline silicon
PCE .... Power conversion efficiency
PECVD .... Plasma-enhanced chemical vapor deposition
PL .... Photoluminescence
PML .... Perfectly matched layer
PMMA .... Poly(methyl methacrylate)
PV .... Photovoltaics
PVD .... Physical vapor deposition
RIE .... Reactive-ion etching
RSA .... Random sequential adsorption
SEM .... Scanning electron microscopy
STC .... Standard test conditions

List of publications and conference contributions

Publications in peer review journals

1. P. M. Piechulla[†], **E. Slivina**[†], D. Bätzner, I. Fernandez-Corbaton, P. Dhawan, R. B. Wehrspohn, A. N. Sprafke, and C. Rockstuhl, "Anti-reflective Huygens' meta-surface with correlated disorder made from high-index disks implemented into silicon heterojunction solar cells", *ACS Photonics*, vol. 8, no. 12, pp. 3476–3485, 2021, Available online: ACS Articles on Request link.

2. **E. Slivina**, D. Bätzner, R. Schmager, M. Langenhorst, J. Lehr, U. W. Paetzold, U. Lemmer and C. Rockstuhl, "Annual energy yield of mono- and bifacial silicon heterojunction solar modules with high-index dielectric nanodisk arrays as anti-reflective and light trapping structures", *Optics Express*, vol. 29, no. 21, pp. 34 494–34 509, 2021.

3. P. M. Piechulla, B. Fuhrmann, **E. Slivina**, C. Rockstuhl, R. B. Wehrspohn, and A. N. Sprafke, "Tailored light scattering through hyperuniform disorder in self-organized arrays of high-index nanodisks", *Advanced Optical Materials*, vol. 9, no. 17, p. 2 100 186, 2021.

4. M. I. Abdelrahman, **E. Slivina**, C. Rockstuhl, and I. Fernandez-Corbaton, "Effects of symmetry-breaking on electromagnetic backscattering", *Scientific Reports*, vol. 11, no. 1721, pp. 1–8, 2021.

5. **E. Slivina**, A. Abass, D. Bätzner, B. Strahm, C. Rockstuhl, and I. Fernandez-Corbaton, "Insights into Backscattering Suppression in Solar Cells from the Helicity-Preservation Point of View", *Physical Review Applied*, vol. 12, no. 5, p. 054 003, 2019.

Talks given at the international conferences

1. P. Piechulla, **E. Slivina**, D. Bätzner, I. Fernandez-Corbaton, R. B. Wehrspohn, A. Sprafke, and C. Rockstuhl, "Nearly-hyperuniform anti-reflection coatings made from high-index nanodisks for silicon heterojunction solar cells", OSA Advanced Photonics Congress, online conference, 26-30 July 2021.

2. **E. Slivina**, A. Abass, D. Bätzner, B. Strahm, C. Rockstuhl, and I. Fernandez-Corbaton, "Revisiting broadband reflection suppression by Mie scatterers: the role of electromagnetic duality", *OSA Optics and Photonics for Energy and Environment Congress*, Sentosa Island, Singapore, 5-8 November 2018.

3. **E. Slivina**, A. Abass, D. Bätzner, B. Strahm, C. Rockstuhl, and I. Fernandez-Corbaton, "Insights into Broadband Backscattering Suppression in Solar Cells from the Duality Point of View", *Metamaterials*, Espoo, Finland, 27 August-1 September 2018.

[†]Both authors contributed equally to this work.

1. Introduction

Over the last years, humankind has taken steps towards reducing carbon dioxide (CO_2) emissions and continues to shift towards replacing fossil fuels as a primary energy source. Since 2015, when the Paris agreement was adopted [1], the greenhouse effect has become more prominent on the world's agenda. While the Intergovernmental Panel on Climate Change has already published an analysis forecasting a disconcerting future for our planet a few years ago [2], their most recent report attracted a lot of attention [3].

Experts from various fields presented a few emissions scenarios for the following decades. The most optimistic case relies on the eradication of CO_2 emissions by 2050. Even then, the global average temperature will rise by 1.5 °C by 2040 and stop growing after 2050. Moreover, the ocean level will continue to rise, and natural disasters will occur more frequently. At this point, the question of inevitable depleting fossil fuel reserves comes to the background, and tackling the energy issue becomes a race against time concerning our future on this planet. In light of these facts, further development and spread of alternative energy sources such as wind and solar become even more urgent.

Solar energy will potentially play a decisive role in achieving the objectives dictated by a net zero emissions scenario since sunlight provides more power when compared to what is consumed worldwide. High reliance on this energy source is due to its omnipresent nature and predictability. In recent years, the manufacturing costs of solar modules have been steadily decreasing. Additionally, global installed solar photovoltaic (PV) capacity has exceeded 750 GW by the end of 2020 [4]. Even after Covid-19 exerted pressure on the world economies, the aforementioned capacity indicates that envisioned future with around 10 TW of PV by 2030 and 30 to 70 TW by 2050 [5] is in the realm of what is possible.

While a few third-generation PV technologies such as dye-sensitized [6], organic [7], and perovskite solar cells [8] are actively investigated and developed, silicon (Si) solar cells and modules continue to dominate the world market. Out of these alternatives, the most promising is the utilization of perovskites, which in combination with Si cells in tandem devices can potentially increase the power conversion efficiency (PCE) up to around 25%-30% and may soon be industrialized [9–11]. Already in 2018, Oxford PV demonstrated a perovskite-silicon tandem cell certified by the National Renewable Energy Laboratory, surpassing all previous Si efficiency records, with a PCE of 28% [12]. However, despite this promising increase of the PCE, there is a long way for such tandem devices to reach the maturity of Si PV.

There are a few reasons why Si continues to be a dominant material for the production of PV devices. First of all, Si is the second most abundant element on earth. Moreover, its physics and chemistry are well understood, and Si does not present potential health hazards. Furthermore, Si PV modules have a decent life expectancy, with warranties lasting longer than two decades. However, Si, which occurs in nature, is found either as impure, oxidized sand, or silicates. Thus, processes to purify and crystallize Si are unavoidable [13]. Not only are the approaches used in industry for these processes

complex and costly, but they are also polluting and energy-consuming. Therefore, in conjunction with the growing global installed PV capacity, continuous technological developments are required to tackle continuously arising resource constraints [14]. A path to circumvent this drawback of Si PV technology is to eliminate the deficiencies in the current chemistry used to transform Si found in nature to the form suitable for industrial applications. Additionally, it is natural to use thinner wafers to reduce Si consumption to optimize Si PV technology further. On top of the apparent advantage of reducing energy loss and pollution during the processing of the raw materials, recent studies show that the employment of thinner Si wafers can have an additional positive economic effect by further decreasing the manufacturing costs [15]. Moreover, thin absorbers are attractive for flexible devices and the boost of thin PV technology in general.

In this thesis, we will focus on crystalline silicon (c-Si) PV. Efficient light coupling between a solar cell and the surrounding medium is crucial for maximizing overall device performance. This is an especially relevant issue for c-Si solar cells, for which the discontinuity of the permittivity from air (or encapsulation on the solar module level) to c-Si causes critical reflection losses. Optical losses remain one of the principal causes preventing c-Si PV technology from reaching the detailed-balance limit [16, 17], defining the ceiling for achievable solar cell PCE. The current record for c-Si solar cells stands at 26.7 % with an upper limit of around 29 % [18]. State-of-the-art c-Si solar cells rely on micron-sized pyramidal textures [19–21] in combination with flat anti-reflective coatings (ARC). On the industrial scale, these textures are realized for wafers with thicknesses larger than 150 μm [22]. However, a transition to the absorber thicknesses below the standard values and switching to the foil-like c-Si PV will require the development of novel processes to negate optical losses. This demand for alternative solutions is caused by the increasingly challenging texturing of the c-Si wafers due to handling issues upon thickness reduction.

While textures comprising small pyramidal structures for thin c-Si wafers are an active area of research [23–25], the emerging novel processes are yet to advance to the industrial scale. Nanophotonics is another approach in response to the need to negate optical losses when the established processes no longer apply. A plethora of nanophotonic concepts have been suggested in recent years not only to improve light in-coupling on the front solar cell interface and optimize light trapping (LT) but for a more comprehensive range of objectives, including colored photovoltaics and spectrum splitting in tandem devices. [26–28].

In this thesis, we will primarily concentrate on nanophotonic structures designed to improve the solar cells' anti-reflective (AR) properties. For example, periodically arranged silicon sub-wavelength structures were investigated for this purpose, including nanospheres, nanowires, and nanopillars [29–31], and randomly arranged structures like black silicon [32]. These designs essentially propose alternative structuring to industrially accepted chemistry but with individual feature sizes smaller than the incident wavelength. Moreover, the proposed designs included nanostructure gratings on either side of the solar cell, contributing to the overall improved light harvesting in the absorber layer. For example, such a concept with two gratings was proposed for thin-film c-Si [33] and thin-film hydrogenated nanocrystalline silicon (nc-Si:H) [34] solar cells stacks. In these two designs, the AR and LT properties were decoupled, where the front grating served to improve light in-coupling, and the rear grating ensured efficient trapping of the photons that were not lost due to reflectance.

Another group of proposed nanophotonic elements for improving AR properties of solar cells is plasmonic nanostructures. These designs rely on metallic structures of spherical or hemispherical shape, e.g., silver or gold, or the structured absorber/metal interfaces

so that they sustain localized surface plasmon resonances (LSPR). The works suggesting designs of plasmonic nanoparticles for improvement of AR and LT properties include [29, 35–38]. However, such metallic nanophotonic structures introduce additional parasitic absorption in the solar cells, partially counteracting their positive influence on the optical performance of a given design [39].

Finally, dielectric structures were extensively investigated in recent years since they do not involve metals and can be applied to any material possessing high refractive index [40–47]. Such nanoparticles act like Mie scatterers and enhance absorption over a broad spectral range due to the preferential scattering of light towards the solar cell substrate. While suggested designs employed nanoparticles of different shapes including nanocones [47] and nanospheres [48], nanodisks attracted special interest [42, 43, 49, 50]. Such preference was dictated not only by the ability of such disks to efficiently direct light towards the absorber over the broad spectral range but also by the feasibility of their fabrication. Titanium dioxide (TiO_2), in particular, was frequently used for some of the mentioned designs since this dielectric material possesses a high refractive index in the spectral region relevant for solar cell application and does not introduce strong parasitic absorption. We note that our choice also fell on TiO_2 as the nanostructure material.

A critical question is *what one can add to already existing knowledge when it comes to the improvement of the AR properties of solar cells when employing dielectric nanostructures?*

Initially, the preferential scattering of the dielectric nanostructures towards the solar cell absorber was mainly attributed to their high refractive index and ability to support multipolar Mie resonances [41]. In this thesis, we will analyze the superior AR properties of dielectric nanostructures from another perspective, which relies on the notion of helicity preservation, i.e., on the ability of the system to preserve the handedness of the incident illumination. We will show that the AR properties of the nanostructure arrays on top of solar cell stacks are related to two conditions: A sufficiently high degree of discrete rotational symmetry of an array and the ability to preserve helicity of the incident illumination. With these two requirements strictly satisfied, the system will exhibit zero backscattering. As we will see later in this thesis, it is impossible to achieve perfect helicity preservation for natural materials in a broad spectral range since it requires the system to be electromagnetically dual (i.e., from the perspective of material, it requires it to have an equal electric permittivity and magnetic permeability). However, the aforementioned multipolar resonances occurring in dielectric sub-wavelength nanostructures help to relax the helicity preservation condition. We will demonstrate that satisfying both symmetry and relaxed helicity conservation requirements allows for broadband backscattering suppression, and these conditions can provide guidelines for future designs of ARCs for solar cell applications.

Furthermore, we will consider two very similar types of systems, albeit with one crucial difference: We will look at the nanostructures' periodic and disordered arrangements. While for the former, respecting the symmetry requirement is trivial when considering a rotationally symmetric individual nanoscatterer, for the latter, the disorder has to be tailored appropriately. We will analyze both these systems from a helicity preservation point of view and draw a parallel between their responses. Our approach relying on the combination of symmetry requirement and helicity is also general. Thus, it makes these two conditions helpful in understanding several apparently different techniques employed to achieve optimal AR properties in solar cells, including pyramidal textures and graded-index layers.

Next, we will discuss experimental results involving both periodic and tailored disordered nanodisks' arrangements. The fabrication techniques we will employ for depositing the optimized nanostructures are quite different, starting from the requirement of special

treatment of the substrate and up to a deposition technique employed to apply the TiO_2 layer from which the nanostructures are made. We will analyze both the optical and electrical properties of the fabricated samples and see which fabrication approach is more feasible for practical application.

Finally, for the periodically arranged nanostructures', we will also analyze their behavior on the solar module level under realistic irradiation conditions by calculating the annual energy yield (EY). This allows us to see whether introducing encapsulation preserves the positive effect of the nanodisk grating.

To make our study holistic, we will discuss the same solar cell stack throughout the thesis. We consider a c-Si-based heterojunction (HJT) rear emitter solar cell stack. We employ nanodisks as dielectric AR nanoscatterers, which are made of TiO_2. It is important to note that the considered system is exemplary, and the design guidelines based on the notion of helicity preservation are not restricted to a particular solar cell stack or the materials involved.

Structure of the thesis

The thesis consists of six chapters. After an introduction, these chapters will follow:

- **Chapter 2** provides the theoretical background needed to put in context the subsequent chapters discussing obtained results. This chapter consists of three main parts. The first part starts with Maxwell's equations and basic electromagnetic theory and continues with the introduction of the helicity operator and the role of discrete rotational symmetry in backscattering suppression. The second part gives the overview of the basic solar cell concepts, focusing on the technology relevant for this thesis – c-Si HJT solar cells. Finally, the third part introduces the reader to the numerical methods employed throughout the thesis, focusing on the extensively used finite element method (FEM).

- **Chapter 3** discusses the AR properties of the periodically arranged nanodisks placed on top of a c-Si HJT solar cell stack. This chapter will first consider a hypothetical (electromagnetically dual) layer stack coated with a square nanodisk grating. For such a system, we will demonstrate the importance of both conditions needed for zero backscattering by gradually breaking its duality and discrete rotational symmetry. Next, we will take the system with the same geometrical parameters but assign realistic material properties to each layer and the nanodisks. This realistic system will correspond to a c-Si HJT solar cell stack coated by TiO_2 nanodisks. We will further optimize this system concerning its AR properties and discuss its optical performance with respect to its ability to preserve helicity. Additionally, we will analyze the scattering properties of an individual nanodisk on top of the same layer stack and see how a further increase of the array symmetry influences the system's AR properties. Finally, we will discuss the fabrication of the optimal system employing electron beam (e-beam) lithography and its subsequent characterization.

- **Chapter 4** continues with a discussion of the system containing periodically arranged nanodisks. Here, we will consider the complete solar module architecture. For this, the nanodisk array will be reoptimized concerning the new surrounding medium, i.e., the encapsulation material. We will introduce the periodic gratings for both front and rear solar cell-encapsulation interfaces. The former is designed to improve the AR properties and the latter – the LT properties of the solar module architecture. After analyzing the optical performance at these interfaces, we will calculate the annual EY of mono- and bifacial solar module architectures for a few locations with different climate conditions. We will compare their power output to

both optimized flat and state-of-the-art reference modules employing textured c-Si wafers.

- **Chapter 5** discusses the AR properties of the tailored disordered nanodisk arrangement placed on top of a c-Si HJT solar cell stack. Here, we will employ a scalable colloid-based nanofabrication method. The design of this nanodisk ARC is inspired by the results obtained in chapter 2. To approximately calculate reflectance of the system, we will employ the first Born approximation and compare the simulated reflectance spectrum with a measured one. Additionally, we will analyze the backscattering properties from a helicity preservation point of view and compare the results with the output from a system with periodically arranged nanodisks. Finally, we will study the influence of the fabrication process on the opto-electronic properties of the cells by characterizing the best sample and comparing it with the response of the untreated solar cell.

- **Chapter 6** is dedicated to conclusions and outlook, where we summarize the results obtained during this doctoral project and discuss possible extensions of this work, giving several perspective paths for further research.

2. Theoretical Background and Computational Methods

This chapter aims to introduce the essential theoretical concepts employed in this thesis, as well as computational techniques used to generate the results. The theoretical aspects discussed in this chapter are divided into two main sections. Section 2.1 is focused on electromagnetic field theory. While starting from the equations describing light propagation in the homogeneous media, it leads to the symmetry of those equations under duality transformation and its generator – helicity. In Sec. 2.2, the working principle and properties of a solar cell and the features of the solar cell stack studied throughout this thesis – silicon-based heterojunction technology (HJT) solar cell – are discussed. Section 2.3 covers the computational tools used in this thesis. Sec. 2.3.1 describes the finite element method (FEM) and its steps, and Sec. 2.3.2 introduces the energy yield methodology framework employed for the calculations in chapter 4. Finally, Sec. 2.3.3 briefly discusses the finite-difference time-domain method (FDTD) which is employed in chapter 5.

2.1 Electromagnetic field theory and duality symmetry

In this section, we start with Maxwell's equations governing light-matter interaction and their fundamental solutions. Next, the reflectance and transmittance of light at the interface between two media is discussed. The angular spectrum representation is also introduced as a tool frequently used within this thesis. Finally, the concepts of electromagnetic duality symmetry and helicity are introduced while those are central to the discussions, which will follow in the other chapters.

2.1.1 Maxwell's equations and Poynting's theorem

To describe the propagation of electromagnetic waves through a medium, we introduce the set of Maxwell's equations in their macroscopic formulation. These four equations show the relationship between electric and magnetic fields, and for a homogeneous medium in the space-time domain, they read [51]

$$\nabla \cdot \mathbf{D}(\mathbf{r}, t) = \rho(\mathbf{r}, t), \tag{2.1}$$

$$\nabla \times \mathbf{E}(\mathbf{r}, t) = -\frac{\partial \mathbf{B}(\mathbf{r}, t)}{\partial t}, \tag{2.2}$$

$$\nabla \cdot \mathbf{B}(\mathbf{r}, t) = 0, \tag{2.3}$$

$$\nabla \times \mathbf{H}(\mathbf{r}, t) = \frac{\partial \mathbf{D}(\mathbf{r}, t)}{\partial t} + \mathbf{J}(\mathbf{r}, t). \tag{2.4}$$

In Eqns. 2.1-2.4, $\mathbf{E}(\mathbf{r}, t)$ and $\mathbf{H}(\mathbf{r}, t)$ are the electric and magnetic fields, $\mathbf{D}(\mathbf{r}, t)$ is the electric displacement, $\mathbf{B}(\mathbf{r}, t)$ is the magnetic flux density, and $\rho(\mathbf{r}, t)$ and $\mathbf{J}(\mathbf{r}, t)$ are charge and current densities, respectively. We complete this system of equations by adding the constitutive relations that link the electric field and magnetic field, as well as the electric

displacement and magnetic flux, and in case of frequency domain are given by

$$\mathbf{D}(\mathbf{r}, t) = \varepsilon_0 \mathbf{E}(\mathbf{r}, t) + \mathbf{P}(\mathbf{r}, t) \tag{2.5}$$

$$\mathbf{B}(\mathbf{r}, t) = \mu_0 \left(\mathbf{H}(\mathbf{r}, t) + \mathbf{M}(\mathbf{r}, t) \right), \tag{2.6}$$

where $\mathbf{P}(\mathbf{r}, t)$ denotes the polarization, $\mathbf{M}(\mathbf{r}, t)$ the magnetization, and ε_0, μ_0 the electric permittivity and magnetic permeability of vacuum.

To switch to a space-frequency domain, one has to consider Fourier transformed fields

$$\mathbf{E}(\mathbf{r}, t) = \int_{-\infty}^{+\infty} \tilde{\mathbf{E}}(\mathbf{r}, \omega) e^{-i\omega t} d\omega. \tag{2.7}$$

Then, Maxwell's equations in the frequency domain read as

$$\nabla \cdot \tilde{\mathbf{D}}(\mathbf{r}, \omega) = \tilde{\rho}(\mathbf{r}, \omega), \tag{2.8}$$

$$\nabla \times \tilde{\mathbf{E}}(\mathbf{r}, \omega) = i\omega \tilde{\mathbf{B}}(\mathbf{r}, \omega), \tag{2.9}$$

$$\nabla \cdot \tilde{\mathbf{B}}(\mathbf{r}, \omega) = 0, \tag{2.10}$$

$$\nabla \times \tilde{\mathbf{H}}(\mathbf{r}, \omega) = -i\omega \tilde{\mathbf{D}}(\mathbf{r}, \omega) + \tilde{\mathbf{J}}(\mathbf{r}, \omega). \tag{2.11}$$

Transformation to the space-frequency domain simplifies the constitutive relations. For linear, isotropic, dispersive, and local media they are given by

$$\tilde{\mathbf{D}}(\mathbf{r}, \omega) = \varepsilon_0 \varepsilon_r(\mathbf{r}, \omega) \tilde{\mathbf{E}}(\mathbf{r}, \omega), \tag{2.12}$$

$$\tilde{\mathbf{B}}(\mathbf{r}, \omega) = \mu_0 \mu_r(\mathbf{r}, \omega) \tilde{\mathbf{H}}(\mathbf{r}, \omega), \tag{2.13}$$

where ε_r and μ_r are the relative permittivity and permeability, respectively.

For a homogeneous medium and in the absence of free electric charges and currents, one can derive the Helmholtz wave equations by combining Maxwell's equations with constitutive relations. Such wave equations for electric and magnetic fields will read as

$$\nabla^2 \tilde{\mathbf{E}}(\mathbf{r}, \omega) + k^2(\omega) \tilde{\mathbf{E}}(\mathbf{r}, \omega) = 0, \tag{2.14}$$

$$\nabla^2 \tilde{\mathbf{H}}(\mathbf{r}, \omega) + k^2(\omega) \tilde{\mathbf{H}}(\mathbf{r}, \omega) = 0, \tag{2.15}$$

where, in the case of a non-magnetic medium, the wave number k is given by

$$k(\omega) = \omega \sqrt{\varepsilon(\omega)\mu(\omega)} = \omega \sqrt{\varepsilon_0 \mu_0 \varepsilon_r(\omega)\mu_r(\omega)} \overset{\mu_r=1}{=} \frac{\omega}{c} \sqrt{\varepsilon_r(\omega)} = \frac{\omega}{c} \underline{n}(\omega). \tag{2.16}$$

Here, the complex refractive index $\underline{n}(\omega)$ is defined as

$$\underline{n}(\omega) = n(\omega) + i\kappa(\omega), \tag{2.17}$$

where a real part denotes the refractive index $n(\omega)$, and an imaginary part – the extinction coefficient $\kappa(\omega)$, which is non-zero for absorbing media. The plane wave solutions of Eqns. 2.14 and 2.15 are given by:

$$\tilde{\mathbf{E}}(\mathbf{r}, \omega) = \mathbf{E}_0(\mathbf{k}, \omega) e^{i\mathbf{k}\mathbf{r}}, \tag{2.18}$$

$$\tilde{\mathbf{H}}(\mathbf{r}, \omega) = \mathbf{H}_0(\mathbf{k}, \omega) e^{i\mathbf{k}\mathbf{r}}, \tag{2.19}$$

with $\mathbf{k}$ denoting the wave vector, and $\mathbf{E}_0(\mathbf{k}, \omega)$ and $\mathbf{H}_0(\mathbf{k}, \omega)$ denoting the field amplitudes. The general solutions of the Helmholtz equations can be obtained via linear superposition of such plane waves.

Although Maxwell's equations describe the behavior of electric and magnetic fields, they do not give any information regarding energy contained in the system. Poynting's theorem resolves this issue and establishes the relation of electromagnetic field and energy stored in it. If from the scalar product of $\mathbf{H}(\mathbf{r}, t)$ with Eq. 2.2 we subtract the scalar product of $\mathbf{E}(\mathbf{r}, t)$ with Eq. 2.4, we will get the following equation:

$$
\begin{aligned}
\mathbf{H}(\mathbf{r}, t) \cdot [\nabla \times \mathbf{E}(\mathbf{r}, t)] - \mathbf{E}(\mathbf{r}, t) \cdot [\nabla \times \mathbf{H}(\mathbf{r}, t)] = \nabla \cdot [\mathbf{E}(\mathbf{r}, t) \times \mathbf{H}(\mathbf{r}, t)] = \\
-\mathbf{H}(\mathbf{r}, t) \cdot \frac{\partial \mathbf{B}(\mathbf{r}, t)}{\partial t} - \mathbf{E}(\mathbf{r}, t) \cdot \frac{\partial \mathbf{D}(\mathbf{r}, t)}{\partial t} - \mathbf{J}(\mathbf{r}, t) \cdot \mathbf{E}(\mathbf{r}, t).
\end{aligned}
\tag{2.20}
$$

If we combine the above equation with the constitutive relations given in Eqs. 2.5 and 2.6, we will arrive at the following expression:

$$
\begin{aligned}
\nabla \cdot [\mathbf{E}(\mathbf{r}, t) \times \mathbf{H}(\mathbf{r}, t)] + \frac{1}{2} \frac{\partial}{\partial t} [\mathbf{D}(\mathbf{r}, t) \cdot \mathbf{E}(\mathbf{r}, t) + \mathbf{B}(\mathbf{r}, t) \cdot \mathbf{H}(\mathbf{r}, t)] = -\mathbf{J}(\mathbf{r}, t) \cdot \mathbf{E}(\mathbf{r}, t) \\
-\frac{1}{2} \left[\mathbf{E}(\mathbf{r}, t) \cdot \frac{\partial \mathbf{P}(\mathbf{r}, t)}{\partial t} - \mathbf{P}(\mathbf{r}, t) \cdot \frac{\partial \mathbf{E}(\mathbf{r}, t)}{\partial t} \right] - \frac{\mu_0}{2} \left[\mathbf{H}(\mathbf{r}, t) \cdot \frac{\partial \mathbf{B}(\mathbf{r}, t)}{\partial t} - \mathbf{M}(\mathbf{r}, t) \cdot \frac{\partial \mathbf{H}(\mathbf{r}, t)}{\partial t} \right].
\end{aligned}
\tag{2.21}
$$

Let us now integrate both sides of this equation and apply Gauss's theorem. For a linear and non-dispersive medium the terms containing $\mathbf{P}(\mathbf{r}, t)$ and $\mathbf{M}(\mathbf{r}, t)$ and their derivatives will vanish, and we will have [52]:

$$
\begin{aligned}
\int_{\partial V} \mathbf{E}(\mathbf{r}, t) \times \mathbf{H}(\mathbf{r}, t) \, d\mathbf{A} + \frac{1}{2} \frac{\partial}{\partial t} \int_{V} [\mathbf{D}(\mathbf{r}, t) \cdot \mathbf{E}(\mathbf{r}, t) + \mathbf{B}(\mathbf{r}, t) \cdot \mathbf{H}(\mathbf{r}, t)] \, dV = \\
-\int_{V} \mathbf{J}(\mathbf{r}, t) \cdot \mathbf{E}(\mathbf{r}, t) \, dV,
\end{aligned}
\tag{2.22}
$$

where the integrand in the first term on the left side of the equation gives the Poynting's vector, representing the energy flux density

$$
\mathbf{S}(\mathbf{r}, t) = \mathbf{E}(\mathbf{r}, t) \times \mathbf{H}(\mathbf{r}, t),
\tag{2.23}
$$

the integrand in the second term gives the electromagnetic energy density

$$
u = \frac{1}{2} \left(\mathbf{D}(\mathbf{r}, t) \cdot \mathbf{E}(\mathbf{r}, t) + \mathbf{B}(\mathbf{r}, t) \cdot \mathbf{H}(\mathbf{r}, t) \right),
\tag{2.24}
$$

and the term on the right side gives the rate of energy dissipation in the volume V. If we now consider the time-harmonic fields, the time average of Eq. 2.22 will yield

$$
\int_{\partial V} \langle \mathbf{S}(\mathbf{r}) \rangle \, d\mathbf{A} = -\frac{1}{2} \int_{V} \Re\{\mathbf{J}^*(\mathbf{r}) \cdot \mathbf{E}(\mathbf{r})\} \, dV,
\tag{2.25}
$$

which establishes Poynting's theorem with the time-average of the Poynting vector $\langle \mathbf{S} \rangle$ given by

$$
\langle \mathbf{S}(\mathbf{r}) \rangle = \frac{1}{2} \Re\{\mathbf{E}(\mathbf{r}) \times \mathbf{H}^*(\mathbf{r})\}.
\tag{2.26}
$$

2.1.2 Fresnel equations for interfaces

Let us now consider a plane wave impinging on an interface between two homogeneous, isotropic, and non-magnetic media. When such a wave is incident on the media having different optical properties, it is split in a transmitted plane wave, propagating in the second medium, and reflected plane wave, which is propagating back into the first medium. Since an arbitrarily polarized plane wave can be decomposed into two
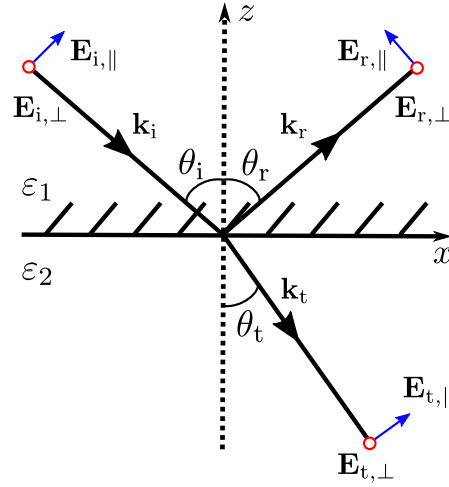
FIGURE 2.1: Illustration of an electromagnetic wave with wave vector $\mathbf{k}_i$ impinging on an interface between two media with permittivities ε_1 and ε_2. The interface lies in x-y-plane. The parallel component of the incident plane wave $\mathbf{E}_{i,\parallel}$ lies in the x-z-plane (plane of incidence), and the perpendicular component $\mathbf{E}_{i,\perp}$ lies in the x-y-plane. $\mathbf{E}_{\{r,t\},\parallel}$ and $\mathbf{E}_{\{r,t\},\perp}$ correspond to parallel and perpendicular components of reflected and transmitted fields, respectively.

orthogonally polarized plane waves, we can choose these polarizations to be parallel and perpendicular to the plane of incidence, such that $\mathbf{E}_i = \mathbf{E}_{i,\parallel} + \mathbf{E}_{i,\perp}$ (see Fig. 2.1). These polarization components are usually referred to as parallel component p or "transverse magnetic" (TM), and perpendicular component s or "transverse electric" (TE). Then, if we consider the amplitudes of the electric fields, we can derive the following relations for the interfaces:

$$E_{r,\perp} = r_s E_{i,\perp}, \qquad E_{r,\parallel} = r_p E_{i,\parallel}, \tag{2.27}$$

$$E_{t,\perp} = t_s E_{i,\perp}, \qquad E_{t,\parallel} = t_p E_{i,\parallel}, \tag{2.28}$$

where the reflection and transmission Fresnel coefficients for both p- and s-polarized plane waves are given by [53]:

$$
\begin{aligned}
r_s &= \frac{\underline{n}_1 \cos\theta_i - \underline{n}_2 \cos\theta_t}{\underline{n}_1 \cos\theta_i + \underline{n}_2 \cos\theta_t}, \\
r_p &= \frac{\underline{n}_2 \cos\theta_i - \underline{n}_1 \cos\theta_t}{\underline{n}_2 \cos\theta_i + \underline{n}_1 \cos\theta_t},
\end{aligned}
\tag{2.29}
$$

$$
\begin{aligned}
t_s &= \frac{2\underline{n}_1 \cos\theta_i}{\underline{n}_1 \cos\theta_i + \underline{n}_2 \cos\theta_t}, \\
t_p &= \frac{2\underline{n}_1 \cos\theta_i}{\underline{n}_2 \cos\theta_i + \underline{n}_1 \cos\theta_t}.
\end{aligned}
\tag{2.30}
$$

In the equations above, the refractive index $\underline{n}$ is defined in Eq. 2.17, and θ_i and θ_i are the incident angle and angle of refraction, respectively (Fig. 2.1). From these coefficients, reflectance and transmittance for both polarizations read as

$$R_{s,p} = |r_{s,p}|^2, \tag{2.31}$$

$$T_{s,p} = \Re\left\{\frac{\underline{n}_2 \cos\theta_t}{\underline{n}_1 \cos\theta_i}\right\} |t_{s,p}|^2, \tag{2.32}$$

and for a non-absorbing media the following equality holds:

$$R_{s,p} + T_{s,p} = 1. \tag{2.33}$$

The relation between the angle of incidence and angle of refraction (transmission angle) is defined by Snell's law, and for a non-absorbing medium, it reads as

$$\frac{\sin \theta_i}{\sin \theta_t} = \frac{n_2}{n_1}. \tag{2.34}$$

If $n_2 > n_1$, there is a real transmission angle θ_t for every angle of incidence θ_i. However, if the first medium is optically denser than the second, and $\theta_t = 90°$, the light will emerge in the direction tangent to the boundary between the media, and the corresponding critical angle of incidence θ_c is defined as

$$\frac{n_2}{n_1} < 1, \rightarrow \theta_c = \arcsin\left(\frac{n_2}{n_1}\right). \tag{2.35}$$

When the incidence angle is larger than θ_c, the incident wave will be fully reflected back into the first medium, and total reflection will occur.

2.1.3 Angular spectrum representation

Plane waves can be employed for the expansion of the electromagnetic field in scattering problems. One way to expand the field into plane waves is via the angular spectrum representation. We note that this method is applicable for the expansion of the fields in a homogeneous medium. It essentially starts with a Fourier expansion of an arbitrary field in terms of the plane and evanescent waves in a given plane. Let us consider an electric field $\mathbf{E}(x, y, z)$ originating from an object (for example, after being scattered). If we consider the field to propagate in principle into the +z-direction and know the field in a plane $z = 0$ which is transverse to the chosen axis, the two-dimensional Fourier transform of the field $\mathbf{E}(x, y, 0)$ will yield [52]

$$\tilde{\mathbf{E}}\left(k_x, k_y; 0\right) = \frac{1}{4\pi^2} \int\limits_{-\infty}^{+\infty} \int\limits_{-\infty}^{+\infty} \mathbf{E}\left(x, y, 0\right) e^{-i\left(k_x x + k_y y\right)} dx\, dy, \tag{2.36}$$

and an inverse Fourier transform will give the electric field in real space:

$$\mathbf{E}\left(x, y, 0\right) = \int\limits_{-\infty}^{+\infty} \int\limits_{-\infty}^{+\infty} \tilde{\mathbf{E}}\left(k_x, k_y; 0\right) e^{i\left(k_x x + k_y y\right)} dk_x\, dk_y. \tag{2.37}$$

Analogously, for the field in an arbitrary z-plane, the two-dimensional Fourier transform of the field $\mathbf{E}(x, y, z)$ yields:

$$\mathbf{E}\left(x, y, z\right) = \int\limits_{-\infty}^{+\infty} \int\limits_{-\infty}^{+\infty} \tilde{\mathbf{E}}\left(k_x, k_y; z\right) e^{i\left(k_x x + k_y y\right)} dk_x\, dk_y. \tag{2.38}$$

If we assume a homogeneous, isotropic, and lossless medium in which the field is propagating, $\mathbf{E}(x, y, z)$ has to satisfy the Helmholtz equation:

$$\left(\nabla^2 + k^2\right) \mathbf{E}(x, y, z) = 0. \tag{2.39}$$

Inserting Eq. 2.38 into Eq. 2.39 will yield the following solution for each of the plane wave components:

$$\tilde{\mathbf{E}}\left(k_x, k_y; z\right) = \tilde{\mathbf{E}}\left(k_x, k_y; 0\right) e^{ik_z z}, \tag{2.40}$$

while defining

$$k_z = \sqrt{k^2 - k_x^2 - k_y^2}, \quad \text{with} \quad k = n\frac{\omega}{c}. \tag{2.41}$$

From Eq. 2.40, we can see that when we move away from the $z = 0$ plane, each Fourier component acquires a phase factor $e^{ik_z z}$. For a lossless medium, k_z can either be real or imaginary (with a positive imaginary part such that the solution is finite for $z \rightarrow \infty$). In this case, for a certain k_x-k_y pair, there are two scenarios:

$$
\begin{aligned}
\text{Plane waves} &\rightarrow k_x^2 + k_y^2 \leq k^2, \\
\text{Evanescent waves} &\rightarrow k_x^2 + k_y^2 > k^2.
\end{aligned}
\tag{2.42}
$$

With these conditions, we can, in fact, see that the angular spectrum is a superposition of the plane and evanescent waves. If we plug the solution of the wave equation given by Eq. 2.40 into Eq. 2.38, we will finally get the following expression for the field in an arbitrary z-plane in terms of its angular spectrum representation:

$$\mathbf{E}\left(x, y, z\right) = \int\limits_{-\infty}^{+\infty} \int\limits_{-\infty}^{+\infty} \tilde{\mathbf{E}}\left(k_x, k_y; 0\right) e^{i\left(k_x x + k_y y + k_z z\right)} dk_x \, dk_y. \tag{2.43}$$

Knowing the coefficients $\tilde{\mathbf{E}}\left(k_x, k_y; 0\right)$, we can then calculate the scattered power for a given k_x-k_y pair as

$$P\left(k_x, k_y; 0\right) = \frac{n}{2Z_0} \left|\tilde{\mathbf{E}}\left(k_x, k_y; 0\right)\right|^2 \cos\theta, \tag{2.44}$$

where $Z_0 = \sqrt{\mu_0/\varepsilon_0}$ is the impedance of vacuum, n is the refractive index of the medium in which the field propagates, and the scattering angle is an angle between $\mathbf{k}$ and z-axis with $\cos\theta = \Re\{k_z/k\}$. Summation over all $\mathbf{k}$ gives the total power contained in a certain wave field.

2.1.4 Electromagnetic duality and helicity operator

Since the design of the anti-reflective (AR) nanostructures discussed throughout this thesis is in the light of their ability to preserve helicity, some introductory definitions are needed. We start with the helicity operator Λ, which is defined as the projection of the angular momentum operator $\mathbf{J}$ onto the direction of the linear momentum operator $\mathbf{P}$, and for monochromatic but spatially dependent fields, it is the curl operator divided by the wave number:

$$\Lambda = \frac{\mathbf{J} \cdot \mathbf{P}}{|\mathbf{P}|} \equiv \frac{\nabla \times}{k}. \tag{2.45}$$

Electromagnetic duality is a continuous transformation rotating electric and magnetic fields onto each other [54, 55]:

$$
\begin{aligned}
\tilde{\mathbf{E}}_\theta(\mathbf{r}, \omega) &= \tilde{\mathbf{E}}(\mathbf{r}, \omega) \cos\theta + Z\tilde{\mathbf{H}}(\mathbf{r}, \omega) \sin\theta, \\
Z\tilde{\mathbf{H}}_\theta(\mathbf{r}, \omega) &= Z\tilde{\mathbf{H}}(\mathbf{r}, \omega) \cos\theta - \tilde{\mathbf{E}}(\mathbf{r}, \omega) \sin\theta,
\end{aligned}
\tag{2.46}
$$

where θ is an arbitrary real angle and Z is the impedance of a medium. If $Z = Z_0$ (in vacuum), Maxwell's equations are symmetric under the above transformation. This means that if the electromagnetic field $(\tilde{\mathbf{E}}(\mathbf{r}, \omega), \tilde{\mathbf{H}}(\mathbf{r}, \omega))$ is a solution to Maxwell's equations, the transformed field $(\tilde{\mathbf{E}}_\theta(\mathbf{r}, \omega), \tilde{\mathbf{H}}_\theta(\mathbf{r}, \omega))$ is also a solution. However, in presence of

matter the symmetry of Maxwell's equations is broken [55]. In general, the system is dual symmetric if and only if its electric and magnetic responses to impinging radiation are equivalent (Sec. 6.11 in [51]).
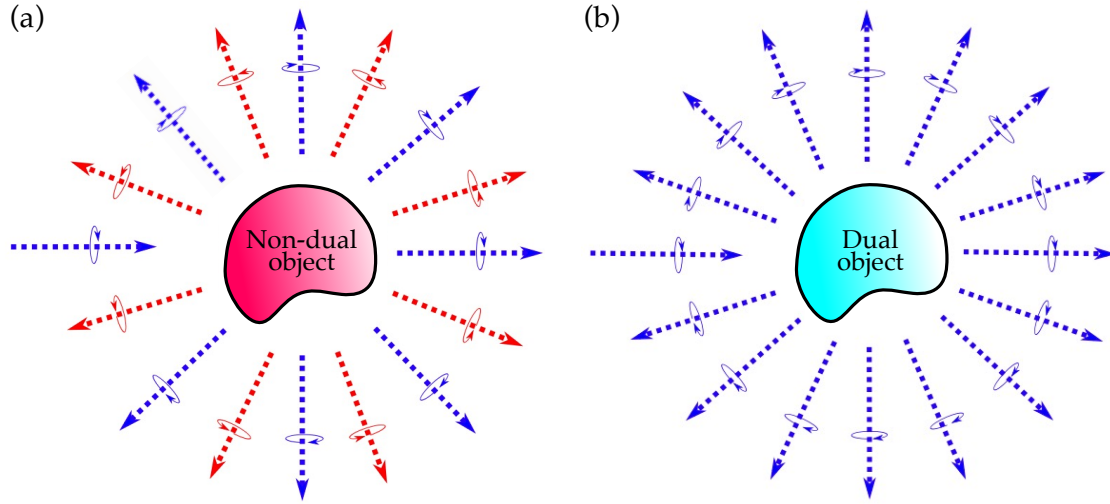
FIGURE 2.2: Illustration of light-matter interaction in the case of a non-dual (left) and dual symmetric (right) object. An incoming field with a well-defined helicity (for example, plane wave with a certain polarization handedness (blue)) is impinging on these two objects. (a) For a non-dual symmetric object, the scattered field contains components of opposite helicity (red), and the helicity of the scattered field is not well defined. In this case, helicity is not preserved. (b) The helicity of the scattered field is well defined and is equal to the helicity of the incoming field. The helicity of the scattered field is preserved. Adapted from [54].

Helicity is a generator of duality transformations: Helicity and duality are related like angular momentum and rotations or linear momentum and translations. Light-matter interaction for both dual and non-dual symmetric objects is schematically shown in Fig. 2.2. When the condition of equivalence of electric and magnetic responses is not satisfied, the system is non-dual symmetric, and the interaction with incoming field leads to components of changed helicity. For dual symmetric systems, helicity is preserved upon interaction with the incident radiation with defined helicity, and such interaction does not couple the left- and right-handed components of the electromagnetic field given as

$$\tilde{\mathbf{G}}_{\pm}(\mathbf{r}, \omega) = \frac{1}{\sqrt{2}} \left(\tilde{\mathbf{E}}(\mathbf{r}, \omega) \pm iZ\tilde{\mathbf{H}}(\mathbf{r}, \omega) \right). \tag{2.47}$$

The above equation defines Riemann-Silberstein vectors [56, 57] which are the eigenstates of the helicity operator with eigenvalues ± 1. A general $\tilde{\mathbf{G}}_{+}(\tilde{\mathbf{G}}_{-})$ field can always be decomposed into a linear combination of left(right)-handed polarized plane waves, which will be exploited in chapter 3.

2.1.5 Helicity and discrete rotational symmetry

We will now consider the light-matter interaction for systems with discrete rotational symmetries $R_z(2\pi/n)$ for $n = 1, 2, 3 \ldots$ when the normally incident plane wave has well defined helicity (polarization handedness) and is propagating along the positive $\hat{\mathbf{z}}$ direction (Fig. 2.3). We are interested in forward (along $\hat{\mathbf{z}}$) and backward (along $-\hat{\mathbf{z}}$) scattering, and what happens with helicity of the scattered field upon such interaction.
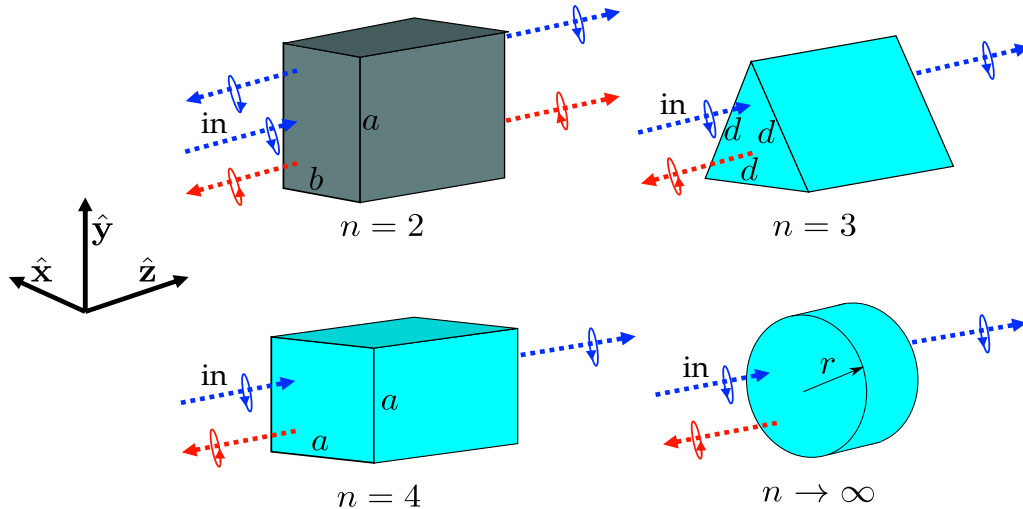
FIGURE 2.3: Illustration of forward and backward scattering by structures with different rotational symmetries $R_z(2\pi/n)$: Gray rectangular prism ($n = 2$), cyan equilateral triangular prism ($n = 3$), cyan square prism ($n = 4$) and cyan cylinder ($n \to \infty$). Blue arrows represent the plane waves of positive helicity +1 (left-handed polarization), and red arrows represent the plane waves of negative helicity -1 (right-handed polarization). The incoming plane wave marked as "in" has positive helicity. Adapted from [54].

It was shown in [54, 58], that when interaction depicted in Fig. 2.3 occurs, there is no preserved helicity component in the backward scattering direction for a system whose discrete rotational symmetry $R_z(2\pi/n)$ has $n \geq 3$. For such a system, the backward scattering can contain only the components with changed (flipped) helicity, and forward scattering can only contain the components of preserved helicity. This breaks down for systems with $n < 3$, and there are components with both helicities in backward and forward scattering directions. If the systems with $n \geq 3$ are also dual symmetric, the red arrows in Fig. 2.3 will disappear since the electromagnetic duality symmetry ensures helicity preservation for all scattering directions. This additional ingredient will lead to zero backscattering by dual symmetric systems with $n \geq 3$.

In this thesis, we will mostly consider the systems composed of natural materials with $\varepsilon_r \neq \mu_r = 1$, for which the scenario depicted in Fig. 2.3 will occur, and helicity will be preserved only along the symmetry axis. Although for such systems, it will not be possible to eradicate the backscattering, we will need to find a way to reduce the portion of the backscattered light with the flipped helicity (red arrows in Fig. 2.3) to design an effective AR coating for the solar cell applications. In this case, to relax the duality symmetry condition, we will need to design the system such that its electric and magnetic responses are equal under the prescribed illumination. The recipe to achieve the equality of these responses will be given in chapter 3, where we will analyze the AR properties of the dielectric nanostructures from the helicity preservation point of view.

2.2 Basic solar cell concepts

This section covers the aspects related to solar cell properties. It starts with a description of the working principle of a typical solar cell. Next, the particular features of a HJT silicon solar cell are introduced. Additionally, key solar cell characteristics, efficiency limits, and light management in solar cells are discussed.

2.2.1 Working principle of a solar cell

(a) (b)
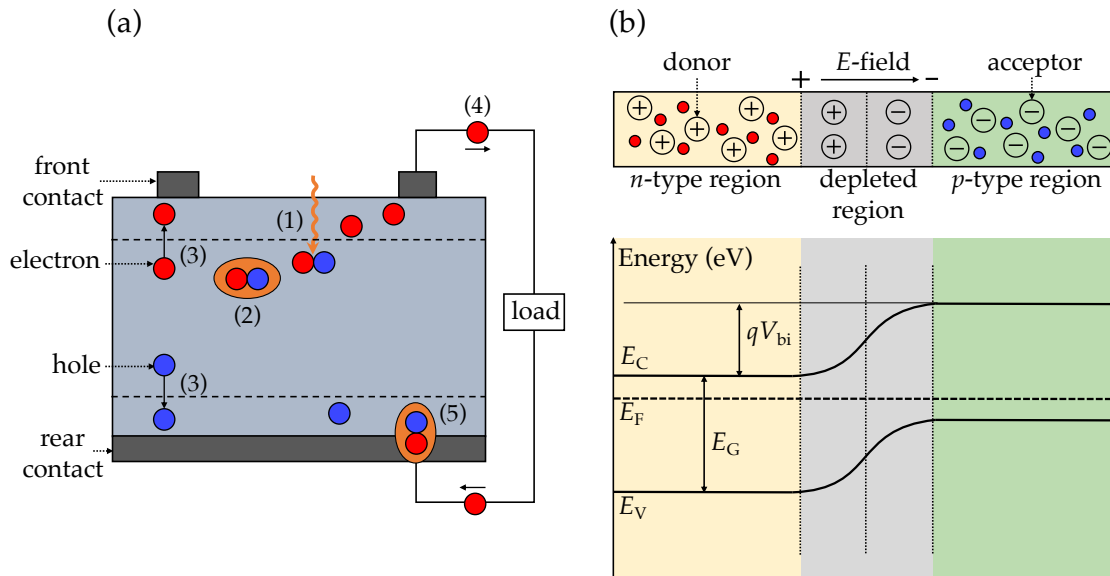
FIGURE 2.4: (a) Demonstration of the working principle of a typical solar cell: (1) generation of an electron-hole pair, (2) partial recombination of electrons and holes, (3) separation of generated charge carriers, (4) electrons feeding into external circuit, (5) electrons recombining with holes after passing through circuit. (b) Schematic of a *p-n* junction and its energy band diagram in equilibrium. E_C and E_V correspond to conduction and valence bands, E_F corresponds to Fermi level, $E_G = E_C - E_V$ is the band gap, and qV_{bi} is a potential barrier with q denoting the elementary charge and V_{bi} denoting the built-in potential.

The working principle of a solar cell is based on the photovoltaic effect – the generation of a potential difference at the junction of two materials (semiconductors) when exposed to light [59]. It is closely related to the photoelectric effect, where an excited charged carrier is emitted instead of staying within the material. Figure 2.4(a) demonstrates the processes happening in a typical solar cell under illumination:

(1) The photon is absorbed by a semiconductor absorber material, and the electron-hole pair is generated (the energy of a photon is converted to chemical energy). In this process, when a photon with energy larger than the band gap reaches the absorber of a solar cell, an electron is excited from the valence band to the conduction band of a semiconductor material, leaving the positively charged void (hole) behind. In this thesis, we deal with silicon-based solar cells. Silicon is an indirect semiconductor, meaning that the lowest point of its conduction band corresponding to the lowest-energy state in momentum space (*k*-space) and the highest point of its valence band corresponding to the highest-energy state in *k*-space are misaligned. For such a semiconductor, exciting an electron from the valence to the conduction band requires an additional momentum transfer from the vibrations of a crystal lattice, i.e., it happens with the energy exchange involving a phonon, quanta of a lattice vibration. Silicon has, therefore, a lower absorption coefficient compared to a direct band gap semiconductor, which puts constraints on the design of silicon solar cells, making light management for such cells particularly important.

(2) In general, the electron-hole pair will recombine, and the electron will return to its initial energy state. The recombination can be either radiative (energy released as a photon) or non-radiative (energy transferred to another electron/hole or released as a phonon). In crystalline silicon, the radiative recombination is inefficient due to

silicon's indirect band gap, and the dominating recombination mechanism is non-radiative Auger recombination [59]. Auger recombination is indirect and involves three particles, with energy and momentum transferred to an additional electron or hole. Additionally, recombination can occur through the lattice defects or impurities in the material (Schockley-Read Hall recombination). It is a two-step process that is facilitated by the trap states in the band gap. Moreover, electrons and holes can recombine at the surface of the material. The unsatisfied dangling bonds on the surface of silicon lead to the creation of the surface trap states within the band gap. The surface recombination rate is proportional to the surface trap density, which can be reduced by the deposition of a thin passivation layer on the front and rear surface of the silicon wafer.

(3) The generated charge carriers are then separated with semi-permeable membranes on both sides of the absorber. In the presence of such membranes, the electrons can flow only through one membrane and the holes through another one. Typically, these membranes are formed by introducing a *p-n* junction, and the charge carriers should reach them in a time shorter than their lifetime [59, 60]. Figure 2.4(b) schematically shows a *p-n* homojunction and its energy band diagram in equilibrium. To form such a junction, *n*-type and *p*-type semiconductors are brought together. To get an *n*-type semiconductor whose majority carriers are electrons, one has to dope an intrinsic semiconductor with electron donor atoms. To get a *p*-type semiconductor whose majority carriers are holes, one has to dope intrinsic semiconductor with electron acceptor atoms. In the case of crystalline silicon, an electron donor dopant is typically phosphorus (P), and an electron acceptor dopant is boron (B) or gallium (Ga). The *n*-type and *p*-type regions are formed by introducing donor and acceptor dopants into the same intrinsic semiconductor for homojunction. Due to a large difference in electron concentration in the doped regions, the electrons diffuse from *n*-type to *p*-type region across the junction. Similarly, the holes diffuse from *p*-type to *n*-type region. The diffusion of mobile carriers across the junction leaves the region close to the junction depleted of those carriers, and what is left in this region is fixed positively and negatively charged donor and acceptor ions, respectively. The width of the depleted region depends on the concentration of electron donor and acceptor atoms (N_D and N_A) in the *n*-type and *p*-type regions. The space charge around the junction leads to the formation of an electric field in the depleted region. This electric field opposes the movement of diffusing charge carriers (causes drift of the carriers). From the band diagram in Fig. 2.4(b), one can see that in equilibrium, the Fermi energy E_F is constant across the junction. The conduction band E_C and the valence band E_V bend in the depleted region due to an electric field present there. Since there is an electric field in this region, it means there is a built-in electrostatic potential difference V_{bi} across the depleted region. Suppose the *p-n* junction is illuminated and additional charge carriers are generated. In that case, the concentration of minority carriers in *n*-type and *p*-type regions (holes for *n*-type and electrons for *p*-type) increases significantly with increasing illumination intensity. These minority carriers flow across the depleted region, becoming majority carriers: Holes from *n*-type to *p*-type region, and electrons from *p*-type to *n*-type region. An illuminated *p-n* junction is not under equilibrium anymore, and the concentrations of the charge carriers are described by the quasi-Fermi energy for electrons and holes, respectively. The flow of the carries mentioned above is proportional to the gradients of these quasi-Fermi levels.

(4) The charge carriers can then be extracted at the metallic contacts, and if those are connected (cell is short-circuited), the generated carriers will flow through the
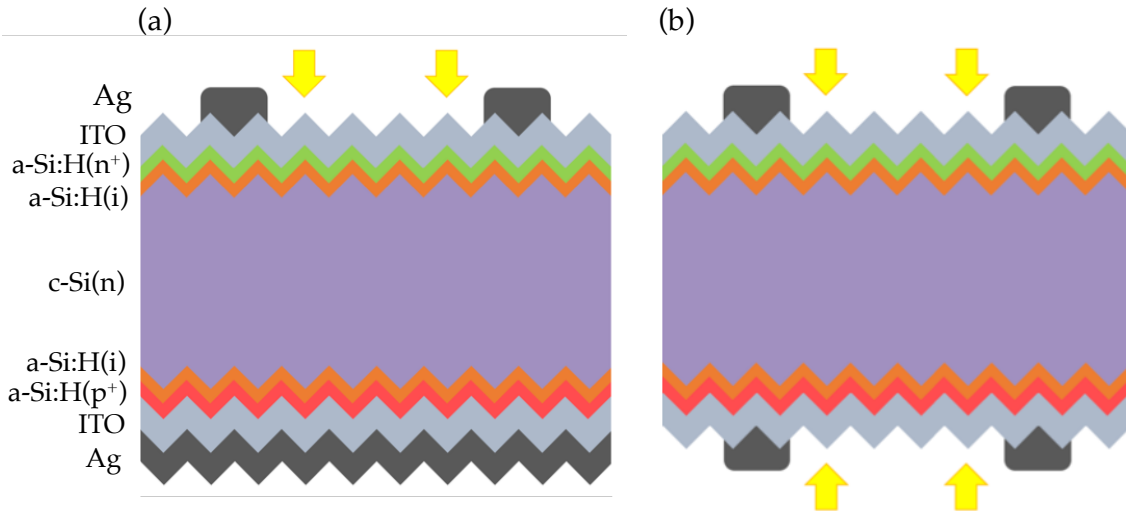
FIGURE 2.5: Schematic image of HJT silicon-based solar cell with rear emitter in both (a) mono- and (b) bifacial configurations. In both cases, the *n*-type crystalline silicon wafer is passivated on both sides with a thin layer of intrinsic hydrogenated amorphous silicon (a-Si:H(*i*)). A heavily *n*-doped layer of hydrogenated amorphous silicon (a-Si:H(n^+)) and a heavily *p*-doped layer of hydrogenated amorphous silicon (a-Si:H(p^+)) are deposited on top of the a-Si:H(*i*) layers on the front and rear side of the devices, respectively. Next, a transparent conducting oxide (TCO) is deposited on both sides – indium tin oxide (ITO). Lastly, the silver contacts are deposited on both sides of the cells. The monofacial HJT cell (a) has full metallization on the rear side, while the bifacial HJT cell (b) has a similar contacting on its rear side as on its front.

external circuit. In this way, the chemical energy is converted to electric energy.

(5) After the electrons pass through the external load, they will complete the circuit and recombine with holes at an interface between the metal contact and cell absorber.

2.2.2 Heterojunction silicon solar cell

In this thesis, the heterojunction technology (HJT) silicon-based solar cell is investigated. The advantages of this technology include excellent wafer passivation by thin amorphous silicon films, low-temperature processing (<200°C) that allows using thinner silicon wafers without causing less substrate warping and the small number of fabrication steps [61].

Figure 2.5 schematically shows such a cell in both mono- and bifacial configurations. A heterojunction is used in this type of device instead of the homojunction discussed in the previous section. In this case, the junction is formed by a *p*-type semiconductor material brought together with an *n*-type semiconductor made from another material. For HJT solar cells, these materials are monocrystalline silicon (band gap 1.12 eV) and hydrogenated amorphous silicon (band gap around 1.7 eV). The absorber is usually a Czochralski monocrystalline silicon wafer, either *n*- or *p*-doped [61, 62]. In this thesis, the silicon wafer of a considered solar cell design is *n*-type since it has a few advantages compared to its *p*-type counterpart. First, for the same impurity concentration, the lifetime of minority carriers in the bulk of *n*-type wafers is generally higher than of *p*-type wafers [63]. Additionally, the passivation of *p*-type wafers is usually more difficult to achieve [64]. Usually, monocrystalline Si(100) substrates are used, for which Si(111) faceted pyramids are formed during the wet chemical etching process [19]. The thickness

of the c-Si wafer tends to be reduced over the years, and, as of 2020, the standard thickness of the wafer of the industry-type silicon-based solar cell is around 160 μm [22].

The silicon wafer is then passivated on both sides with intrinsic hydrogenated amorphous silicon (a-Si:H(*i*)). This way, the crystalline silicon dangling bonds are hydrogenated, and the surface defect density is reduced. Excellent passivation by a-Si:H(*i*) allows for high open-circuit voltages of HJT solar cells, reaching above 740 mV. Next, the thin layers of heavily doped amorphous silicon are introduced on top of the passivating a-Si:H(*i*) films. In this thesis, we consider a rear emitter HJT solar cell, for which the heavily *p*-doped amorphous silicon (a-Si:H(p^+)) film is deposited on the rear side of the device (emitter), while a heavily *n*-doped amorphous silicon (a-Si:H(n^+)) film is deposited on the front side. These amorphous silicon thin films are deposited using plasma-enhanced chemical vapor deposition (PECVD). The thickness of the front a-Si:H(*i*,n^+) layer combination and the rear a-Si:H(*i*,p^+) combination can be well controlled in the deposition process and is smaller than 15 nm for either side of the cell. The holes then drift to the a-Si:H(p^+) layer crossing the p^+-*n* heterojunction, and electrons drift to the a-Si:H(n^+) layer crossing the n^+-*n* heterojunction.

The carrier collection in HJT solar cells occurs via a transparent conducting oxide (TCO), typically indium tin oxide (ITO). ITO films are deposited on either side of the solar cell. A the same time, on the front, this layer also serves as an antireflective coating. It has a typical thickness of around 80 nm, corresponding to minimal reflectance at a wavelength of $\lambda = 600$ nm [62]. It should be noted that for the rear emitter cell configuration, which is considered here, the trade-off between optical and electrical bulk properties of the front ITO layer is less pronounced than for front emitter cell configuration, and, consequently, the requirements for the front ITO film are more relaxed: When n^+-*n* heterojunction is on the front, the power losses associated with carrier collection can be reduced since the lateral conductivity of the absorber is utilized opening up an additional transport path [65]. For the rear ITO film, to ensure optimal optical performance (which is relevant for the bifacial configuration), it would be feasible to deposit ITO film of the thickness around 200 nm. However, a typical rear ITO film is comparable/thinner than the front ITO film since it limits the production costs. ITO films are usually deposited using physical vapor deposition (PVD). Typical carrier mobilities in sputtered ITO are usually between 20 and 40 cm^2/V·s, while the free-carrier density is tuned between 10^{19}–10^{21} cm^{-3} yielding low sheet resistances (3–100 Ω/sq) [61].

Lastly, metallic contacts are deposited on the front and rear sides of a HJT solar cell. Screen-printing is the most common method of metallization in crystalline silicon PV, and the typical conductor lines are 35–40 μm wide. As mentioned before, the processing temperatures of HJT cells have an upper bound of 200°C, and for this type of solar cell, the low-temperature silver paste is used. Since for a HJT solar cell, both mono- and bifacial configurations are possible, contacting on the rear side of the device is either the same as on the front (screen-printed metallic grid) or a conformal silver layer.

2.2.3 Solar cell parameters

The key parameters used to characterize a solar cell's performance are short-circuit current density J_{SC}, open-circuit voltage V_{OC}, maximal power P_{max}, and the fill factor *FF*. The power conversion efficiency (PCE) η can be determined from these parameters, which can be obtained from the illuminated current-voltage (*I-V*) characteristic of the solar cell.

The *I-V* characteristic of a solar cell behaving like an ideal diode is given as [59]

$$I(V) = I_{\text{rec}}(V) - I_{\text{gen}}(V) - I_{\text{ph}} = I_0 \left[\exp\left(\frac{qV}{k_{\text{B}}T} \right) - 1 \right] - I_{\text{ph}}, \qquad (2.48)$$

where $I_{\text{rec}}(V)$ is the recombination current, $I_{\text{gen}}(V)$ is the thermal-generation current, $I_{\text{ph}}(V)$ is the photogenerated current, I_0 is the dark saturation current (reverse-blocking current), q is the elementary charge, k_{B} is Boltzmann's constant, and T is the temperature. This behaviour can be described by an equivalent circuit, where the diode is formed by a *p-n* junction.

In reality, the performance of the solar cell is influenced by the series resistance R_{s} and the shunt resistance R_{sh}, which can have a negative impact on the fill factor. When these resistances are taken into account, the *I-V* characteristic is described by the following equation:

$$I(V) = I_0 \left[\exp\left(\frac{q(V - IR_{\text{s}})}{k_{\text{B}}T} \right) - 1 \right] + \frac{V - IR_{\text{s}}}{R_{\text{sh}}} - I_{\text{ph}}, \tag{2.49}$$

As can be seen from Eqs. 2.48 and 2.49, to have the minimal impact on the solar cell performance, the series resistance should be as small as possible, and the shunt resistance should be as large as possible.

(a) (b)
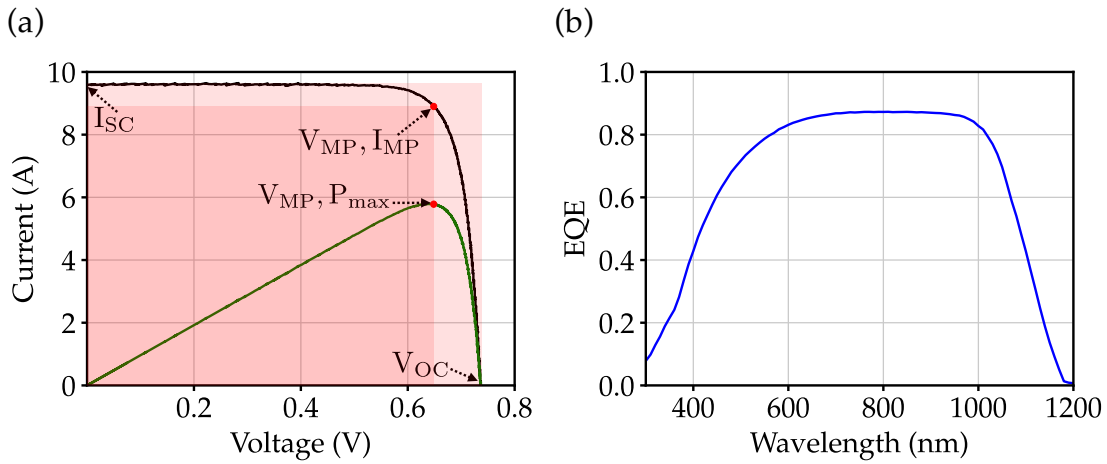
FIGURE 2.6: (a) The current-voltage characteristic (black) and power (green) of a typical HJT solar cell. For this particular cell, the short-circuit current I_{sc} and the open-circuit voltage V_{OC} were determined to be 9.6 A and 0.736 V, respectively. Maximal power P_{max} which is a product of the current at maximum power point I_{MP} and the voltage at maximum power point V_{MP}, was around 5.8 W. The fill factor is represented by the red-tinted area and was found to be around 82.1 %. This cell had a power conversion efficiency of around 23.8 %. (b) The external quantum efficiency of the same solar cell. Data were provided courtesy of Meyer Burger Research AG in Hauterive, Switzerland.

The current-voltage characteristic of a HJT solar cell, from which one can extract the main solar cell parameters, is shown in Fig. 2.6(a). The short-circuit current I_{SC} is the current flowing through the external circuit when the electrodes of a solar cell are short-circuited and $V = 0$. To remove the dependence of I_{SC} on the area of the device, one can use the short-circuit current density J_{SC}. The open-circuit voltage V_{OC} is the voltage at which the current I flowing through the external circuit is zero. It corresponds to a forward bias voltage at which the dark saturation current compensates for the photogenerated current. The power P_{max} defines the maximum power point (MPP) on the solar cell's $I - V$ characteristic, and it is given by the product of the current I_{MP} and voltage V_{OC} at this point. The fill factor is defined as the ratio between the maximal power and the product of V_{OC} and I_{SC}:

$$FF = \frac{P_{\text{max}}}{V_{\text{OC}} \cdot I_{\text{SC}}} = \frac{V_{\text{MP}} \cdot I_{\text{MP}}}{V_{\text{OC}} \cdot I_{\text{SC}}}. \tag{2.50}$$

Graphically, the *FF* can be represented as the surface ratio of two rectangles (darker red-tinted area divided by lighter red-tinted area in Fig. 2.6). Finally, the PCE of the solar cell can be calculated as the ratio between the maximal power generated by the cell and the incident power as

$$\eta = \frac{P_{\text{max}}}{P_{\text{in}}} = \frac{V_{\text{OC}} \cdot I_{\text{SC}} \cdot FF}{P_{\text{in}}}. \tag{2.51}$$

The other frequently used characteristic of a solar cell is the external quantum efficiency (EQE). This wavelength-dependent quantity corresponds to the fraction of photons incident on the solar cell and generating electron-hole pairs in the solar cell absorber, which contribute to the short-circuit current. One can obtain the EQE by illuminating a solar cell with monochromatic light of the wavelength λ and measuring the generated photocurrent. The EQE is given by the following equation:

$$\text{EQE}(\lambda) = \frac{J_{\text{ph}}(\lambda)}{q \cdot \phi(\lambda)}, \tag{2.52}$$

where $J_{\text{ph}}(\lambda)$ is the generated photocurrent density, q is the elementary charge, and $\phi(\lambda)$ is the photon flux incident on the solar cell. The EQE of a typical HJT solar cell is shown in Fig. 2.6(b). From such a characteristic, one can then calculate the short-circuit current density J_{SC} as

$$J_{\text{SC}} = q \int_{\lambda_1}^{\lambda_2} \phi(\lambda) \text{EQE}(\lambda) \, d\lambda. \tag{2.53}$$

For a c-Si-based cell such as a HJT solar cell, the relevant wavelength range is from 300 nm to 1200 nm.

A parameter related to EQE is the internal quantum efficiency IQE, which corresponds to the fraction of photons absorbed in the absorber layer of the solar cell and generating the charge carriers, which subsequently contribute to the short-circuit current. It is given by the following equation:

$$\text{IQE}(\lambda) = \frac{\text{EQE}(\lambda)}{1 - R(\lambda)}, \tag{2.54}$$

where R is reflectance.

2.2.4 Solar irradiance and efficiency limits

Since only photons with suitable energy can be absorbed and generate the electron-hole pairs in a particular semiconductor, it is important to know the spectral distribution of the solar radiation. The solar radiation spectrum can be described either by the spectral irradiance $SI(\lambda)$ or the spectral photon flux $\phi(\lambda)$, which are linked by the following equation [59]:

$$SI(\lambda) = \phi(\lambda) \frac{hc}{\lambda}, \tag{2.55}$$

where hc/λ is the photon energy.

Figure 2.7 shows the spectral irradiance outside the atmosphere of earth (AM0) and global spectral irradiance (AM1.5G) that is attenuated by the atmosphere. This attenuation is caused by the scattering and absorption by dust particles, air molecules, etc. The key parameter that defines solar irradiance under clear sky conditions is the distance that the sunlight travels through the atmosphere. It is the shortest when the sun is directly overhead (at the zenith). Optical air mass (AM) is the ratio of an actual path length of the sunlight to the shortest distance and is defined as $1/\cos(\theta)$, where θ is the zenith angle (angle between sun position and the zenith). The standard spectrum at the surface

of the Earth AM1.5G corresponds to $\theta = 48.2°$. For this spectrum shown in Fig. 2.7, the integrated irradiance yields 997.5 W/m^2 [66]. The standard test conditions (STC), which allow comparing various solar cells and solar modules, are characterized by the AM1.5G spectrum and a cell temperature of 25°C. However, it should be noted that per international standard [67], the values for the spectral irradiance from [66] have to be multiplied by a normalization factor such that the integrated irradiance of 1 kW/m^2 corresponding to the STC could be achieved. The actual solar irradiance, which is incident on a particular location on Earth, depends on the local conditions such as cloud coverage. In this thesis, the performance of the solar modules under realistic irradiation conditions will be discussed in chapter 4.
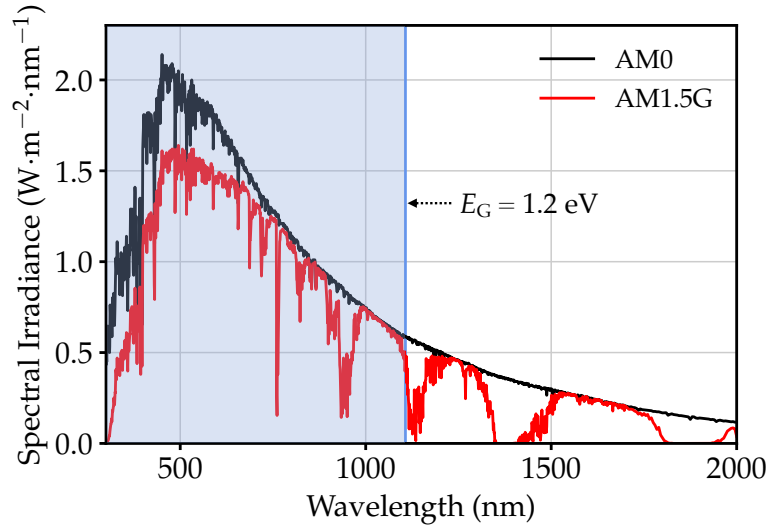
FIGURE 2.7: Spectral irradiance as a function of the wavelength. The spectrum outside the atmosphere (AM0) and global standard spectrum (AM1.5G) are shown. The blue-tinted area highlights the fraction of the spectrum relevant for single junction silicon-based solar cells. The right edge of this area corresponds to the band gap energy of silicon. The data for both spectra is taken from [66].

The critical question is, which portion of the spectral irradiance can be utilized by a PV device, particularly by a single junction silicon-based solar cell. The blue-tinted area in Fig. 2.7 indicates the part of the spectrum relevant for silicon-based cells. Here, the long wavelength edge of this region corresponds to the band gap energy of crystalline silicon $E_G = 1.12$ eV (wavelength around 1107 nm). However, since silicon is an indirect band gap semiconductor material, the cut off is not sharp, and light beyond this limit can still be absorbed by the silicon wafer. The most general efficiency limit for a solar cell is the thermodynamic efficiency limit, and it can be calculated as the efficiency of an ideal engine (Carnot engine). It is given by the following equation:

$$\eta_{\text{Carnot}} = 1 - \frac{T_c}{T_s}, \tag{2.56}$$

where T_c and T_s are the temperatures of the solar cell and the sun, respectively. With $T_c = 300$ K and $T_s = 6000$ K, the thermodynamic efficiency limit is about 95 %.

The more realistic efficiency limit for a single junction solar cell was introduced by W. B. Shockley and H. J. Queisser in 1961 who used a detailed balance approach to derive it [16]. In their calculations, they assumed that all the photons above the band gap are absorbed and that carrier mobility is infinite, allowing for the collection of the carriers

irrespective of where they are generated. Starting with a general definition of efficiency as the ratio between the power delivered to a load to the power incident on the solar cell, they arrived at the following expression [16]:

$$\eta_{SQ} = t_s \cdot u(x_g) \cdot v(f, x_c, x_g) \cdot m(v\, x_g / x_c),$$
(2.57)

where t_s is the probability that incident photons will produce an electron-hole pair, $u(x_g)$ is the ultimate efficiency limit, $v(f, x_c, x_g)$ is the band gap utilization efficiency, and $m(v\, x_g / x_c)$ is the impedance matching factor linked to the fill factor of the solar cell. Apart from the probability factor t_s, the efficiency introduced in the above equation is a function of the following variables: (1) two ratios involving band gap energy and temperatures of the sun and a solar cell $x_g = E_G / k_B T_s$ and $x_c = T_c / T_s$, (2) factor f which combines the parameters involving radiative recombination out of the solar cell and geometrical factor taking into account the limited angle from which the solar irradiation impinges on the object. For a silicon-based solar cell, the detailed balance limit yields maximum efficiency of around 32 %. However, this estimate for silicon-based cells is optimistic since only the radiative recombination is taken into account. A study conducted by A. Richter *et al.* in 2013 for a silicon-based solar cell arrived at the efficiency limit of 29.43 % [17].

2.2.5 Light management and optical losses

Now we consider the common light management strategies applied in solar cell design, which allow to enhance absorptance in the absorber layer of the device and negate the optical losses. In general, to maximize the absorptance, on the one hand, one has to suppress reflection, thus improving light in-coupling in the device, and, on the other hand, one has to introduce an efficient light trapping (LT) scheme to prevent the photons from leaving the solar cell without generating an electron-hole pair. The loss mechanisms also include parasitic absorption in the layers other than the cell absorber and shading losses from the contacting grid on top (and bottom in bifacial solar cell configuration) of a solar cell. The latter is neglected in this thesis.

First, we cover the typical approaches used to reduce reflection losses. In general, light impinging on an interface between two media with different refractive indices will be partly transmitted and partly reflected. As can be seen from the Fresnel equations (Eq. 2.29), the more significant the refractive index mismatch, the stronger the reflection at the interface. Given the high refractive index of c-Si, the reflection losses at the air/c-Si interface will be between 30 % and 40 % in the wavelength region corresponding to peak spectral irradiance. One way to reduce this loss is to apply an anti-reflective coating (ARC). It can be derived from the Fresnel equations, that at a certain wavelength λ_0, the refractive index of the ARC shall satisfy the following equation [53]:

$$n_{ARC} = \sqrt{n_1 n_2},$$
(2.58)

where n_1 and n_2 are the indices of the media between which the ARC is inserted (e.g., air and c-Si). Typically, the thickness of this film is chosen such that destructive interference will occur between the two waves reflected from the front and back interface of the ARC. This leads to the following condition for the ARC thickness:

$$t_{ARC} = \frac{\lambda_0}{4 n_{ARC}}.$$
(2.59)

Adding more ARCs can reduce reflection even further, allowing for smoother index change as the light is traversing the stratified medium [68–71]. However, this index grading technique can complicate cell processing and introduce additional parasitic

absorption losses.

Another approach to reflection suppression employs textured interfaces. As was already briefly discussed in Sec. 2.2.2, for silicon-based cells, including HJT devices, such textures comprise pyramidal structures with bases between 3 μm to 5 μm, which emerge upon chemical etching. Since the dimensions of the pyramids are larger than the relevant wavelengths, these structures are typically treated in the geometrical limit. Such textures help to enhance the coupling of light into silicon wafers due to increased chances of reflected light bouncing back onto the surface. It is quite common to combine both the surface texture and ARC, as it is done for the HJT solar cells where in addition to texture, the conducting ITO layer also serves as an ARC.

Once the light reaches the solar cell absorber, the next step is to ensure that a sufficient LT scheme is in place such that the photons do not escape from the device without generating the charge carriers. The intensity of light traveling through an absorptive medium decreases exponentially, and it is described by the Beer-Lambert law given as

$$I(d, \lambda) = I_0 \exp(-\alpha(\lambda)d), \tag{2.60}$$

where d is the distance the light travels in the medium, I_0 is the initial intensity, and $\alpha(\lambda)$ is the absorption coefficient of the material [59]. The fraction of the incident light absorbed in the material can thus be expressed as the difference between the light intensity impinging on the absorber and the light intensity transmitted through it:

$$I_{\text{abs}}(d, \lambda) = I_0[1 - \exp(-\alpha(\lambda)d)]. \tag{2.61}$$
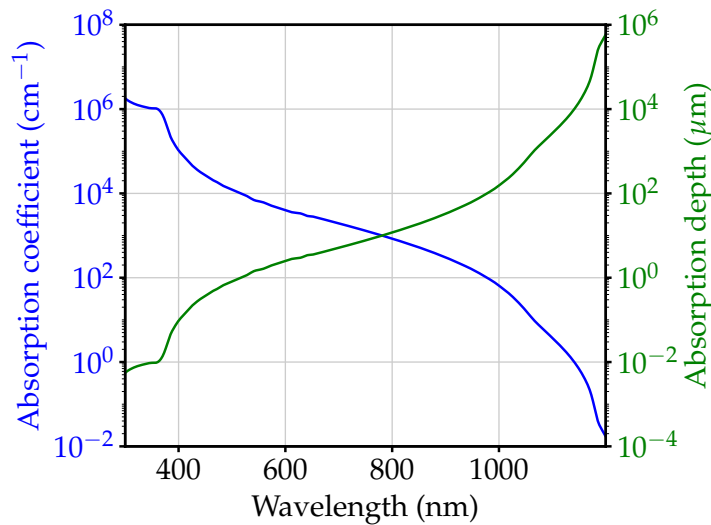
FIGURE 2.8: Absorption coefficient (α) and absorption depth (d_{a}) of crystalline silicon. d_{a} is inversely proportional to α. The values of the extinction coefficient were taken from [72].

The absorption coefficient α determines the absorbing properties of the material, and it can strongly vary in the spectral range relevant for a solar cell. It is given by the following equation:

$$\alpha(\lambda) = \frac{4\pi\kappa(\lambda)}{\lambda}, \tag{2.62}$$

where an extinction coefficient κ is the imaginary part of a complex refractive index which was defined in Eq. 2.17. The absorption depth d_{a} in the material can then be determined

as $1/\kappa$. Figure 2.8 shows these two quantities as the function of wavelength for c-Si. Since it is an indirect band gap semiconductor, it is a relatively poor absorber. As can be seen from this graph, short-wavelength photons are absorbed near the surface of silicon. In contrast, the thickness required to absorb the photons of longer wavelengths will be unfeasible for solar cell fabrication. It will negatively affect the electrical properties of the device. Hence, the optical path length within the absorber layer has to be sufficiently increased.

The common LT strategies applied in industrial-type c-Si cells include having a mirror at the device's rear side, leading to considerable enhancement of the optical path length. For HJT solar cells, a silver layer in the monofacial configuration serves this purpose. However, having a metallic layer leads to additional parasitic absorption losses. The silicon wafer texturing applied in commercial devices allows achieving efficient LT in the solar cell by changing the propagation of the light inside the absorber such that the total internal reflection can be achieved. For c-Si/air interface, the critical angle defined in Eq. 2.35 is around $16°$ [73, 74].

A very effective LT can be achieved by introducing a Lambertian scatterer that can randomize the incident light's propagation directions at the interface between the absorber and surrounding medium [75]. For instance, if a Lambertian scatterer is present on the front surface of the absorber material, the impinging light will be scattered into propagation directions with a cosine distribution. Since an absorber material is usually an optically thicker medium, it will offer a larger phase-space for light to be filled compared to an adjacent medium [73]. This way, the light will be preferably scattered into the absorber layer, leading to its high confinement in the absorber volume.

The maximal enhancement of the optical path length in a weakly absorbing medium was established by E. Yablonovitch in 1982 [76]:

$$\beta_{\mathrm{opt}} = 4n^2, \tag{2.63}$$

where n is the refractive index of the absorber. In this approach, a Lambertian front texture and a perfect mirror on the rear of the solar cell were assumed. The derivation of Eq. 2.63 was done in the geometrical optics limit and is only valid for absorber thicknesses larger than the wavelength. For c-Si, the Yablonovitch limit yields $\beta_{\mathrm{opt}} \approx 50$.

2.3 Numerical methods

2.3.1 Finite element method

Throughout this thesis, we will be dealing with structures whose dimensions are smaller than or comparable to the incident wavelength. In such a scenario, Maxwell's equations have to be solved to accurately simulate the light propagation through the considered system. For the problems encountered in this work, applicable numerical techniques include the Fourier modal method [77], the finite-difference time-domain method (FDTD) [78], the finite-difference frequency-domain (FDFD) [79], and the finite element method (FEM) [80, 81]. The majority of the results presented in this thesis were obtained by means of FEM using the commercial Maxwell solver *JCMsuite* [82].

The FEM is a numerical technique employed to obtain approximate solutions to boundary-value problems of mathematical physics, including electromagnetic problems. The basic principle of this technique is to replace a continuous domain with a finite number of subdomains in which the unknown function is represented by the local ansatz functions with unknown coefficients. This way, an original boundary-value problem with an infinite number of degrees of freedom is reduced to a problem with a finite number of degrees of freedom, with the solution of the entire system being approximated by a finite number

(a) (b)
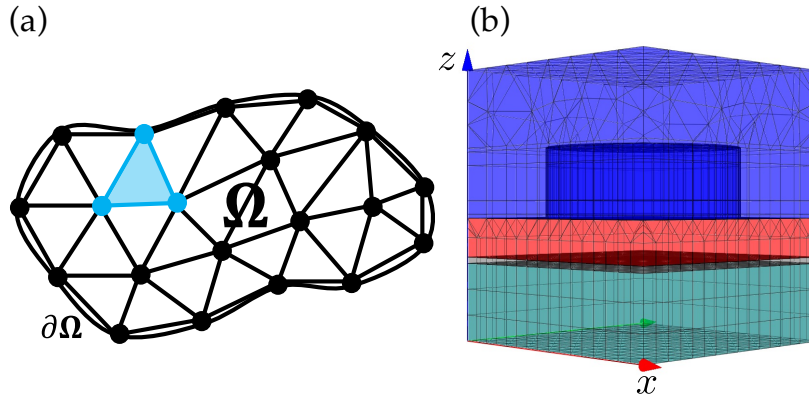
FIGURE 2.9: (a) Schematic image of a two-dimensional domain Ω with border $\partial\Omega$ discretized into small elements of triangular shape. A single element is highlighted in blue. (b) Snapshot of an exemplary discretized three-dimensional computational domain in *JCMsuite* for a nanodisk placed on top of a substrate. The boundaries on the top and bottom of the domain are transparent. The boundaries on the sides are either transparent (simulation of an isolated disk) or periodic (simulation of a square array of nanodisks).

of unknown coefficients [80]. The basic steps of the FEM comprise:

1. **Discretization of the domain.** Let us consider a domain Ω that is discretized in the first step of the FEM. It is a very important step since how Ω is discretized impacts the computational time, the memory requirements, and the accuracy of the numerical solutions. The entire domain is subdivided into a number of small patches (elements). For a two-dimensional domain, the elements are typically small triangles or rectangles. The discretization of such a domain is schematically shown in Fig. 2.9(a) with a single element highlighted in blue. In the case of a three-dimensional domain, the elements may be tetrahedra, triangular prisms, or rectangular bricks. Figure 2.9(b) shows the snapshot of a discretized three-dimensional computational domain in *JCMsuite*.

2. **Selection of the ansatz functions.** Let us stick to a two-dimensional case, for which a domain Ω is discretized into triangular elements as shown in Fig. 2.9(a) denoted as K. On each element we now define N_K vectorial ansatz functions ϕ_i with $i = 1, 2, 3, \ldots, N_K$. Here, N_K denotes the dimension of the local function space V_K, which is a part of the global function space V_h. The set of ansatz functions forms the basis of V_K. If we solve the Helmholtz wave equation for an electric field, the approximation of the solution on an element, which is a superposition of the local ansatz functions ϕ_i, is given by [82]:

$$\mathbf{E}_K = \sum_{i=1}^{N_K} a_{K,i}\phi_i, \tag{2.64}$$

where $a_{K,i}$ are the unknown coefficients. The local ansatz functions ϕ_i are usually the polynomials of a fixed order whose support is restricted to one or a few elements.

3. **Formulation of the system of equations.** To apply the FEM, one has to derive a weak formulation of Maxwell's equations. The description of such derivation can be found in [81]. The weak form of Maxwell's equations is then discretized. This way, the FEM restricts the function space V to a finite dimensional space $V_h \subset V$, with N_h being the dimension of V_h. This essentially means that the FEM does

not approximate Maxwell's equations but rather the function space in which the solution is determined. If the expansion of electric field $\mathbf{E}_h(\mathbf{r})$ of a form given by Eq. 2.64 is inserted into the discrete version of Maxwell's equations, it will result in the following linear system of equations [82]:

$$A \cdot \mathbf{a}_h = \mathbf{f}, \tag{2.65}$$

where the elements of the matrix system are given by $A_{ji} = a(\phi_i, \phi_i)$, vector $\mathbf{a}_h$ is composed by the unknown coefficients in the expansion of a form given in Eq. 2.64, and $f_j = f(\phi_j)$ depend on the imposed boundary conditions. The boundaries of the computational domain can be either periodic or transparent. In the case of periodic boundary conditions, the simulated structures are periodic in the direction perpendicular to the respective boundary. When the transparent boundary conditions are imposed, the perfectly matched layers (PMLs) are used [83]. These artificial layers attenuate the electromagnetic waves which are incident upon them and prohibit their reflection back into the interior of the computational domain. To perform optimally, the PMLs should have a sufficient thickness.

4. **Solution of the system of equations.** Solving the system of equations formulated in the previous step is the most time-consuming part of the FEM process. The size of the matrix A in Eq. 2.65 will scale with the number of the elements into which the domain Ω is subdivided. Thus, for the problems which require fine meshing of the computational domain, the FEM might become very costly. It is also important to remember that Maxwell's equations are solved in the frequency space, and the simulation for a broad spectral range involves multiple calculations. *JCMsuite* has a feature allowing to parallelize the computations, which is in handy when multiple calculations are needed. The accuracy of the solution depends on the mesh size h and the polynomial degree p of the local ansatz functions on each of the elements into which the computational domain is split. The error of the obtained solution can be estimated by the following equation [84]:

$$\text{error} \propto \left(\frac{h}{\lambda}\right)^p, \tag{2.66}$$

where λ is the local wavelength in each material in the computational domain. Hence, increasing the polynomial order p is favorable since it leads to an exponential decrease of the error. However, one has to take care when choosing the values of h and p to find a trade-off between the accuracy of the solution and the required computational resources since, in some cases (e.g., in case of a coarse mesh), further increasing p will not improve the accuracy of the solution.

5. **Post-processing of the results.** From the electric field obtained by solving Maxwell's equations, quantities such as the absorbed energy and the energy flux can be extracted, which allows calculating quantities such as the absorptance in a certain layer of the solar cell device or reflectance of the substrate coated by the nanostructure array (e.g., for a system represented by a computational domain in Fig. 2.9(b)).

2.3.2 Energy yield methodology

The energy yield simulation framework used in this work was developed by Tenure-Track-Prof. Dr. Ulrich W. Paetzold, Dr. Malte Langenhorst, and Dr. Raphael Schmager from IMT/LTI at KIT, and Dr. Jonathan Lehr from LTI. It is a comprehensive modeling framework, enabling the quick simulation of various PV architectures under realistic irradiation conditions [85]. The detailed information on the features of this modeling framework can be found in [86]. Here, only a brief overview of its respective modules is

given. The energy yield simulation framework consists of four parts:

1. The **Optics Module** calculates the wavelength- and angular-dependent absorptance of the specified solar module architecture. In this thesis, a single-junction silicon-based solar module in a mono- and bifacial configuration was investigated. The module combines the transfer matrix method (TMM) for the planar interfaces with the geometrical ray tracing for the textured interfaces. Absorptance in the optically thick layers, like the silicon absorber and the window glass and encapsulation layers, is calculated using the Beer-Lambert law (Eq. 2.60). The optics module was adjusted to integrate the angular and spectral response of the nanostructure arrays calculated by means of FEM for the solar cell-encapsulation interface for both rear and front side of the solar module. Once the response of these different kinds of interfaces is calculated, the total absorptance in each layer is calculated using the matrix formalism described in [87].

2. The **Irradiation Module** calculates the spectral and angular-resolved annual irradiance with a temporal resolution of one hour for the locations in different climate zones. The realistic direct and diffuse irradiance are derived by using a simple model to account for the cloud coverage.

3. The **Electrical Module** calculates the temperature-dependent current density-voltage characteristics while taking into account the series and shunt resistances for a given short-circuit current density of the cell. Additionally, the maximum power point is determined to calculate the output power of the solar module.

4. The **Energy Yield Core Module** calculates the annual energy yield (EY) of the solar module depending on its location, tilt angle, and the direction the module is facing. The EY is determined by combining absorptance, the spectral and angular-resolved irradiation of the solar module, and electrical properties.

2.3.3 Finite-difference time-domain method

For the calculations where larger computational domains are required (chapter 5), we will employ the finite-difference time-domain method (FDTD) since, in contrast to FEM, it allows us to obtain results at different frequencies simultaneously. The computations based on that method can also nicely be parallelized on a larger number of computers, unlike finite element-based methods that can only be distributed. These advantages make FDTD particularly appealing when considering larger computational domains. Here, we will only briefly discuss this numerical method. The detailed description can be found in [79, 88].

The FDTD method solves Maxwell's equations in time domain and originates from an algorithm proposed by Yee [89] in 1966. Maxwell's equations are solved numerically on a discrete grid in both space and time, and Yee's algorithm allows to approximate the continuous derivatives by second-order accurate, two-point centered difference forms. The electromagnetic field components are located at different spatial and temporal locations in a unit cell of the so-called Yee grid. The electric field components are spatially discretized along the edges of such a cell, while the orthogonal magnetic field components are spatially discretized at the centers of the cell faces. This way, each electric field component is surrounded by four magnetic field components and vice versa. A leapfrog updating scheme in the time domain advances the field components. The field components of $\mathbf{E}(\mathbf{r}, t)$ or $\mathbf{H}(\mathbf{r}, t)$ are calculated at times which are an odd multiple of the half time step $\Delta t/2$, while the field components of $\mathbf{H}(\mathbf{r}, t)$ or $\mathbf{E}(\mathbf{r}, t)$ are updated at times which are an even multiple of $\Delta t/2$ [88].

All the simulations using the FDTD method were performed using the free software *Meep* [90]. Through FDTD, we either determined the scattered field in the frequency

domain after performing the discrete Fourier transform of the field in the time domain, subsequently obtaining the angular spectrum, or calculated reflectance directly, dividing the backscattered field's energy flux by the incident field's energy flux.

3. Anti-Reflective Nanostructures with Periodic Arrangement

In this chapter, after a short introduction in Sec. 3.1 we will show that the AR properties of optimally designed high-index dielectric nanodisks arranged in a periodic lattice are closely related to how well the nanostructured system as a whole preserves helicity of the incoming light when the incident radiation is along the symmetry axis (Sec. 3.2). Moreover, in Sec. 3.3, we will show the experimental realization of the nanostructured HJT solar cell stack with the geometrical parameters determined in Sec. 3.2. The content of this chapter is mainly based on [P1]. The experimental work presented in this chapter was done in collaboration with the research group of Tenure-Track-Prof. Dr. Ulrich W. Paetzold from IMT/LTI at KIT, CFN at KIT, SUSS MicroOptics SA in Hauterive, Switzerland, and CSEM in Hauterive, Switzerland.

3.1 Introduction

The article of Kerker *et al.* from 1983 [91] became the inspiration for the extensive research on backscattering suppression. This work demonstrated that a sphere with equal relative electric permittivity (ε_r) and magnetic permeability (μ_r) yields zero backscattering when illuminated by a plane wave. For an $\varepsilon_r = \mu_r$ sphere, there is no energy in the specular reflection direction independently of the polarization of the incident plane wave. The numerous theoretical and experimental studies on zero backscattering that followed Kerker's publication include [58, 92–100]. In Sec. 2.1.4, we introduced the definition of duality symmetry, which states that a system is symmetric under duality transformations if and only if its electric and magnetic responses to the incident illumination are equivalent, which is directly connected to the $\varepsilon_r = \mu_r$ spheres investigated by Kerker. A dual symmetric system preserves helicity (handedness) of the incident illumination in the same manner as translational symmetry preserves linear momentum and cylindrical symmetry preserves the angular momentum. However, duality symmetry alone is not enough for a system to exhibit zero backscattering, but duality coupled with cylindrical symmetry is [94, 100]. These two requirements for a system explain the effect reported by Kerker *et al.*.

Nevertheless, for a practical application such as nanophotonic AR structures for solar cells, one can not directly meet the duality symmetry condition. Full cylindrical symmetry can also not be achieved by the regular nanoparticle arrays. Fortunately, the work reported in [58] established that for a general system, a degree of discrete rotational symmetry $2\pi/n$ for $n \geq 3$ and helicity preservation along the symmetry axis are sufficient to achieve zero backscattering. This result, whose derivation depends only on the symmetries of the system, is essential for the design of AR coatings composed of regularly arranged dielectric nanoparticles for two reasons. First, the discrete rotational symmetry condition establishes the appropriate nanoparticle-array combinations. Secondly, it reduces the duality symmetry condition, which implies that helicity should be preserved irrespective of the illumination direction, to a helicity preservation condition for illumination along the symmetry axis of the system. For the systems where $\varepsilon_r \neq \mu_r = 1$, helicity preservation

can be achieved under particular illumination conditions by tuning the geometrical parameters of the scattering structures. The dielectric nanodisks are suitable candidates for forming the AR array coatings since, for them, the equal electric and magnetic response required for helicity preservation can be achieved by tuning their geometrical aspect ratios given by the height and diameter of the nanodisks. For instance, almost zero reflectance was reported for the periodic square and hexagonal arrangements of optimized Si cylinders for solar cell applications [42, 101]. Additionally, such arrangements of Si nanodisks were employed for applications where high transmission is needed [102, 103].

Notably, the generality of the helicity preservation and discrete rotational symmetry requirements make them helpful in understanding other techniques employed for the AR properties improvement of solar cells. In this regard, we can consider graded-index AR multilayers and chemical texturing, which leads to the formation of micron-sized pyramids on the c-Si wafer front and rear surfaces. Either technique can be understood when applying the symmetry principles. In a system relying on an ARC composed of several different materials indexed by $r = 1, 2, \ldots$, including vacuum, the condition $\varepsilon_r = \mu_r$ is sufficient for duality symmetry and by extension for helicity preservation [100]. Thus, the amount of helicity preservation can be linked to the magnitude of the gradient of the impedance across the system $\nabla \sqrt{\frac{\mu(\mathbf{r})}{\varepsilon(\mathbf{r})}}$ (Eqs. (2.12)-(2.15) in [56]). The textured solar cells' good AR performance can also be explained by a low impedance gradient transition between air and silicon when moving from the tips to the bases of the pyramids. Regarding the required degree of rotational symmetry, the ordered pyramids have C_4 symmetry, while the randomly positioned pyramids achieve an effective cylindrical (C_∞) symmetry. Both cases guarantee a sufficiently high degree of rotational symmetry. The above explanation can be compared with the argument explaining the AR properties of the pyramidal texture by multiple reflections on the facets of the pyramids. This argument is usually made in the context of the ray optics approximation, which relies on the dimensions of the pyramids being large when compared to the operational wavelengths. In contrast, the explanation based on symmetry does not depend on any such approximation. In the case of graded-index multilayered ARCs, the minimization of the impedance gradient across interfaces is apparent. When such layers are applied to flat systems, they possess cylindrical symmetry. The symmetry principles also apply when the multilayered ARCs are combined with pyramidal textures.

In this chapter, we will first consider a system consisting of a square arrangement of nanodisks (Sec. 3.2.2). Initially, we consider the nanodisks made of some artificial material, but later we consider them made from TiO$_2$. For the case when $\varepsilon_r = \mu_r$, we will demonstrate the importance of either condition when deviating from those by breaking either the discrete rotational symmetry or electromagnetic duality symmetry. We will then discuss the optimization result of full-wave simulations for the high-index TiO$_2$ nanodisk square array placed as an AR coating on top of the front part of a HJT solar cell stack and show that helicity preservation and a sufficiently high degree of discrete rotational symmetry are relevant requirements for the design of AR coatings based on dielectric nanoparticle arrays. For this analysis, we will employ the decomposition of the backscattered power into its helicity components (Sec. 3.2.1). We will also analyze a single nanodisk response and its correlation with the AR properties of an array of such nanodisks (Sec. 3.2.3). Moreover, for a simplified system, we will also compare the square arrangement of TiO$_2$ nanodisks with their hexagonal arrangement and show advantages of the latter (Sec. 3.2.4).

Importantly, the TiO$_2$ nanodisks are placed on the front surface of the HJT solar cell stack in an electrically decoupled manner since this allows avoiding the passivation difficulties, which can be imposed by placing dielectric nanoscatterers directly on top of the c-Si

wafer. An additional advantage of using TiO_2 nanodisks is their low absorption in the spectral region relevant for the solar cells. In Sec. 3.3, we will show the application of these favorable properties of the nanodisks and discuss the experimental realization of a HJT solar cell stack coated with TiO_2 nanodisk square array.

3.2 Solar cell with periodic nanodisk coating

3.2.1 Decomposition of the backscattered power into helicity components

If we consider a dual symmetric object or system, we will not observe any coupling between the two helicities of the impinging light. However, since we aim to apply the concept of helicity preservation to a realistic structure, such as a solar cell stack, for which all materials have the magnetic permeability $\mu_r = 1$, some degree of coupling will be present. The figure of merit, which will be used to quantify this coupling and, thus, helicity preservation by the system, is the normalized scattered power of changed helicity.

In Section 2.1.4 we defined the helicity operator Λ and introduced the concept of electromagnetic duality symmetry. As was defined in Eq. 2.47 for Riemann-Silberstein vectors $\mathbf{G}_\pm(\mathbf{r}, \omega)$, the light-matter interaction with a dual symmetric system will not couple the components of the electromagnetic field of opposite handedness. We will now take advantage of the possibility to decompose a general $\mathbf{G}_+$ ($\mathbf{G}_-$) field into a linear combination of left(right)-handed polarized plane waves. Let us consider the power of the electromagnetic field scattered from an object. We can decompose this power into the power in both positive and negative helicity components P_+ (P_-). For a plane wave with momentum $\mathbf{k} = [k_x, k_y, k_z]$, the polarization vectors which correspond to the positive and negative helicity components are (Sec. 2.2.4 in [54]):

$$\hat{\mathbf{e}}_\pm(\mathbf{k}) = \frac{1}{\sqrt{2}}[\hat{\mathbf{s}}(\mathbf{k}) \pm \hat{\mathbf{p}}(\mathbf{k})], \tag{3.1}$$

where

$$\begin{aligned}
\hat{\mathbf{s}}(\mathbf{k}) &= i\left[\sin(\phi)\hat{\mathbf{x}} - \cos(\phi)\hat{\mathbf{y}}\right], \\
\hat{\mathbf{p}}(\mathbf{k}) &= -\cos(\theta)\cos(\phi)\hat{\mathbf{x}} - \cos(\theta)\sin(\phi)\hat{\mathbf{y}} + \sin(\theta)\hat{\mathbf{z}},
\end{aligned} \tag{3.2}$$

with

$$\begin{aligned}
\theta &= \arccos(k_z/k), \\
\phi &= \arctan(k_y/k_z), \\
k &= \sqrt{k_x^2 + k_y^2 + k_z^2}.
\end{aligned} \tag{3.3}$$

The $\hat{\mathbf{s}}(\mathbf{k})$ and $\hat{\mathbf{p}}(\mathbf{k})$ polarization vectors in Eq. 3.2 correspond to the TE and TM polarizations, respectively.

We employ the angular spectrum representation introduced in Sec. 2.1.3, and the backscattered field in real space obtained via full-wave simulation is then Fourier transformed. Each of the plane waves, which compose the backscattered field, can then be decomposed into its two helicity components in the following way:

$$\mathbf{E}(\mathbf{k})\exp(i\mathbf{k}\cdot\mathbf{r}) = [\mathbf{E}_+ + \mathbf{E}_-](\mathbf{k})\exp(i\mathbf{k}\cdot\mathbf{r}), \tag{3.4}$$

with

$$\mathbf{E}_\pm(\mathbf{k}) = \left\{[\hat{\mathbf{e}}_\pm(\mathbf{k})]^\dagger \mathbf{E}(\mathbf{k})\right\}\hat{\mathbf{e}}_\pm(\mathbf{k}) = E_\pm\hat{\mathbf{e}}_\pm(\mathbf{k}). \tag{3.5}$$

Subsequently, the expression for the normalized powers $P_+(\mathbf{k})$ and $P_-(\mathbf{k})$ corresponding

to both helicities reads as

$$P_{\pm}(\mathbf{k}) = \frac{|E_{\pm}|^2}{2Z_0 P_{\text{in}}}, \tag{3.6}$$

where Z_0 is the impedance of the medium and P_{in} is the power of the incident plane wave to which the backscattered power is normalized. This power is expressed as:

$$P_{\text{in}} = \frac{|\mathbf{E}_0|^2}{2}\sqrt{\varepsilon_0/\mu_0} = \frac{|\mathbf{E}_0|^2}{2Z_0}. \tag{3.7}$$

In the above equation, $\mathbf{E}_0$ is the amplitude of the incident plane wave. Summation over all $\mathbf{k}$ yields the total powers P_+ and P_- associated with positive and negative helicity, respectively.

The equations above allow to understand better the definition of helicity operator given by Eq. 2.45. Let us go back to Eq. 3.1. If we consider a wave vector in the $\hat{\mathbf{z}}$ direction $\mathbf{k} = [0,0,k]$, we obtain the polarization vector $\hat{\mathbf{e}}(\mathbf{k}) = \frac{1}{\sqrt{2}}(-\hat{\mathbf{x}} - i\hat{\mathbf{y}})$ corresponding to the left-handed circular polarization (helicity $+1$), and $\hat{\mathbf{e}}(\mathbf{k}) = \frac{1}{\sqrt{2}}(\hat{\mathbf{x}} - i\hat{\mathbf{y}})$ corresponding to the right-handed circular polarization (helicity -1). Analogously, for a wave vector in the $-\hat{\mathbf{z}}$ direction $\mathbf{k} = [0,0,-k]$, we arrive at the polarization vectors $\hat{\mathbf{e}}(\mathbf{k}) = \frac{1}{\sqrt{2}}(\hat{\mathbf{x}} - i\hat{\mathbf{y}})$ and $\hat{\mathbf{e}}(\mathbf{k}) = \frac{1}{\sqrt{2}}(-\hat{\mathbf{x}} - i\hat{\mathbf{y}})$ corresponding to left-handed circular (helicity $+1$) and right-handed circular polarization (helicity -1), respectively. Notably, the polarization vector corresponding to the positive helicity for $\hat{\mathbf{z}}$ direction is identical to the polarization vector corresponding to the negative helicity for $-\hat{\mathbf{z}}$ direction, and vice versa. If we go back to the definition of helicity (Eq. 2.45 in Sec. 2.1.4), we can see that the property mentioned above illustrates the meaning of helicity, such that the same sense of rotation coupled with an opposite linear momentum leads to an opposite handedness. Keeping this interpretation of the helicity definition in mind, we can revisit the formulation of the conditions sufficient for zero backscattering, which were introduced in [58] and discussed in Sec. 2.1.4. If we consider a plane wave that has a definite polarization handedness and impinges on an object whose degree of rotational symmetry is high enough ($C_{n\geq 3}$), we would expect the light reflected and transmitted along the symmetry axis to have the same angular momentum as the incident plane wave. From this, it follows that the reflected plane wave must have flipped helicity (opposite to the one of the incident plane wave), since the linear momentum is opposite to the one of the incident plane wave while the angular momentum stays the same. Thus, if, in addition to having a sufficiently high rotational symmetry, the object does not allow helicity change along the symmetry axis, the backscattering will be zero. This holds for both positive and negative helicity, and since an arbitrarily polarized plane wave can always be expressed as a weighted sum of the two helicities, it implies that the backscattering at normal incidence for the object satisfying the symmetry condition will be zero independently of the polarization of an incoming plane wave.

3.2.2 Nanodisks in a square lattice

Having discussed how one can quantify the ability of the system to preserve helicity, we will apply it to a specific structure. The schematic image of the structure considered in the simulations is given in Fig. 3.1. The titanium dioxide (TiO$_2$) nanodisks arranged in a square lattice are placed on top of a HJT solar cell stack. We note here that a semi-infinite c-Si substrate is assumed, and when referring to a HJT solar cell stack, we assume the front part of thereof. For simplicity, the term we use throughout this section will be "HJT solar cell stack". Refractive indices of TiO$_2$, ITO, and c-Si were taken from [104], [105], and [72], respectively. The refractive index data for the composite a-Si:H(i,n^+) layer were obtained in Meyer Burger Research AG employing ellipsometry. The corresponding
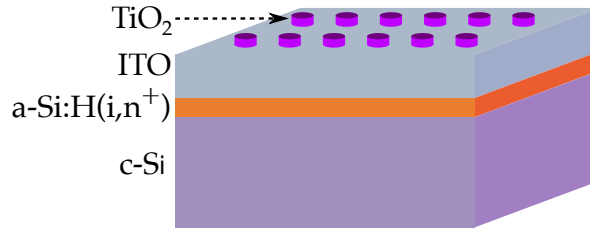
FIGURE 3.1: Schematic image of a HJT solar cell stack with a TiO$_2$ nanodisk coating. The nanodisks are arranged in a square lattice with a unit cell parameter $a = 500$ nm. The height and diameter of an individual disk are 100 nm and 300 nm, respectively. The composition of the solar cell stack considered in the simulations is as follows from bottom to the top: A semi-infinite c-Si substrate, an absorbing 300 nm thick film of c-Si, an 8 nm thick film of a-Si:H (passivating intrinsic and n^+-doped), and a 50 nm thick film of ITO serving as a front contact. Adapted from [P1]. © 2019 American Physical Society.

graph can be found in Appendix A. In the simulations discussed in this section, the illumination is a plane wave whose helicity is -1 (right-handed polarized light). All calculations were performed using FEM.

First, we will show how the degree of rotational symmetry and helicity influence the AR properties of the system. We will do so on an example of hypothetical materials with relative permittivity equal to relative permeability ($\varepsilon_r = \mu_r$) and compare reflectance in the case of the systems with different symmetry of the nanodisks' arrangement. The nanodisks are either arranged in a square array (C_4), which satisfies the rotational symmetry condition, or a rectangular array (C_2) that does not. Reflectance is calculated via the total electromagnetic energy flux Φ, which is obtained through integration of the electromagnetic energy flux density (Poynting vector) across the layer interfaces, which is subsequently normalized by the incoming flux:

$$R = \frac{\text{Re}\{\Phi\}}{P_{\text{in}} \cdot A},$$
(3.8)

where A is the area of the computational domain, i.e., the unit cell of the lattice.

Figure 3.2(a) shows the result of the performed simulations. For a fair comparison, the ratio of the nanodisks' surface area to the unit cell area of the lattice is kept the same for both arrays. The materials are assumed to have $\varepsilon_r = \mu_r$, and the geometry is the same as it is illustrated in Fig. 3.1. The properties of these artificial materials are assigned in the following way: The electric permittivities correspond to those of the natural materials indicated in Fig. 3.1, and their magnetic permeabilities are taken to be equal to the permittivities. The illumination is along the symmetry axis of the nanodisks' axis, and the momentum of the circularly-polarized incident plane wave is normal to the plane of a coated HJT solar cell stack. Since the considered wavelength range is between 750 nm and 1100 nm, the periodicity of the lattices is always smaller than the wavelength in free space. This means that reflectance is purely specular, and only the 0$^{\text{th}}$ diffraction order is present. The results in Fig. 3.2(a) confirm that the system needs to have a high enough degree of rotational symmetry to achieve zero-backscattering. While the system for which the nanodisks are arranged in a square array yields zero backscattering, a system with the nanodisks arranged in a rectangular array does not, although the system is dual symmetric with $\varepsilon_r = \mu_r$.

Next, it is important to consider the situation when the perfect helicity preservation is
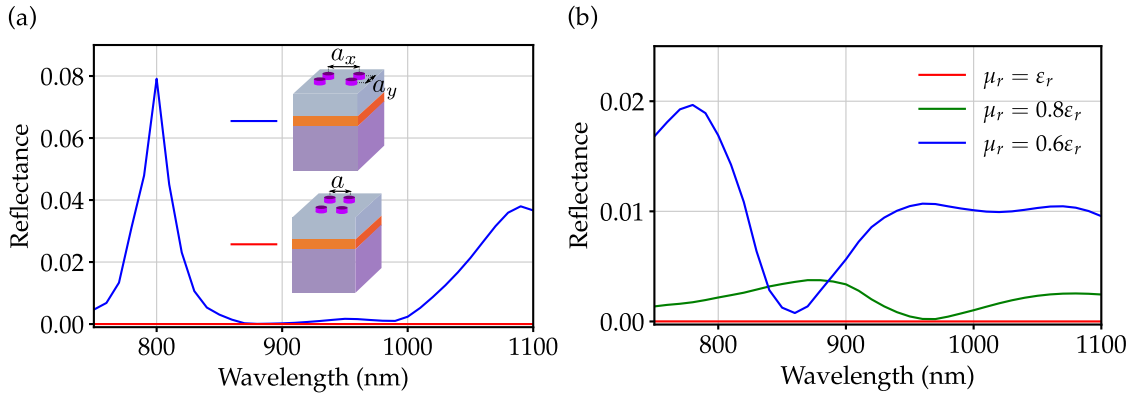
(a)

(b)

FIGURE 3.2: (a) Reflectance of dual-symmetric systems with rectangular (C_2) and square (C_4) arrangement of the strictly dual nanodisks under the normal incidence of the illumination. Both systems are made of hypothetical materials with electric permittivities ε_r corresponding to those of natural materials with magnetic permeabilities set to $\mu_r = \varepsilon_r$ such that perfect duality symmetry could be achieved. The detailed information on the natural materials and geometry can be found in Fig. 3.1. Here, the simplified schematics of the considered unit cells are shown in the inset: The C_4 unit cell parameter is $a = 500$ nm, and the C_2 unit cell parameters are $a_x = 806.5$ nm and $a_y = 310$ nm, respectively. (b) Reflectance of the system with square (C_4) arrangement of the nanodisks upon duality breaking. Colors represent the different ratios of relative permeability μ_r to relative permittivity ε_r. Adapted from [P1]. © 2019 American Physical Society.

violated and how it influences reflectance when the rotational symmetry condition ($C_{n \geq 3}$) is still satisfied. To address this issue, we consider the case when perfect duality is broken. Figure 3.2(b) provides the result of these simulations. Here, reflectance of a C_4 system with varying μ_r/ε_r ratios is shown. It is clear from these results that the AR properties get worse with the materials becoming less dual symmetric.

From Figs. 3.2(a) and (b) we can deduce the design requirements for an AR coating: The system must possess a high enough degree of discrete rotational symmetry and should preserve helicity. The symmetry requirement is easy to fulfill, while the lack of the materials with $\varepsilon_r = \mu_r$ in the relevant spectral region does not allow us to meet the helicity preservation condition in such a way. However, one can still achieve helicity preservation for specific illuminations for systems made from realistic materials with $\varepsilon_r \neq \mu_r = 1$ when the system's geometry is appropriately optimized. Such optimal geometry should lead to an equal electric and magnetic response of the system for the considered illumination. For the high-index dielectric nanodisks, which we consider here, the optimization of the geometry by tuning their aspect ratios results in the desired outcome at a particular frequency in case of the illumination along their symmetry axis [102, 103, 106]. This, however, is not strictly equivalent to electromagnetic duality symmetry. In the case of dual symmetric nanodisk, helicity will be preserved omnidirectionally. For example, electromagnetically small dielectric spheres can be designed such that they achieve a high degree of helicity preservation independently of the illumination direction at a certain frequency [94]. Nevertheless, for the spheres, this does not happen at the resonant frequencies compared to the nanodisks.

After demonstrating the importance of satisfying the conditions needed to minimize backscattering, we now switch to the system introduced in Fig. 3.1 when it is composed of natural materials with $\varepsilon_r \neq \mu_r = 1$. This system represents a HJT solar cell with a square
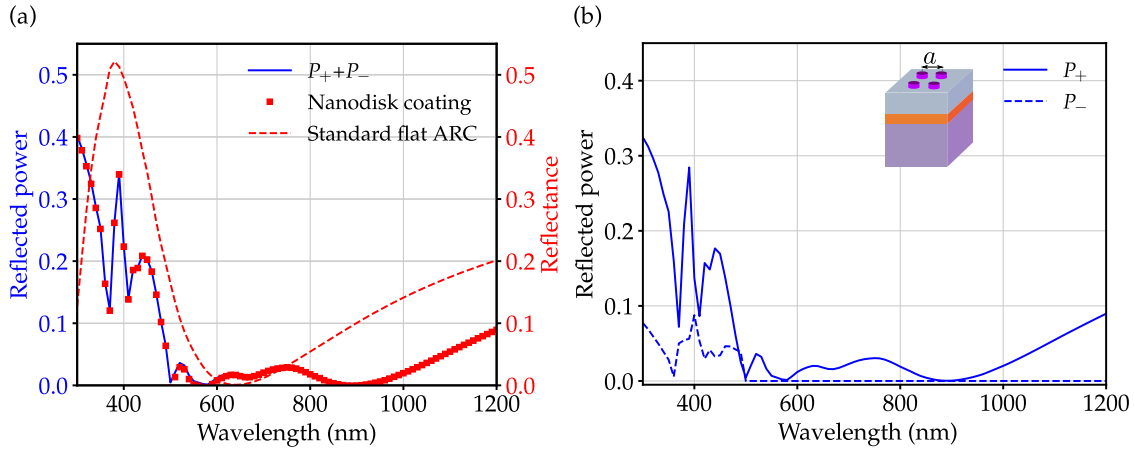
(a)

(b)

FIGURE 3.3: (a) Reflectance as a function of wavelength for an optimized nanocoated structure and a standard flat HJT solar cell with optimized ITO thickness under the normal incidence of the illumination. To ensure the validity of the result, reflectance of the coated HJT cell is compared to the sum of the normalized powers of two helicities P_+ and P_-. (b) Normalized reflected powers of positive and negative helicity P_+ and P_- for an optimized nanocoated structure. The system is schematically shown in the inset. The detailed information on natural materials as well as the geometrical parameters is given in Fig. 3.1. Adapted from [P1]. © 2019 American Physical Society.

TiO$_2$ nanodisk array placed on its front surface. Reflectance of the optimized system is shown in Fig. 3.3(a). As expected, the sum of the normalized total backscattered powers of both helicities P_+ and P_-, which is also shown in this graph, is equal to reflectance calculated through the EM energy flux. The AR performance of the coated HJT solar cell is compared to the AR performance of the same cell coated with a standard optimized flat ARC. As was previously discussed in Sec. 2.2.2, the ITO layer of the reference HJT solar cell serves as both the front contact and ARC. The optimal thickness of such an ARC is 80 nm, and minimal reflectance of a HJT solar cell with this coating is achieved around $\lambda = 600$ nm.

The system's geometrical parameters were optimized to achieve minimal current density loss stemming from reflectance upon normally incident illumination. The following equation defines the current density loss:

$$J_{\text{loss}} = q \int_{\lambda_1}^{\lambda_2} \phi_{\text{AM1.5G}}(\lambda) R(\lambda) \text{IQE}(\lambda) d\lambda, \tag{3.9}$$

where $\phi_{\text{AM1.5G}}(\lambda)$ is the spectral photon flux. The AM1.5G spectrum data were taken from [66], and the simulated reflectance $R(\lambda)$ was interpolated accordingly. We note that IQE(λ) was assumed to be unity. In the optimization process, the thickness of an ITO layer and the height of the individual nanodisk were varied in 10 nm steps, while the radius of the individual nanodisk was varied in 25 nm steps. The period of the square lattice was varied in 100 nm steps, and it was accommodated to the radii of the nanodisks such that the surface area ratio stayed roughly unchanged.

During the optimization, three of the four geometrical parameters were fixed, and the current loss density was calculated as a function of the fourth parameter. When the optimal value of this geometrical parameter was found, it was fixed, and another parameter was subsequently varied. These iterations lead to a set of geometrical parameters giving the minimal current density loss due to reflectance. The optimal geometrical

parameters of the investigated structure comprise 300 nm individual nanodisk diameter, 100 nm individual nanodisk height, 50 nm ITO layer thickness, and 500 nm square array period. The current density loss of the optimized system calculated using Eq. 3.9 yields 1.7 mA·cm^{-2}. This value is compared to the current density loss in the case of an optimized standard flat reference. Such a reference yielded a loss of 5.1 mA·cm^{-2}.

Although the sampling in the optimization process was quite coarse, we note that the optimization results are robust up to 20 % with respect to the change of the geometrical parameters' values, including the ITO layer thickness and the dimensions of an individual nanodisk. The changes in the ITO layer thickness and the height of the individual nanodisks result in slight shifts of the reflectance minima. Varying the individual nanodisks' radii leads to more significant shifts of the minima, although the integrated reflectance over the whole spectral range is only slightly changed. While deviating from the optimal parameter set results in an increase of the current density loss value, the difference between the latter and the current density loss of the standard optimized flat reference stays considerably large. Such stability of the geometrical parameters concerning the AR properties improvement is especially important for experimental realization of the structure since, in this case, the imperfections in the fabrication process are less impactful.

Figure 3.3(b) demonstrates the normalized total powers that are reflected into the air half-space for both helicities. As was described in Sec. 3.2.1, to analyze the helicity content of the reflected light, we decompose the backscattered field into plane waves corresponding to negative and positive helicities. Subsequent summation over all wave vectors yields powers P_+ and P_-. The helicity content of the reflected light shown in Fig. 3.3(b) is expected. When the wavelengths within the considered spectral range exceed the lattice constant $a = 500$ nm of the square nanodisk array, only the 0th diffraction order is allowed. This means that reflectance in the wavelength region with $\lambda > 500$ nm is purely specular. Then, as can be seen in Fig. 3.3(b), the C_4 discrete rotational symmetry of the array prohibits the reflected light from having the component with the same helicity as the illumination (helicity -1) [58]. This manifests itself in the strictly zero values of P_- in the discussed region of the spectrum, and all the reflected power is of changed (positive) helicity. In the spectral region with $\lambda > 500$ nm, the reflection suppression is equivalent to the helicity preservation by the investigated system. Let us now look at the part of the spectral region with $\lambda < 500$ nm. Here, higher diffraction orders are present, thus allowing for the backscattered light to be of mixed helicity (both P_- and P_+ are present). This is the consequence of the fact that the helicity flip upon reflection from the system with $C_{n \geq 3}$ symmetry occurs only when the momenta of both incident and reflected plane waves are aligned with the symmetry axis [58], which is not true for nonzero diffraction orders.

3.2.3 Scattering by an isolated nanodisk

To have more insight into the analysis of an optimized C_4 nanodisk array which was discussed in Sec. 3.2.2, we now will consider the system consisting of an isolated TiO$_2$ nanodisk placed on top of a HJT solar cell stack. The result of this calculation is shown in Fig. 3.4. First, we computed the specularly reflected powers corresponding to the positive and negative helicity. As can be seen from Fig. 3.4(a), only the power corresponding to the flipped helicity (P_+) is nonzero. As was discussed in Sec. 3.2.2, this is expected from the system whose rotational degree of symmetry is sufficiently high independently of its helicity preservation properties. For the system consisting of an isolated nanodisk on a solar cell substrate, this symmetry is C_∞. The backscattering by the system is practically suppressed in the region close to $\lambda = 500$ nm, where the backscattered power corresponding to the flipped helicity P_+ is approaching zero. At the frequencies where
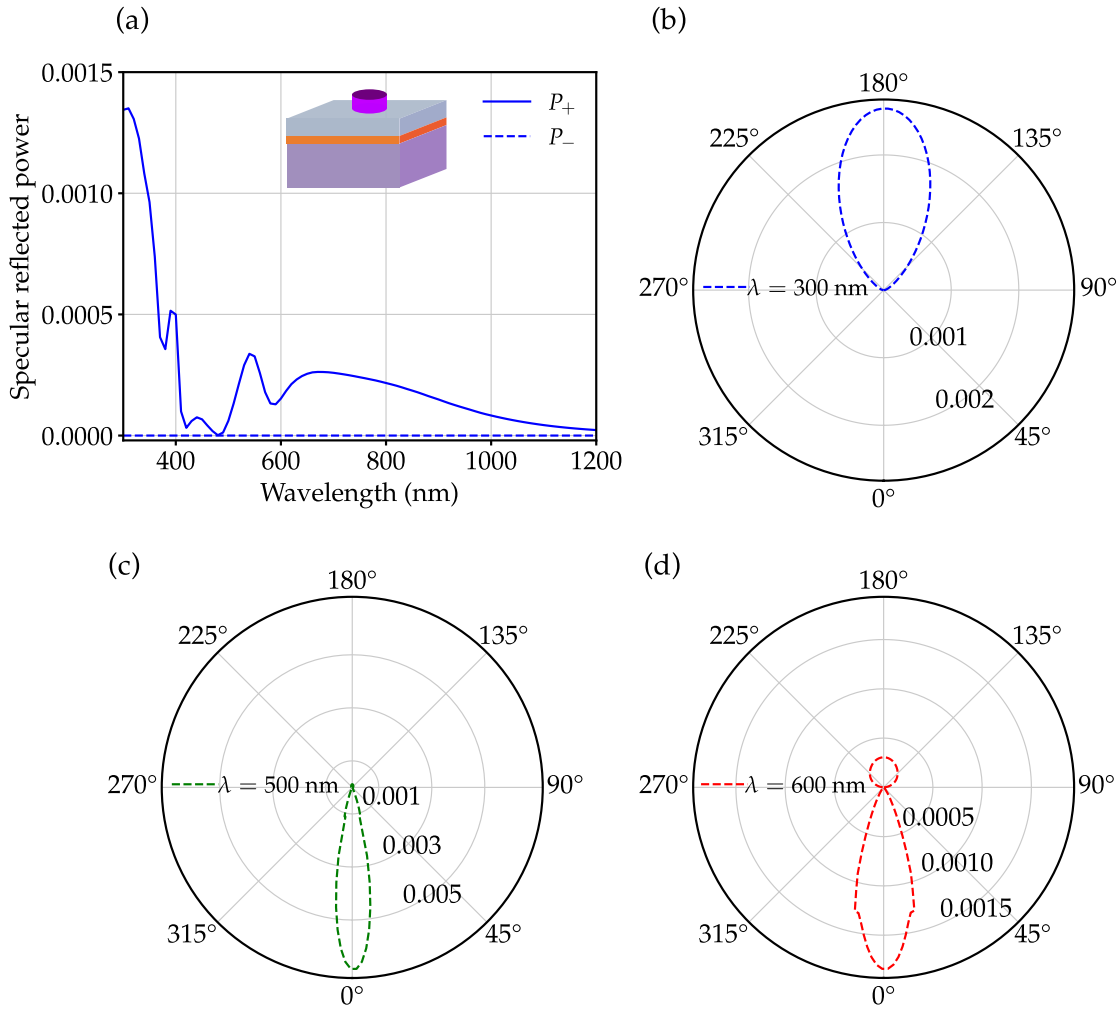
FIGURE 3.4: (a) Normalized specularly reflected powers P_+ and P_- corresponding to positive and negative helicity for an isolated nanodisk on top of a HJT solar cell layer stack under normal incidence of the illumination. The system is schematically shown in the inset and has the same geometrical parameters and material composition as it is shown in Fig. 3.1 except that we consider here an isolated nanodisk. (b)-(d) Polar plots of the far field intensities at wavelengths $\lambda = 300$, 500, and 600 nm, respectively. The far field intensities are computed in a plane that contains the symmetry axis of the nanodisk. Adapted from [P1]. © 2019 American Physical Society.

the values of P_+ are sufficiently small, the system as a whole is approaching perfect helicity preservation.

Figures 3.4(b)-(d) demonstrate the far field intensities at three selected wavelengths. For $\lambda = 300$ nm, basically, all the light is scattered back into the air hemisphere. For $\lambda = 600$ nm, the portion of the backscattered light is significantly reduced compared to the portion of the light scattered towards the solar cell substrate. However, at $\lambda = 500$ nm, the system approaches perfect helicity preservation, and nearly all the scattering is towards the c-Si substrate hemisphere. Since the degree of helicity preservation in designs based on materials with $\varepsilon_r \neq \mu_r = 1$ relies on the nanodisks' optimized geometrical parameters, it depends on the frequency as well as the illumination direction. Thus, for the designs based on natural materials, the deviation from the optimal frequency will lead to the degradation of the degree of helicity preservation and an increase of the backscattering

by the system.

3.2.4 Increased symmetry of the nanodisks' arrangement

As was established in Sec. 3.2.3, the helicity change is unavoidable for objects with $\varepsilon_r \neq \mu_r = 1$ when moving away from the optimal frequency. Thus, it is worth investigating if this shift can be compensated to some extent when the degree of discrete rotational symmetry of the nanodisks' arrangement is increased. We now will evaluate the response of the simplified system consisting of a c-Si silicon substrate coated with the TiO_2 nanodisk arrays. This choice of the system facilitates a more straightforward analysis of the impact of the nanodisks' arrangement symmetry since it allows to isolate other factors such as optimization of the thicknesses of other layers and their effect on the optical response.

We consider the arrangement of the nanodisks in square and hexagonal lattices. As in Sec. 3.2.2, we start with the systems composed of hypothetical materials. The electric permittivity of the substrate and the nanodisk correspond to those of the natural materials. The magnetic permeabilities are varied in the range of 60 % to 90 % of the permittivities. Figure 3.5(a) shows the result of our analysis. As expected, reflectance of both arrays is growing with the increased mismatch between magnetic permeability and electric permittivity. One can see that the hexagonal arrangement of the nanodisks leads to smaller reflectance across the entire spectral range for all ratios of $\varepsilon_r = \mu_r$. This effect persists even when we move significantly away from the duality point ($\mu_r = 0.6\varepsilon_r$).
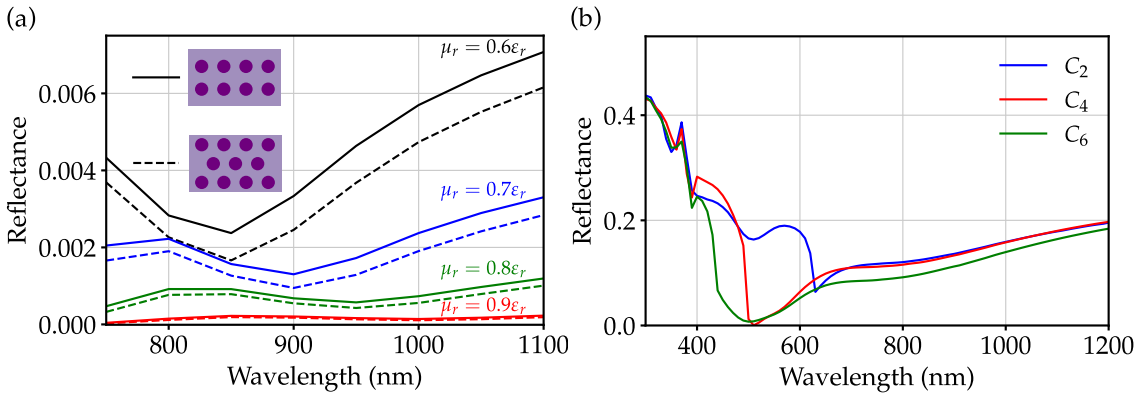
FIGURE 3.5: (a) Reflectance of a c-Si substrate coated with TiO_2 nanodisk arrays with C_4 (bold lines) and C_6 (dashed lines) symmetries under the normal incidence of the illumination. Both systems are made of hypothetical materials with electric permittivities ε_r corresponding to those of natural materials, while with magnetic permeabilities μ_r are varied. Colors represent the different ratios of relative permeability μ_r with respect to relative permittivity ε_r. (b) Reflectance of a c-Si substrate coated with the TiO_2 nanodisk arrays of different symmetries in case of natural materials ($\mu_r = 1$). The rectangular (C_2), square (C_4), and hexagonal (C_6) lattices are considered. The lattice constants are $a_x = 625$ nm, $a_y = 400$ nm for C_2, $a = 500$ nm for C_4, and $a = 500$ nm for C_6. Adapted from [P1]. © 2019 American Physical Society.

Now we switch to the case of natural materials with $\varepsilon_r \neq \mu_r = 1$. Figure 3.5(b) shows reflectance in the case of the rectangular (C_2), square (C_4), and hexagonal (C_6) arrangement of the nanodisks. In the case of a rectangular array, the unit cell area is matched to the one of the square array, while for the hexagonal array, the lattice constant is the same as for the square array ($a = 500$ nm). For the square nanodisk array, the nonzero diffraction orders disappear in the air half-space when the wavelength is equal to or exceeds the lattice

TABLE 3.1: Integrated reflectance of the TiO$_2$ nanodisk arrays of different symmetries placed on top of the c-Si substrate. Reprinted from [P1]. © 2019 American Physical Society.

	C_2 $a_x = 625$ nm, $a_y = 400$ nm	C_4 $a = 500$ nm	C_6 $a = 500$ nm	C_6 $a = 537$ nm
Integrated reflectance (nm)	161.01	144.37	118.24	141.77

constant. For the hexagonal nanodisk array, the wavelength from which the nonzero diffraction orders vanish is $\lambda = 0.5\sqrt{3}a$. For lattice constant $a = 500$ nm, this yields 433 nm.

As expected, the system with the rectangular nanodisk array, which does not satisfy the discrete rotational symmetry condition, leads to higher reflectance than the other two arrays. We can see that the higher degree of rotational symmetry of the hexagonal nanodisk array improves the AR properties of the system in comparison to the square nanodisk array. To exclude the effect of increased filling fraction of the TiO$_2$ nanodisks and see only the change in the AR properties coming from symmetry, we also consider the case when the ratio of the nanodisks surface area to the area of the unit cell is kept the same for the square and hexagonal nanodisks' arrangements. To quantify the difference in the performance of the systems with various symmetries of the nanodisk arrays, we consider integrated reflectance in nm, which is calculated by the following equation:

$$\text{IR} = \int_{\lambda_1}^{\lambda_2} \text{R}(\lambda)d\lambda. \tag{3.10}$$

Table 3.1 shows the result of this calculation. The values of the integrated reflectance demonstrate an expected decrease with an increasing degree of rotational symmetry of the arrays. However, the integrated reflectance of the hexagonal array compared to the square array becomes significantly smaller when the filling fraction of TiO$_2$ nanodisks is the same. Still, increasing the degree of symmetry of the array leads to the improved AR properties of the system.

3.3 Experimental realization of a solar cell with the nanodisk coating

After discussing the mechanism behind the broadband reflection suppression by the systems with nanodisk coatings, we will now show the experimental realization of such a system. Here, we demonstrate the results of a multi-step fabrication process of a structured rear emitter HJT solar cell stack utilizing electron beam (e-beam) lithography and characterize the fabricated sample.

3.3.1 Fabrication process

The solar cell precursor and the target dimensions of the individual nanodisks and array pitch are the same as in Fig. 3.1, with the difference that the a-Si:H and ITO layers placed symmetrically to the ones on the front were deposited on the rear of the c-Si wafer. To ensure sufficiently flat morphology of the precursor's surface, we used the chemically-mechanically polished *n*-type c-Si wafers produced by TOPSIL. The wafers had thicknesses of around 280 μm and a diameter of 100 mm. The a-Si:H(i,n^+) and ITO layers on the front, and a-Si:H(i,p^+) and ITO layers on the rear of a precursor were deposited via PECVD and PVD, respectively. The thicknesses of the rear a-Si:H and ITO layers were comparable to their counterparts on the front of the solar cell stack.

Two samples were fabricated using the same process for the chips that were laser cut from one solar cell precursor. The dimensions of an individual chip were 22 by 22 mm^2. For the sample which was subsequently characterized, the nanodisk array covered 2 by 4 mm^2 area. For the sample which was fabricated to produce the top and cross-section scanning electron microscopy (SEM) images, the nanodisk array covered 0.5 by 0.5 mm^2 area.
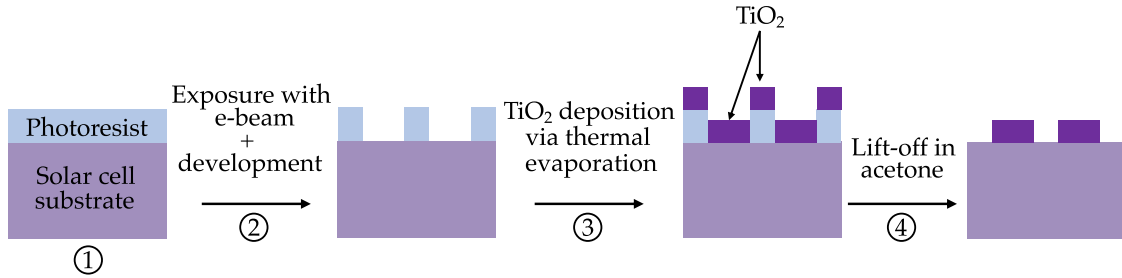

FIGURE 3.6: Illustration of the fabrication process of the square TiO$_2$ nanodisk array on top of a HJT solar cell by e-beam lithography. The flow of the process was the following: (1) HJT solar cell precursor was spin-coated by the PMMA photoresist; (2) spin-coated sample was exposed with e-beam and subsequently developed; (3) TiO$_2$ was deposited on top of the developed sample using the thermal evaporation; (4) photoresist was removed through the lift-off in acetone which was facilitated by placing the sample in the ultrasonic bath. The precursors were prepared by Meyer Burger Research AG staff in Hauterive, Switzerland. Steps (1) and (2) were performed by Dr. Silvia Diewald from CFN at KIT. Step (3) was performed by Dr. Somayeh (Sara) Moghadamzadeh from LTI at KIT. SUSS MicroOptics SA in Hauterive, Switzerland gave access to their clean room for step (4).

Figure 3.6 illustrates the steps of the fabrication process used to create a square TiO$_2$ nanodisk array on top of a flat HJT solar cell precursor. In the first step, the front surface of a flat HJT solar cell precursor was spin-coated with a poly(methyl methacrylate) (PMMA) double-layer photoresist. The photoresist double stack was prepared using PMMA (AR-P 642.06, 200 K, Anisol) and PMMA (AR-P 672.045, 950 K, Anisol) with a total targeted thickness of around 400 nm. Then, the sample was structured by the e-beam with the exposure dose 450 μC·cm^{-2}, using the system with an acceleration voltage of 50 kV (JEOL JBX-5500FS 50 kV e-beam writer). After the development of the exposed sample, the non-exposed volume was left since the used photoresist was positive. Next, the TiO$_2$ thin film was deposited on the structured photoresist. Even though the refractive index of the resulting TiO$_2$ layer can be higher while using atomic layer deposition (ALD), the layer was deposited by thermal evaporation. The refractive index data for TiO$_2$ can be found in Appendix A. This technique was chosen since ALD leads to the deposition of a conformal film and would require using reactive-ion etching (RIE) to structure it, which leads to additional steps and complicates the fabrication process. However, thermal evaporation allows removing the photoresist through lift-off in acetone. The lift-off process was facilitated by immersing the sample into the ultrasonic bath in the time increments of 1 min, and after each iteration, the optical microscope was used to check if PMMA still covered some parts of the structured area. Typically, it was possible to remove the photoresist completely after performing two iterations of this process.

Figure 3.7 shows SEM images of the fabricated nanostructure, where the images (a)-(b) show the top view of the fabricated sample, and the images (c)-(d) – the cross-section
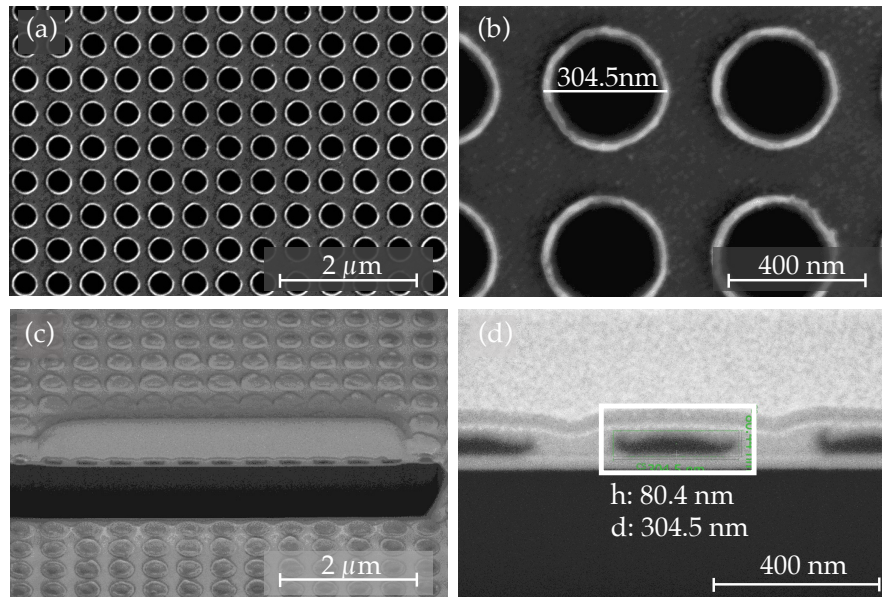
FIGURE 3.7: SEM images of the TiO$_2$ nanodisk coating fabricated by e-beam lithography on the front surface of a HJT solar cell layer stack: (a)-(b) top view, (b) cross-section of the structure (generated by FIB). The targeted array parameters were: Pitch of 500 nm, nanodisk diameter of 300 nm, and nanodisk height of 100 nm. While the pitch of the fabricated nanodisk array met the target value of 500 nm and the deviation from the optimal diameter value was insignificant, there was a visible deviation from the optimal height of the nanodisks. The height h and diameter d of the fabricated nanodisks are indicated in the image (d). For this structure, which was fabricated specifically for imaging purposes, the nanodisk array covered the area of 0.5 by 0.5 mm^2. The images were taken by Silvia Biselli at CSEM in Neuchâtel, Switzerland.

which was generated using focused ion beam (FIB). From the top view images, it can be seen that the diameter and pitch of the nanodisk array are in good correspondence with the optimal design. However, the height of the nanodisks is lower than the target value [Fig. 3.7(d)], which could be due to the photoresist shadowing effects during the thermal evaporation of TiO$_2$. Nevertheless, since the optimization results introduced in Sec. 3.2.2 are quite robust to change in the nanodisk array parameters' values, this deviation is not critical for the AR properties of the nanocoating.

3.3.2 Sample characterization

We then characterized the fabricated samples by measuring reflectance and photoluminescence (PL). Below is a brief description of the techniques and tools employed for characterization:

Spectrophotometery:

Spectrophotometry is the technique that allows measuring the wavelength-dependent optical response (reflectance and transmittance) of thin films. In a spectrophotometer, the polychromatic light source is shone onto a monochromator (e.g., a grating), which splits it into a range of individual wavelengths. The diffracted light is then split into two beams by a beam splitter and subsequently passes a chopper. The reference beam travels directly into an integrating sphere where it is detected while the sample beam first passes the sample. The intensity ratio between these two beams yields reflectance or transmittance. The integrating sphere, whose inner surface is covered by a diffusely reflective material,

allows evenly distributing the incoming light through multiple reflections. The resulting integrated radiation then reaches the detector. To measure reflectance, we used two commercial tools produced by Perkin Elmer: LAMBDA 750 UV/Vis/NIR (at Meyer Burger Research AG in Hauterive, Switzerland) and LAMBDA 1050 UV/Vis/NIR (in LTI at KIT). During the measurements by the latter spectrophotometer, an aperture was placed in the beam path to adjust the beam spot size such that the measurement for the small area sample could be performed.

Photoluminescence imaging:

Since it is a contactless and fast measurement technique, PL imaging is widely used in the PV industry to access the quality of c-Si wafers as well as the finished solar cells. In a typical PL imaging setup, the light from a source (e.g., LED arrays) hits the sample, after which the photons whose energy is above the band gap of the semiconductor material are absorbed, exciting the electrons to the conduction band. Subsequently, these electrons radiatively recombine with the holes, and the light is emitted from the investigated sample. A CCD camera then captures this light after going through a longpass filter. The commercial tool used to produce the PL images was GREATEYES LumiSolarCell EL PL IR system (at Meyer Burger Research AG in Hauterive, Switzerland).

Figure 3.8 shows the result of the reflectance measurements over a broad spectral region. Here we compare reflectance of the structured HJT solar cell stack to reflectance of two references. The first reference had the same ITO thickness of 50 nm as the structured sample ITO (adapted flat ARC reference). The measurement for this reference was conducted for the same chip on which the TiO_2 nanodisk structure was written. The second reference was the one that had an optimized ITO thickness of 80 nm (standard flat ARC reference). It should be noted that the second reference was not fabricated using the mechanically polished wafers, but flat Czochralski n-type c-Si wafers, and it was a finished device that had screen printed silver contact fingers but no busbars.
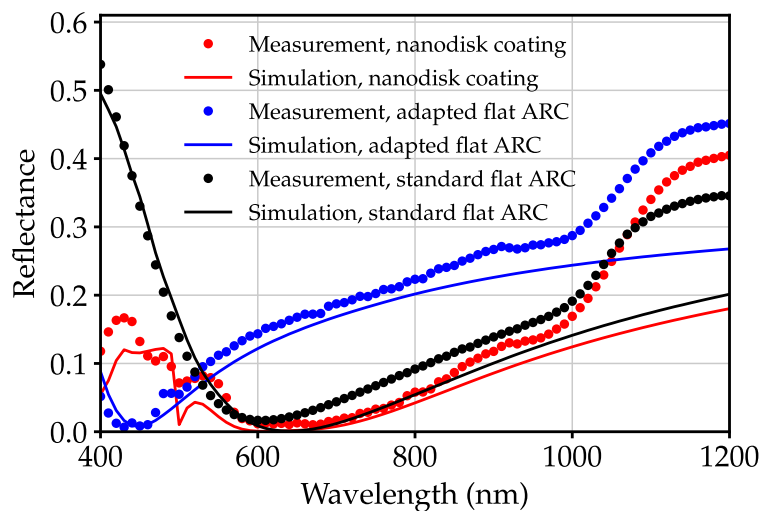
FIGURE 3.8: Reflectance of the HJT solar cell stack coated with nanodisk array compared to reflectance of the adapted flat ARC (ITO thickness of 50 nm) and standard flat ARC (ITO thickness of 80 nm) references. All the simulations shown in this graph were performed using FEM.

For the area with the nanodisk structure and the adapted ARC reference, the simulated reflectance is in good accordance with the measured spectra. For the standard ARC reference, there is a stronger deviation between the simulated reflectance and the measured one. This is most likely caused by the shadowing introduced by the contact fingers.

For all three configurations, there is a substantial deviation of the measured reflectance from the simulated one at long wavelengths related to reflection from the back surface of the solar cell, which is not taken into account in the simulations. Table 3.2 shows the calculated current density loss for the structured solar cell stack and both references in case of the simulated and measured reflectance (see Eq. 3.9). For both the simulated and measured optical performance, the structured HJT solar stack outperforms both the adapted ARC reference and the standard ARC reference, although, as expected, the difference in performance with the former reference is more significant. Taking into account the shading introduced by the contact fingers and assuming it to be 5%, the value for the current density loss of the standard ARC reference would decrease to $6.1 \text{ mA} \cdot \text{cm}^{-2}$. Even in this case, the structured solar cell stack would introduce smaller reflection loss.

TABLE 3.2: Current density loss due to simulated and measured reflectance of a HJT solar cell with the standard flat ARC, the adapted flat ARC, and the TiO$_2$ nanodisk coating.

	Standard flat ARC	Adapted flat ARC	Nanodisk coating
$J_{\text{loss,sim}}$ (mA·cm^{-2})	4.7	7.6	3.0
$J_{\text{loss,meas}}$ (mA·cm^{-2})	6.4	9.4	5.0
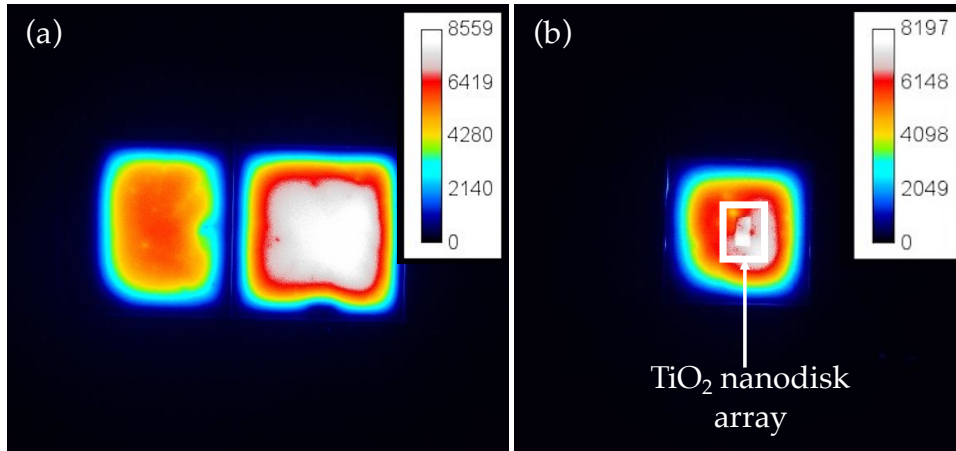
FIGURE 3.9: PL images of (a) the adapted ARC reference HJT solar cell without TiO$_2$ nanodisks and (b) the HJT solar cell with the nanodisk array, respectively. In the image (b), the structured area is indicated with a white rectangle. The color bars correspond to the counts representing luminescence intensity. The measurement integration time for both samples was 5 s.

We can also compare the performance of the HJT solar cell stack coated with the TiO$_2$ nanodisks to the stack coated by a double ARC. The coating we consider consists of a MgF$_2$ layer on top of the ITO layer (with optimized thicknesses of 95 nm and 60 nm, respectively). Simulated reflectance of the HJT solar cell with double ARC is shown in Appendix B. We note that we compare only the current density losses that were calculated from the simulated reflectances since we did not fabricate a HJT solar cell with a double ARC. The calculated current density loss of the HJT solar cell with a double ARC is $2.7 \text{ mA} \cdot \text{cm}^{-2}$, which is slightly lower than the current density loss calculated for the HJT solar cell with the nanodisks. This mismatch most likely stems from the fact that the TiO$_2$ that was used for the fabrication did not have the refractive index as high as the

Rutile TiO_2, which was assumed for the initial design discussed in Sec. 3.2. However, the effect of encapsulation of the solar cell in a solar module will annihilate the advantage of the double ARC, while this is not the case for an optimized nanodisk structure, which will be shown in chapter 4.

Additionally, we studied the influence of the e-beam structuring on the passivation and electrical properties of the sample by taking the PL images of the reference flat sample and the sample with the nanodisk array, respectively. Both samples were laser cut from the same HJT solar cell precursor. The images were taken after the sample structured with the TiO_2 nanodisks was cured in the furnace at 200°C in order to mitigate the damage which was likely introduced during the exposure to e-beam. The resulting images are shown in Fig. 3.9. We observed that after curing the sample with the nanodisk array, the luminescence intensity of the samples with TiO_2 nanodisks was comparable to the intensity of the adapted ARC reference. This result shows that despite exposing the sample to e-beam, which can generally lead to the generation of nonradiative recombination centers, the passivation of the solar cell was kept intact since the luminescence intensity is proportional to the lifetime of the minority carriers in the device.

3.4 Conclusions

In this chapter, we demonstrated that a sufficiently high degree of discrete rotational symmetry together with helicity preservation are the relevant requirements for the design of nanostructure arrays aimed to improve the AR properties of solar cells. For the systems with nanodisks in a periodic arrangement whose discrete rotational symmetry is $C_{n \geq 3}$, our numerical results link the ability of the system to preserve helicity (handedness) of the incident illumination to the suppression of backscattered field. For the selected design comprising TiO_2 nanodisk square array placed on the front surface of a flat HJT solar cell stack, we achieved a significant decrease of the current density loss due to reflection. We also have demonstrated that increasing the rotational symmetry when switching from the square (C_4) to hexagonal (C_6) lattice can further improve the AR performance of the nanodisk coating.

Moreover, we fabricated and subsequently characterized an optimized TiO_2 nanodisk array on top of a flat HJT solar cell by e-beam lithography. We demonstrated that placing such nanodisks on a solar cell layer stack leads to a significant reduction of reflectance over a broad spectral range. Additionally, placing the nanodisks on top of the HJT solar cell layer stack in an electrically decoupled manner can ensure that the passivation of the solar cell stays intact. The passivation preservation was evaluated through PL images of the areas with and without TiO_2 nanodisk array, whose luminescence intensities were comparable.

4. Energy Yield of Solar Modules with Periodically Arranged Nanostructures

This chapter discusses the annual energy (EY) of mono- and bifacial solar modules based on c-Si HJT solar cells with relatively thin wafers for which the employment of the photonic nanostructures is of interest. After an introductory Sec. 4.1, we will introduce investigated solar module architectures and employed computational methods in Sec. 4.2. In Sec. 4.3, we will discuss the optical properties of solar modules into which the nanodisk arrays used as AR and light trapping (LT) structures are introduced and compare them to the reference module architectures. Next, in Sec. 4.4, we will present the results of the annual EY calculations and elucidate how the improved optical properties of the solar modules with the nanodisks increase the output power. The content of this chapter is based on [P2]. This project was carried out in collaboration with the research group of Tenure-Track-Prof. Dr. Ulrich W. Paetzold from IMT/LTI at KIT.

4.1 Introduction

Although various nanophotonic structures were proposed and studied in the past, it is important to analyze their performance on the level of the solar module and under realistic irradiation conditions. Such performance analysis was performed for various solar module architectures with textured interfaces and/or flat ARCs employed for optimizing the optical properties [107–112]. In a realistic scenario, the solar module is not always illuminated with normally incident light, and the consideration of a particular nanostructure design based on its ability to increase the short-circuit current density under standard test conditions is not sufficient. One has to additionally ensure that the optical performance of the proposed AR and/or LT nanostructures is robust when the incoming irradiation impinges on the solar module at an elevated incident angle. Moreover, the absorption of the photons in the active layer of the solar module depends on other factors such as the sun's position and the cloud coverage effect on the incoming irradiation. For solar cells with photonic nanoscatterers placed on both front and rear surfaces, it is also interesting to assess the power output in the bifacial solar module configuration. Such solar module architecture allows to harvest those photons that can be absorbed in the active material when the light either impinges on the module from its back or is reflected from the ground.

In this chapter, we will discuss the EY of relatively thin wafer-based c-Si HJT solar modules, for which nanodisk gratings cover both the front and rear surface of the solar cell stack. We consider square arrays of dielectric high-index TiO_2 nanodisks as the AR and LT photonic nanostructures. The geometrical parameters of these arrays were optimized, and the resulting annual EY for mono- and bifacial modules with the nanocoated solar cells were compared to the standard flat references relying on the flat ARCs. Additionally, we compared the power output of the solar modules with AR and LT nanodisks to the performance of the state-of-the-art solar modules with textured c-Si wafers. The nanodisk arrays were optimized concerning the short-circuit current density associated with the reflected portion of the light for normally incident light. The

optimal geometrical parameters depend on whether the nanodisks were placed on the front solar cell-encapsulation interface, where they suppress backscattering and improve the light in-coupling, or on the rear solar cell-encapsulation interface, where they improve the LT properties. To obtain the primary information that is transferred into the EY modeling framework, we calculated the optical response of the solar cell-encapsulation interfaces while considering AR and LT nanodisk arrays for multiple incidence angles using full-wave simulations. The annual EY was assessed for the mono- and bifacial module architectures with and without TiO_2 AR and LT nanodisk arrays at locations on earth with different climate conditions. We also considered the influence of albedo radiation, which is particularly interesting for bifacial solar modules [113]. Here, we aim to demonstrate that upon reducing the c-Si wafer thickness down to a value where chemical texturing becomes challenging, if not impossible, the proposed AR and LT nanodisks are an excellent alternative to state-of-the-art pyramidal textures and approach their performance.

4.2 Solar module architectures and computational methods

4.2.1 Investigated module architectures and electrical properties

We considered six different solar module architectures in our analysis, which are shown in Fig. 4.1. The extensive numerical simulations of the annual EY were performed for the module architectures (a) to (d). They correspond to mono- and bifacial solar modules with either standard flat ARC [architectures (a) and (c)] or AR and LT nanodisks at solar cell-encapsulation interfaces [architectures (b) and (d)]. We additionally compared the performance of the solar modules with nanodisks to the performance of the state-of-the-art architectures employing solar cells with chemically textured c-Si wafers [architectures (e) and (f)]. For the architectures (a) to (d), we varied the thickness of the c-Si absorber between 5 μm to 80 μm with 1 μm steps and studied the annual EY. The chosen thickness range falls between thin photovoltaics (PV) with absorber thicknesses of a few micrometers and conventional wafer-based c-Si PV. In the case of state-of-the-art architectures (e) and (f), the annual EY was calculated only for a few select thicknesses of the c-Si wafer. Such variation of the thickness allows judging from which thickness on the suggested concept using the nanodisks is beneficial compared to the more traditional approaches considered for comparison.

For all considered architectures, the front a-Si:H layer (passivation intrinsic and n^+-doped) of the c-Si HJT solar cell had a thickness of 8 nm, the same as for a structure considered in the simulations in the previous chapter. The thickness of the front conducting ITO layer depended on the architecture. For all reference module architectures relying either on the flat ARC or the combination of flat ARC and random pyramidal texture [(a),(c), (e), and (f)], the thickness of this layer was 75 nm. This thickness was found to be optimal for reference architectures when we considered a solar cell-encapsulation interface. In the case of the modules with AR and LT nanodisks [architectures (b) and (d)], the thickness of the front ITO layer was reduced to 10 nm. This reduction stems from the optimization of the AR nanodisk array and is the minimal thickness that can allow decent conductivity of a solar cell. The rear a-Si:H layer (passivation intrinsic and p^+-doped) of all architectures was slightly thicker than that on the front, while the rear ITO contact layer was thinner than its counterpart on the front surface of the solar cell. For architectures (b) and (d) which contained AR and LT TiO_2 nanodisk square arrays, the dimensions of an individual nanodisk and the lattice constant were determined through an optimization process which will be discussed in more detail in Sec 4.2.2. The optimal geometrical parameters for the AR nanodisk array were determined to be as follows: 125 nm radius and 90 nm height of an individual nanodisk with 320 nm lattice constant. The optimal
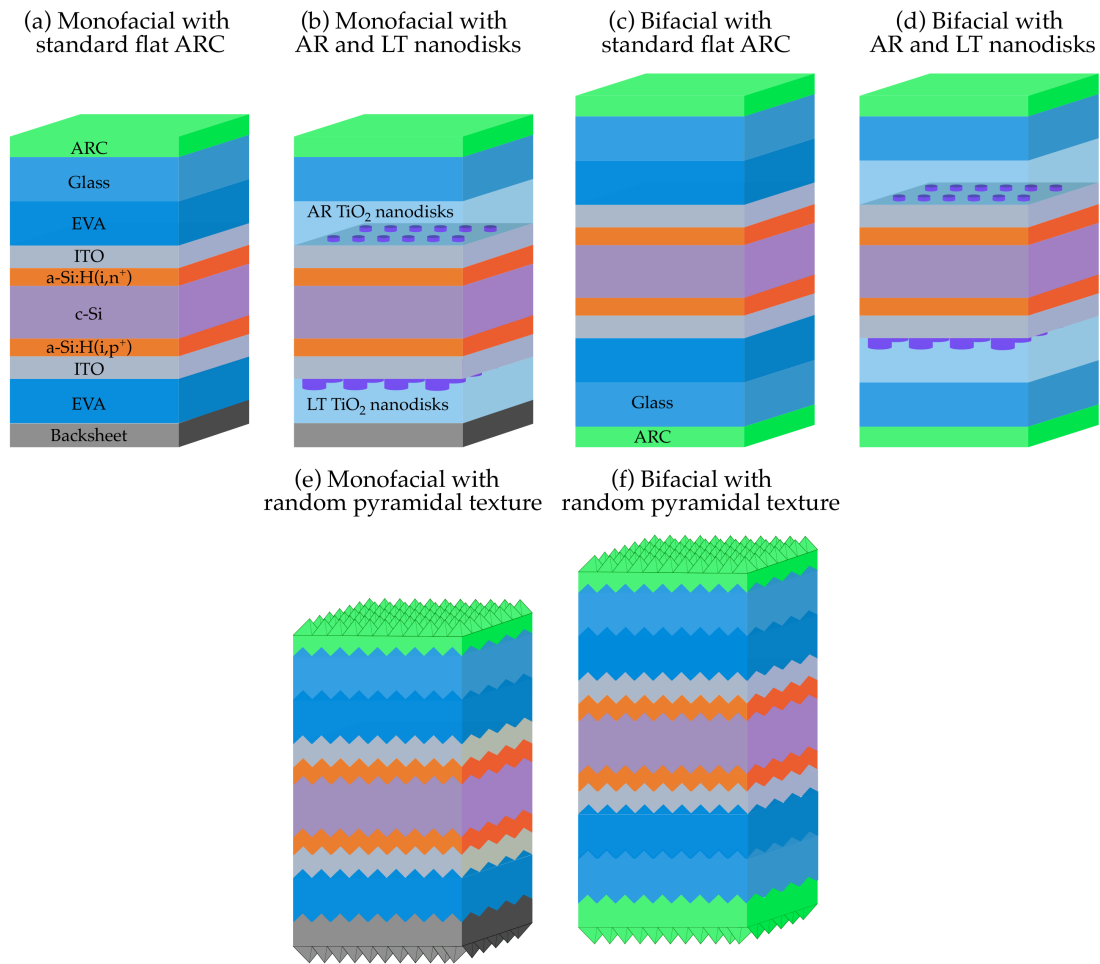
FIGURE 4.1: Schematic image of the six solar module architectures discussed throughout this chapter: (a) Monofacial reference module with an optimized transparent conductive ITO layer on the front of the solar cell, which serves as both ARC and front contact. A silver mirror mimicking the optical behavior of the perfectly reflective backsheet is placed at the rear side of the module. The Front ITO layer is preceded by window glass and encapsulation ethylene-vinyl acetate (EVA) layers. These window layers are covered with an ARC (MgF$_2$). The EVA layer, the same as the one on the front of the architecture, is beneath the rear ITO layer. For all investigated solar module architectures, the window layers are the same. (b) Monofacial module with the optimized AR and LT nanodisk arrays placed on top of the front and rear ITO contacting layers, respectively. The backsheet follows the rear EVA layer as in the previous architecture. (c) Bifacial reference module with a standard flat ARC of the solar cell as in architecture (a) with symmetric window layers on either side of the solar module. (d) Bifacial module with the optimized AR and LT nanodisk arrays on top of the front and rear ITO contacting layers with symmetric window layers on either side of the solar module, respectively. (e) State-of-the-art monofacial module architecture with a solar cell with a textured c-Si wafer. (f) State-of-the-art bifacial module architecture with a solar cell with a textured c-Si wafer. Adapted with permission from [P2]. © 2021 Optical Society of America.

geometrical parameters of the LT nanodisk array were: 215 nm radius and 395 nm height of an individual nanodisk with 565 nm lattice constant.

We considered the bifacial HJT solar cells for all investigated solar module architectures. In our simulations, we neglected the effect of the metallic contacts on the optical performance and, subsequently, the annual EY of the modules. To imitate the optical performance of the perfectly reflective backsheet of the monofacial solar module, we introduced a 200 nm thick silver layer on the rear side of the respective module architectures. The window layers of the monofacial solar modules were non-absorbing glass and encapsulation ethylene-vinyl acetate (EVA) layer with thicknesses of 4 mm and 400 μm, respectively. These window layers were covered by a 130 nm ARC film made of magnesium fluoride (MgF$_2$). The bifacial architectures had the window layers covered by ARC on either side, which were identical to those on the front sides of the monofacial solar modules. In the bifacial solar module configuration, there is a possibility to absorb the light incident on either side of the solar module.

On top of that, one can take advantage of albedo radiation since the portion of light that is initially transmitted by the solar module and is reflected from the ground surface towards the module has a second chance for absorption in c-Si, considerably boosting the annual EY. When a bifacial solar module is tilted, albedo radiation can influence the performance of the solar module also in another way. To be specific, the light reflected from the ground surface can also directly hit the front surface of the tilted module and can subsequently be absorbed. The impact of albedo radiation on the annual EY of the solar module is also relevant for tilted monofacial solar modules. These aspects have to be carefully considered.

Refractive index data for c-Si, TiO$_2$, ITO, and Ag considered in the simulations were taken from literature [72, 104, 105, 114]. Material data for the front and rear composite (passivation intrinsic and doped) a-Si:H layers were provided by Meyer Burger Research AG, and the corresponding graphs can be found in Appendix A. An optically thick non-absorbing glass layer was considered to have a nondispersive refractive index of $n = 1.5$. Since the glass layer was non-absorbing, its thickness did not impact the performance of the investigated solar modules. The refractive index data of the encapsulating EVA layer and the MgF$_2$ thin ARC were taken from [115] and [116], respectively.

To calculate the annual EY of various solar modules, one has to specify the electrical parameters. The parameters used in our simulations, corresponding to a typical c-Si HJT solar cell, are summarized in Table 4.1. The shadowing by electrical connections for all investigated solar module architectures was disregarded.

TABLE 4.1: Electrical parameters of the solar cell. Reprinted with permission from [P2]. © 2021 Optical Society of America.

Shunt resistance, R_{sh} [$\Omega \cdot cm^2$]	5000
Series resistance, R_s [$\Omega \cdot cm^2$]	0.7
Reverse-blocking current, J_0 [A/cm^2]	$2 \cdot 10^{-13}$
Ideality factor, n_{id}	1.1
Temperature coefficient of J_{SC}, $t_{J_{SC}}$ [%/K]	0.05
Temperature coefficient of V_{OC}, $t_{V_{OC}}$ [%/K]	-0.25

A HJT solar cell with such a set of electrical parameters would have a J_{SC} around 38.3 mA/cm^2. We note that such a value of the short-circuit current density corresponds to a state-of-the-art c-Si HJT solar cell with a thick and textured wafer. Such a device will have $V_{OC} = 0.734$ V at a temperature of $T = 25°C$ based on the following equation:

$$V_{OC} = n_{id} V_{th} \ln \left(\frac{J_{SC}}{J_0} + 1 \right),$$ (4.1)
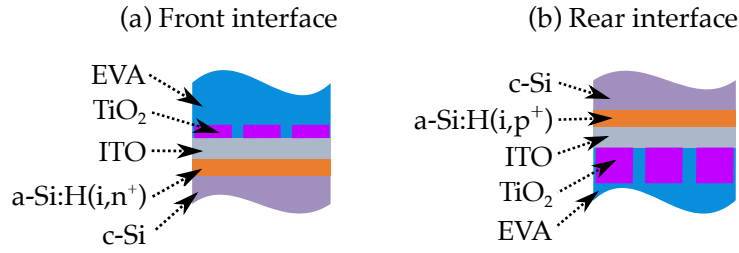
FIGURE 4.2: Schematic image of solar cell-EVA interfaces as considered in the optical simulations. (a) Front solar cell-EVA interface. The ITO layer is covered with an AR TiO$_2$ nanodisk array. (b) Rear solar cell-EVA interface. The ITO layer is covered with a LT TiO$_2$ nanodisk array. Adapted with permission from [P2]. © 2021 Optical Society of America.

where the thermal voltage reads as $V_{\text{th}} = kT/q = 0.0257$ V, with k being the Boltzmann constant. The values of the ideality factor and reverse-blocking current are taken from Table 4.1.

The optical simulations of the EVA-cell interface for both AR and LT TiO$_2$ nanodisk arrays were performed employing FEM. The annual EY was calculated using the EY modeling framework briefly introduced in Sec. 2.3.2.

4.2.2 Calculation of reflectance, transmittance, and absorptance

We calculated reflectance and transmittance into multiple scattering directions for each considered incidence direction, characterized by a polar and azimuth angle, and wavelength for the solar cell-EVA interfaces with AR and LT nanodisk arrays on top of the respective ITO layers. Reflectance and transmittance are given as the ratio of the scattered reflected or transmitted power to the power of the incident field. The respective interfaces are schematically shown in Fig. 4.2.

For both investigated interfaces, c-Si and encapsulating EVA were assumed to be non-absorbing and semi-infinite. Usually, when semi-infinite substrate and superstrate are assumed, one has to consider the impact of the glass-EVA and air-glass interfaces on the optical performance of the system with nanodisk array [117]. In our case, however, the c-Si wafer thicknesses are in the range between thin PV and conventional c-Si PV, and the influence of the interfaces mentioned above is considerably reduced. Additionally, the matrix formalism employed in the EY modeling framework allows to account for the light-matter interaction at the glass-EVA and air-glass interfaces and combines the simulation results for these optically thick layers with the optical response of the solar cell-EVA interfaces with nanodisk arrays, thus forming a matrix that describes the optical response of the entire system. Therefore, those contributions can be neglected at that level of the optical simulations.

For a certain azimuth angle ϕ_{in}, reflectance and transmittance values form matrices with a size of $(N_{\theta_{\text{in}}}, N_{\theta_{\text{r,t}}}, N_\lambda)$, where the entries corresponded to the polar angles of incidence, scattering angles, and wavelengths, respectively. The polar angle θ_{in} was varied from 0° to 89° with 5° steps. The results were then interpolated down to a resolution of 1°. For the azimuth angle ϕ_{in}, the rotational symmetry of the nanodisk array (C_4) is exploited, and only calculations for angles between 0° and 45° with 15° steps were performed. The calculated matrices for different ϕ_{in} values were subsequently averaged. Total reflectance and transmittance for a certain wavelength and incident polar and azimuth angles were

calculated using the following equations:

$$R = \frac{\sum\limits_{\boldsymbol{k}_{\mathrm{r}}} |\tilde{\boldsymbol{E}}(k_{\mathrm{r,x}}, k_{\mathrm{r,y}})|^2 \cdot \cos(\theta_{\mathrm{r}})}{|\boldsymbol{E}_0|^2 \cos(\theta_{\mathrm{in}})}, \tag{4.2}$$

$$T = \frac{\sum\limits_{\boldsymbol{k}_{\mathrm{t}}} n_{\mathrm{out}} |\tilde{\boldsymbol{E}}(k_{\mathrm{t,x}}, k_{\mathrm{t,y}})|^2 \cdot \cos(\theta_{\mathrm{t}})}{n_{\mathrm{in}} |\boldsymbol{E}_0|^2 \cos(\theta_{\mathrm{in}})}, \tag{4.3}$$

where $\boldsymbol{k}_{\mathrm{r,t}}$ are the wave vectors of the reflected and transmitted fields, $\theta_{\mathrm{r,t}}$ with $\cos\theta = \Re(\pm k_{\mathrm{z}}/k_{\mathrm{r,t}})$ are the scattering angles, and n_{in} and n_{out} are the refractive indices of the media in which the incident and scattered field propagate, respectively. The incident illumination $\boldsymbol{E}_0$ was the superposition of TE- and TM-polarized light. To calculate reflectance and transmittance, we employed the angular spectrum representation, and $\tilde{\boldsymbol{E}}(k_{\{\mathrm{r,t}\},\mathrm{x}}, k_{\{\mathrm{r,t}\},\mathrm{y}})$ in Eqs. 4.2 and 4.3 were calculated via the Fourier transform of the electric fields in real space obtained through full-wave simulations.

Absorptance values for a given azimuth angle formed a matrix with a size of (N_m, $N_{\theta_{\mathrm{in}}}$, N_λ), where index m runs over all absorbing layers (a-Si:H(i,n^+/p^+), ITO, TiO$_2$) contained in either the front or rear solar cell interface. The simulations for varying angles of incidence were performed for the systems with the optimized AR and LT nanodisk arrays. The optimization of the optical response of the solar cell-EVA interface with the nanodisks was performed concerning the short-circuit current density corresponding to reflectance in the case of a normally incident light, which was calculated as

$$J_{\mathrm{SC,R}} = q \int_{\lambda_1}^{\lambda_2} \phi_{\mathrm{AM1.5}}(\lambda) R(\lambda) d\lambda, \tag{4.4}$$

where and $\phi_{\mathrm{AM1.5}}(\lambda)$ is the spectral photon flux. The spectral AM1.5G spectrum data was taken from [66], and the total reflectance $R(\lambda)$ was interpolated accordingly. As it was done in the previous chapter, we assumed the perfect charge carrier collection efficiency with IQE(λ)=1 when calculating $J_{\mathrm{SC,R}}$. The short-circuit current density associated with reflectance was minimized in the case of the front AR nanodisk array and maximized in the case of the rear LT nanodisk array, respectively. The optimization process was carried out by varying one of the geometrical parameters of the nanodisk array (disk radius, disk height, and lattice constant) while the remaining parameters were kept fixed. We cycled through and sequentially optimized these geometrical parameters until we achieved either the global minimum or maximum value of $J_{\mathrm{SC,R}}$ for the front solar cell-EVA interface or rear solar cell-EVA interface, respectively. In the first stage of the optimization process, the geometrical parameters of the AR and LT nanodisk arrays were varied as coarsely as in the previous chapter. To verify that either a global minimum or maximum was achieved, the steps for all geometrical parameters were reduced to 5 nm. As was described in Sec. 2.3.2, the light propagation multi-layer thin-film stacks was treated coherently using TMM, while in the case of the thicker layers (c-Si, window glass, and EVA layers), the Beer-Lambert law (Eq. 2.60) was employed to calculate absorptance. When the AR and LT nanodisk arrays were considered in place of the thin-film layers, the optical response of the investigated solar module architecture as a whole was computed by integrating the corresponding reflectance, transmittance, and absorptance matrices obtained using FEM into the Optics Module of the EY modeling framework.

4.3 Optical performance of solar module architectures

4.3.1 Reflectance of front and rear solar cell-encapsulation interfaces

Before comparing the annual EY of various solar module architectures, we will discuss in detail the optical properties of the reference solar modules with flat ARC and modules with integrated AR and LT nanodisk arrays. In particular, we will closely look at reflectance of the solar cell-EVA interface. Figure 4.3 shows reflectance in the case of normally incident light of the solar cell-EVA interfaces with either AR or LT nanodisk array. The interfaces are illuminated either from EVA semi-infinite half-space or from c-Si semi-infinite half-space. The reflectances at the flat reference solar cell-EVA interfaces were computed using TMM and are plotted for comparison.
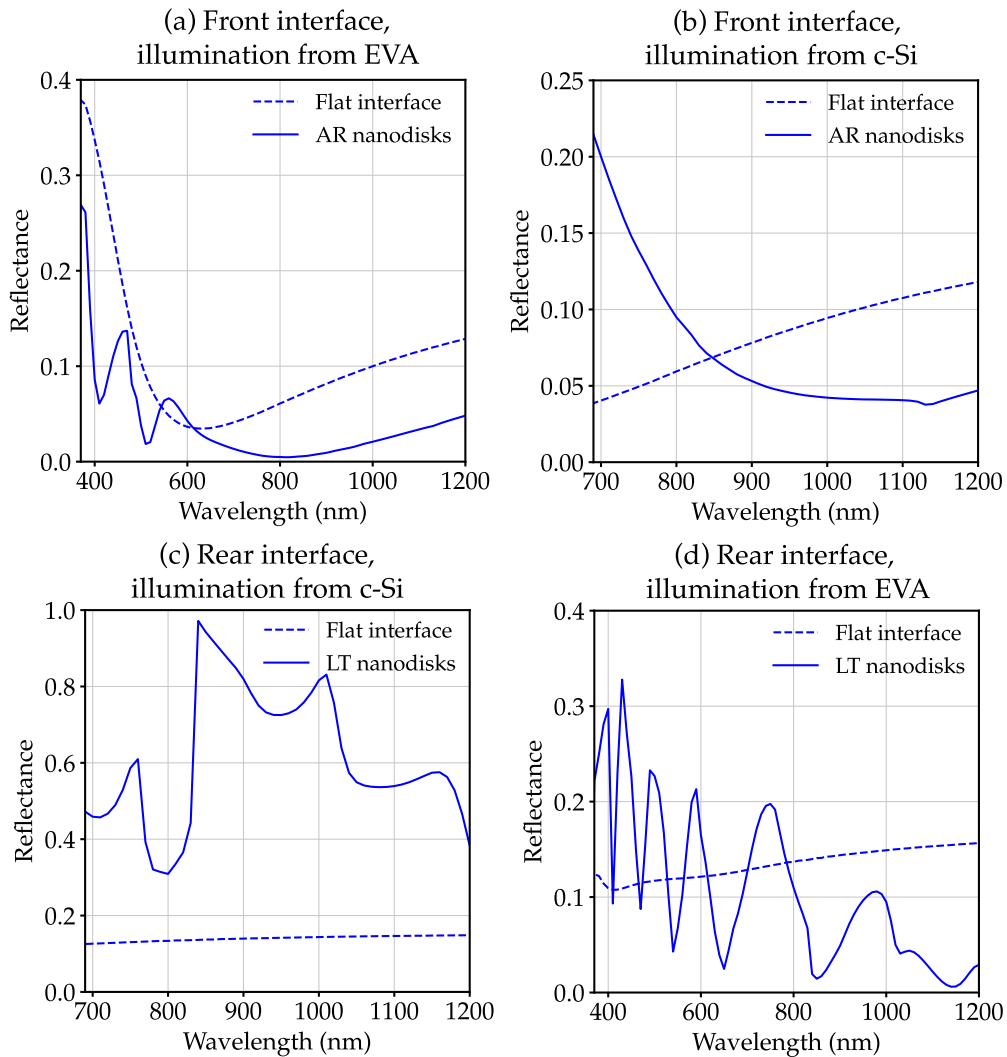
FIGURE 4.3: Reflectance at normal incidence of the solar cell-EVA interfaces with either AR [Fig. 4.2(a)] or LT [Fig. 4.2(b)] nanodisk array. Interfaces are the same for the pairs of graphs (a)-(b) and (c)-(d), respectively. The illumination is either from EVA or c-Si semi-infinite half-spaces. Adapted with permission from [P2]. © 2021 Optical Society of America.

The graphs (a) and (b) in Fig. 4.2 characterize the optical performance of the front solar cell-EVA interface with the AR nanodisk array, which is schematically depicted in Fig. 4.2(a). Here, the objective was to minimize the short-circuit current density $J_{SC,R}$ associated with reflectance (Eq. 4.4). Reflectance of the interface with such an optimized

AR nanodisk array when the light is impinging from the EVA semi-infinite half-space is shown in Fig. 4.3(a). The design of this AR coating was inspired by the optimization results discussed in the previous chapter and published in [P1]. The optimal parameters obtained in the case of the solar cell-air interface were a starting point for the optimization in the case of the solar cell-EVA interface, and the design of the system with AR nanodisk coating is related to the ability of this system to avoid cross-talk between the opposite helicities of the electromagnetic field.

The resulting reflectance of the interface with the AR nanodisk array is lower than the one at the interface with the flat ARC. It exceeds the reflectance of the reference flat interface only in the spectral region in the vicinity of $\lambda = 600$ nm, for which the standard ARC of a c-Si HJT solar cell is usually optimized. Nevertheless, as can be seen from Fig. 4.3(b), the LT properties of this nanodisk array are considerably worse than its AR properties. When the light is incident on the front solar cell-EVA interface from c-Si semi-infinite half-space, only the long wavelength response is of interest since the short-wavelength photons are absorbed before reaching the rear of the c-Si solar cell. The system with AR nanodisk coating transmits the light reflected from the rear of the stack quite strongly at long wavelengths, and it does not have LT properties superior to the ones of the system with the standard flat ARC. Such optical response shows that the nanodisk array placed on the front solar cell-EVA interface contributes to the improved light harvesting of a solar module mainly due to its superior AR properties.

The graphs (c) and (d) in Fig. 4.3 correspond to the optical performance of the rear solar cell-EVA interface with the introduced LT nanodisk array, which is schematically depicted in Fig. 4.2(b). In this case, the optimal parameters of the nanodisk array strongly diverge from the ones of the AR nanodisk array. The individual nanodisks are significantly larger than their counterparts at the front solar cell-EVA interface and are sparsely spaced. Given the absorption depth of c-Si introduced in Fig. 2.8 in Sec. 2.2.5, for the minimal considered absorber thickness of 5 μm, the photons that can reach the rear side of the c-Si solar cell have wavelengths $\lambda \geq 690$ nm. The incident light is effectively scattered into multiple directions for such nanodisk array, thus allowing for improved harvesting of the long wavelength photons reaching the rear of the c-Si solar cell.

Reflectance of the interface with the optimized LT nanodisk array is shown in Fig. 4.3(c). The LT properties of the system with LT nanodisk are considerably superior to the LT properties of the system with standard flat ARC throughout the whole spectral region. However, results shown in Fig. 4.3(d) indicate that even though the system with LT nanodisks outperforms the flat reference in terms of the AR properties in the long wavelength region, its main contribution to the improved absorptance in the c-Si wafer is related to its strong LT properties. Thus, when the nanodisk arrays with decoupled AR and LT properties are introduced on the front and rear solar cell-EVA interfaces, respectively, one can significantly boost absorptance in c-Si, and, consequently, the annual EY of the solar module.

4.3.2 Analysis of parasitic absorption losses in solar modules

One important aspect of the optical performance of a given solar module architecture is parasitic absorption. We analyzed the absorptance in different layers of the solar modules for a c-Si wafer intermediate thickness of 40 μm for normally incident light. Absorptance in all layers of mono- and bifacial solar modules except for glass which was assumed to be non-absorbing, is shown in Fig. 4.4 and Fig. 4.5, respectively.

We note that absorptance is not indicated in the graphs for some layers if it was found to be negligible. For example, it was the case for the rear a-Si:H(i,p^+) layer for the monofacial solar module and the rear and front a-Si:H($i,p^+/n^+$) layers for the bifacial solar module
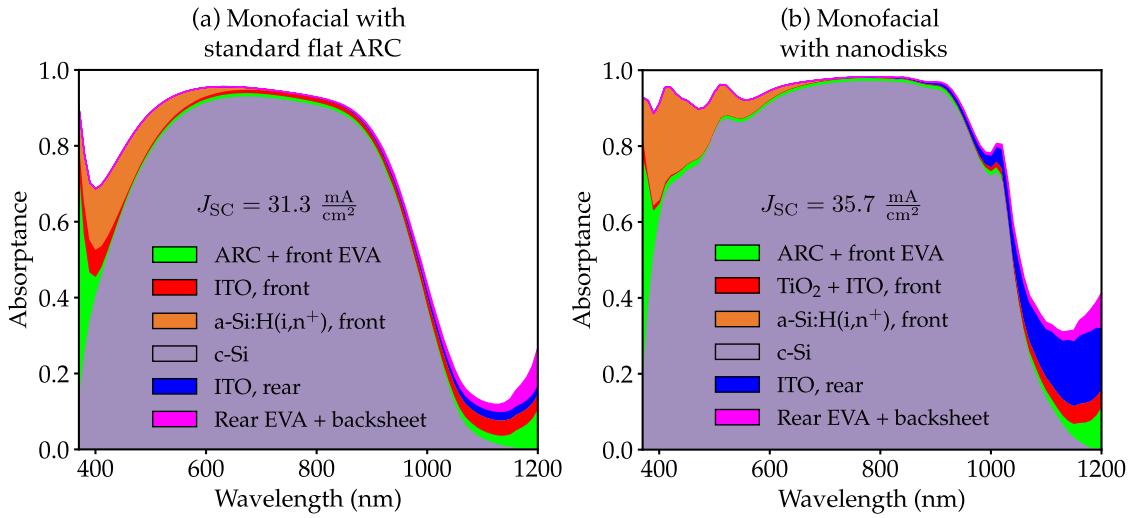
FIGURE 4.4: Absorptance in the layers of (a) the monofacial reference solar module with a standard flat ARC and (b) the monofacial solar module with the AR and LT nanodisk arrays placed on the front and rear ITO layers for normally incident ligth. For both solar module architectures, the c-Si wafer thickness was 40 μm. Adapted with permission from [P2]. © 2021 Optical Society of America.

for the forward and backward illumination direction, respectively. Additionally, the LT nanodisk array did not introduce any parasitic absorption in the case of the monofacial solar module and the bifacial solar module when it was illuminated from its front since TiO_2 absorbs only at wavelengths shorter than 380 nm, and these short wavelength photons are absorbed before reaching the rear side of the c-Si cell. Analogously, the AR nanodisk array in the case of the bifacial solar module did not introduce any parasitic absorption when it was illuminated from its rear side.

To qualitatively compare the performance of the solar modules with nanodisks and the reference modules, we calculated the short-circuit current density using the following equation:

$$J_{SC} = q \int_{\lambda_1}^{\lambda_2} \phi_{AM1.5}(\lambda) A(\lambda) d\lambda, \tag{4.5}$$

where $A(\lambda)$ is absorptance in the c-Si wafer. Here, we assumed a perfect collection efficiency. The calculated values of J_{SC} are indicated on top of all graphs in Fig. 4.4 and Fig. 4.5. As it was for Eq. 4.4, we used the AM1.5G spectrum for the calculation.

The front conducting ITO layer in the case of the reference solar module with a standard flat ARC [Fig. 4.4(a)] serves as an ARC but introduces some parasitic absorption. When we introduce the AR nanodisk array [Fig. 4.4(b)], the thickness of the ITO layer is significantly reduced from 75 nm to 10 nm. This way, the parasitic absorption in this layer becomes smaller, especially in the short wavelength range. The AR nanodisks have a very small contribution to the parasitic absorption since the major portion of the photons which could reach and be absorbed in the nanodisks is absorbed in the thick EVA layer (wavelengths between 300 nm and 360 nm). Nevertheless, while increasing absorptance in c-Si due to improved light in-coupling, the introduction of the AR nanodisk array leads to the increase of the parasitic absorption in the front a-Si:H(i,n^+) layer. We note, however, that in [118] it was shown that the carriers absorbed in the front passivating a-Si:H(i) layer can still contribute to the short-circuit current. Thus, the parasitic absorption in the front composite a-Si:H(i,n^+) layer is the upper bound for the parasitic loss and can be less significant in reality. The LT nanodisk array helps to further improve the optical
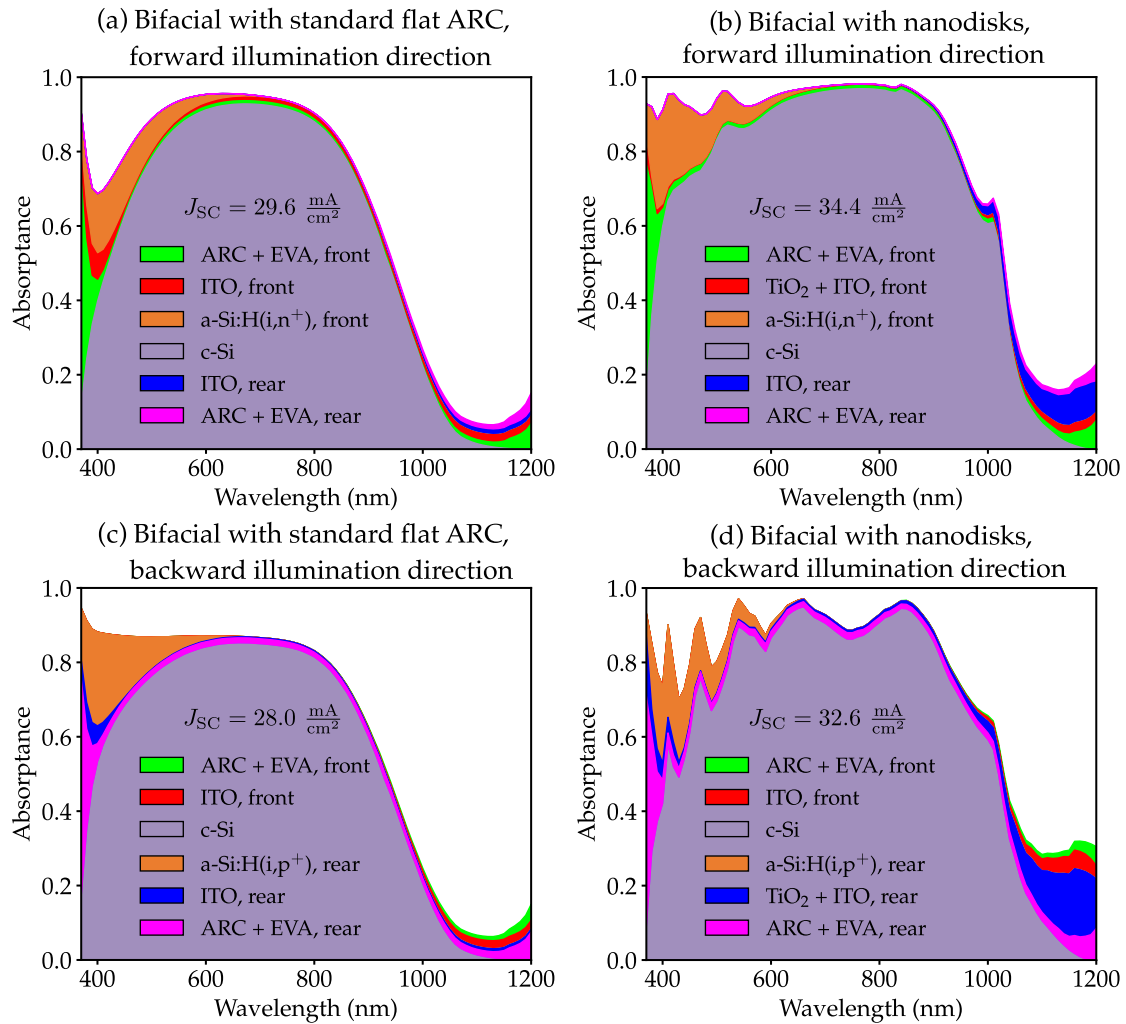
(a) Bifacial with standard flat ARC,
forward illumination direction

(b) Bifacial with nanodisks,
forward illumination direction

(c) Bifacial with standard flat ARC,
backward illumination direction

(d) Bifacial with nanodisks,
backward illumination direction

FIGURE 4.5: Absorptance in the layers of the bifacial solar modules for a normally incident light: (a) in the case of forward illumination direction for the bifacial reference solar module with the standard flat ARC, (b) in the case of forward illumination direction for the bifacial solar module with AR and LT nanodisk arrays introduced on top of the front and rear ITO layers, respectively, (c) in the case of backward illumination direction for the bifacial reference solar module with the standard flat ARC, (d) in the case of backward illumination direction for the bifacial solar module with AR and LT arrays introduced on top of the front and rear ITO layers, respectively. For both solar module architectures, the c-Si wafer thickness was 40 μm. Adapted with permission from [P2]. © 2021 Optical Society of America.

performance of the monofacial solar module by increasing absorptance in c-Si in the long wavelength range. At the same time, the strong scattering effect of the LT nanodisks also leads to increased parasitic absorption in this spectral region.

From comparing the short-circuit current densities of the monofacial solar module architectures, which are indicated in both graphs in Fig. 4.4, we can see that the addition of AR and LT nanodisk arrays on top of the front and rear ITO layers leads to 14.1 %$_{rel}$ increase of J_{SC}. However, we should also compare the short-circuit current density, which can be reached for the module with the nanodisks, to one of the state-of-the-art architecture ((e) in Fig. 4.1). For the same wafer thickness of 40 μm, the latter will yield $J_{SC} = 36.1$ mA/cm^2, which gives the difference of 1.1 %$_{rel}$. Thus, also performing slightly

worse than the random pyramidal texture, the AT and LT nanodisks arrays allow for a broadband enhancement of absorptance in the c-Si wafer and can serve as a decent substitute for the pyramids when the standard texturing procedure becomes impractical.

If we consider the bifacial standard reference module when it is illuminated from its front [Fig. 4.5(a)], the parasitic absorption for the wavelengths below $\lambda = 700$ nm resembles that of the monofacial standard reference module. As expected, the parasitic absorption is a little lower in the long wavelength range since more light is transmitted through the rear window layers. If the AR and LT nanodisk arrays are introduced on top of the front and rear ITO layers [Fig. 4.5(b)], absorptance in c-Si is analogous to the monofacial solar module case. Let us consider the scenario when the bifacial solar module is illuminated from the rear [Fig. 4.5(d)]. In this case, the AR and LT nanodisks also visibly improve absorptance in the c-Si wafer when compared to the reference bifacial solar module with the standard flat ARC [Fig. 4.5(c)], even though the LT nanodisks do not possess optimal AR properties and introduce dips in c-Si absorptance since there are sharp spectral features in reflectance spectrum [Fig. 4.3(d)].

Let us now compare the short-circuit current densities of the bifacial solar module architectures for both forward and backward illumination direction indicated in the graphs in Fig. 4.5. Upon the forward illumination, introducing the AR and LT nanodisk arrays on top of the front and rear ITO layers leads to $16.2\,\%_{rel}$ increase of J_{SC}. In the case of the backward illumination, the improvement of J_{SC} is $16.4\,\%_{rel}$. Now we will compare the performance of the bifacial solar module with the nanodisks with the state-of-the-art bifacial solar module [Fig. 4.1(f)]. For the bifacial solar module with the random pyramidal texture and c-Si wafer thickness of 40 μm, the short-circuit current densities were found to be 34.7 and 34.6 mA/cm^2 for the forward and backward illumination direction, respectively. Analogously to the monofacial solar module, the bifacial solar module with the texture outperforms the bifacial solar module with the AR and LT nanodisk arrays with the difference in J_{SC} being $0.9\,\%_{rel}$ and $6.1\,\%_{rel}$ for the forward and backward illumination direction.

4.4 Energy yield of solar modules

After discussing in detail the optical performance of the solar modules with the nanodisks introduced at the front and rear solar cell-EVA interfaces, we will now focus on the annual EY of the solar module configurations from Fig. 4.1 for three cities in the United States of America located in different climate zones [119]. Two of the chosen cites have contrasting irradiation conditions – Anchorage, AK, and Honolulu, HI. Anchorage is located in a cold and cloudy region (Boreal climate), while Honolulu is located in a hot and sunny region (Tropical climate). The third chosen city, Kansas City, MO, has a temperate climate with and receives the annual solar irradiance, which lies in between the irradiances of the first two cities. Through considering the locations in different climate zones, we aimed to showcase the robustness of the performance of the solar modules with the AR and LT nanodisk arrays and their ability to boost the annual EY irrespective of the irradiation conditions, albeit with minor differences which most likely stem from the spectral features caused by the nanodisks. In our simulations, the solar modules were facing south, and the tilt angles were optimized for each of the three cities. The optimal tilt angles were found to be 38° for Anchorage, 30° for Kansas City, and 17° for Honolulu, respectively. The extensive analysis of the annual EY was done for the solar module architectures (a) to (d) from Fig. 4.1. The calculation of the annual EY for the state-of-the-art reference solar modules with the textured c-Si wafers was done only for Kansas City for a few select c-Si wafer thicknesses.

Figure 4.6 shows the relative increase of the annual EY when the AR and LT nanodisk
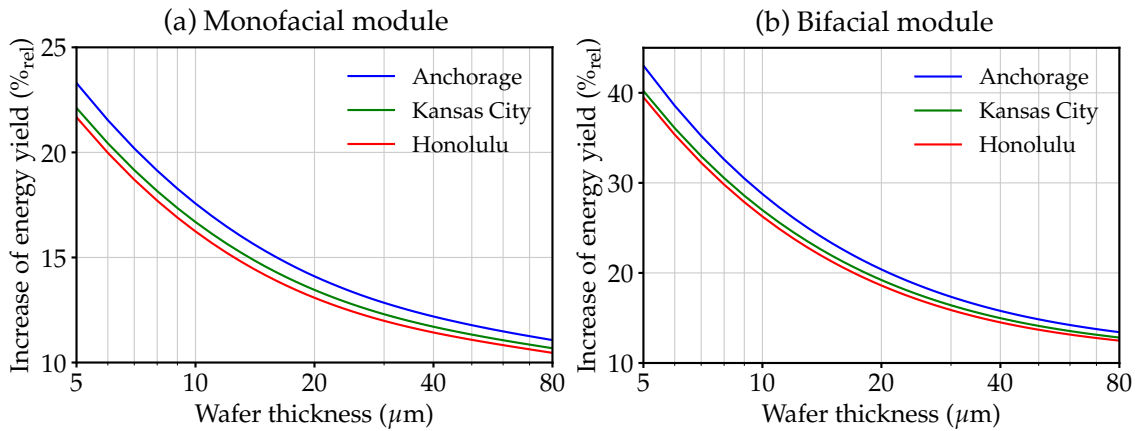
FIGURE 4.6: Relative increase of the annual EY for three locations in the United States of America in the case of (a) the monofacial solar module (comparing architecture (b) to (a) from Fig. 4.1) and (b) the bifacial solar module (comparing architecture (d) to (c) from Fig. 4.1) with varying thickness of the c-Si wafer. Adapted with permission from [P2]. © 2021 Optical Society of America.

arrays on top of the front and rear ITO layers are employed instead of the standard planar ARCs. The improvement of the annual EY is shown as a function of the c-Si wafer thickness. This calculation was performed without consideration of albedo, although the bifacial solar modules are always installed on the ground surface with some albedo in a realistic scenario. We chose to perform this simulation without albedo since its influence is more substantial for the sunnier locations. We aimed to avoid the subsequent imbalance in annual EY to highlight the robustness of the performance of the solar modules with the nanodisks for varying irradiation conditions. The resulting relative increase of the annual EY was found to be 23.3 %$_{rel}$ and 43.0 %$_{rel}$ in the case of the minimal c-Si wafer thickness of 5 μm for monofacial and bifacial solar modules with AR and LT nanodisk arrays, respectively.

As expected, the monofacial solar module with AR and LT nanodisks [Fig. 4.1(b)] outperforms the reference monofacial solar module with standard flat ARC [Fig. 4.1(a)]. The effect of the nanodisk arrays becomes even more apparent with decreasing c-Si wafer thickness. When we consider the monofacial solar module, the LT nanodisk array serves the purpose of enhancing the light path length within the c-Si wafer, which is achieved by the scattering of the light in multiple directions upon interaction with large and sparsely spaced nanodisks. In the case of the bifacial solar module, the perfectly reflective backsheet is replaced by the transparent window layers [Fig. 4.1(d)], and the LT nanodisks have to also perform as a decent ARC to facilitate the efficient light in-coupling when the solar module is illuminated from its rear. The results in Fig. 4.6(b) demonstrate that despite the average AR properties of the LT nanodisk array [Fig. 4.3(d)], in the bifacial module configuration, an even stronger increase of the annual EY than for the monofacial module configuration can be achieved when compared to the reference architecture with the standard flat ARC [Fig. 4.1(c)].

We will now compare the annual EY of the mono- and bifacial solar modules with AR and LT nanodisk arrays with the EY of the state-of-the-art solar modules with random pyramidal texture. The results of this comparison are given in Tab. 4.2 We calculated the annual EY of the latter for two c-Si wafer thicknesses from the range we swapped for the calculations presented in Fig. 4.6 – the median thickness of 40 μm and the thickness of 80 μm below which the texturing of the c-Si wafer becomes unfeasible. We also calculated the annual EY for the c-Si wafer thickness of 160 μm, which is typical for industrial

TABLE 4.2: Comparison of the annual EY in Kansas City, MO in the case of the monofacial and bifacial solar modules with AR and LT nanodisk arrays and the solar modules with the random pyramidal texture. Reprinted with permission from [P2]. © 2021 Optical Society of America.

Module architecture	Wafer thickness [μm]		
	40	80	160
	Energy yield [kWh·m^{-2}a^{-1}]		
Monofacial with nanodisks	337.7	348.7	358.1
Monofacial with random pyramidal texture	344.9	355.6	364.5
Bifacial with nanodisks	356.5	370.6	382.2
Bifacial with random pyramidal texture	366.6	380.6	392.0

c-Si-based solar cells. For the bifacial solar modules, we considered the sandstone ground surface. Since the short-circuit current densities of the solar modules with nanodisks are smaller than the short-circuit current densities of the state-of-the-art solar modules (Sec. 4.3.2), the latter outperform the modules with nanodisk arrays for all three c-Si wafer thicknesses. As expected, the smallest difference in the annual EY is for the thickest c-Si wafer. When we compare the module architectures (e) to (b) and (f) to (d) shown in Fig. 4.1 in the case of 160 μm c-Si wafer, the gap in the annual EY reduces to 1.8 %$_{\text{rel}}$ and 2.6 %$_{\text{rel}}$ for the monofacial and bifacial solar modules, respectively. Nevertheless, we stress that the standard industrial process of c-Si wafer texturing is challenging to apply for thinner wafers, such as those considered here. Thus, the proposed AR and LT nanodisk arrays can be used as an alternative to the pyramidal textures since their fabrication is feasible, and they allow approaching the optical performance achieved by wafer texturing.

Lastly, we performed the calculation of the annual EY, taking into account albedo radiation for the solar module architectures (a)-(d) in Fig. 4.1. The results of this analysis are given in Fig. 4.7. We performed the simulations for the solar modules with a median c-Si wafer thickness of 40 μm for the sandstone and grass ground surface and compared their annual EY to the EY of the modules when albedo was not considered. While the interfaces for the reference solar modules with standard ARC are flat (architectures (a) and (c) in Fig. 4.1), the monofacial reference module slightly outperforms the bifacial reference module since the backsheet of the former configuration reflects the light reaching this sheet back into the solar module. This way, some of this light is reabsorbed in the c-Si wafer, while for the bifacial reference module, many photons are lost due to transmittance when no LT structure is introduced on the rear interface of the solar cell. Such difference in the annual EY is more prominent with the smaller tilt of the solar module since less irradiation can hit the rear side of the bifacial module. However, as soon as we take into account albedo radiation, this performance gap is breached, and the bifacial reference module starts to outperform the monofacial reference module. This difference highlights the influence of albedo on the solar module performance and shows the importance of introducing some LT structure on the rear interface of the bifacial solar module.

For the monofacial solar module architecture, the consideration of albedo radiation
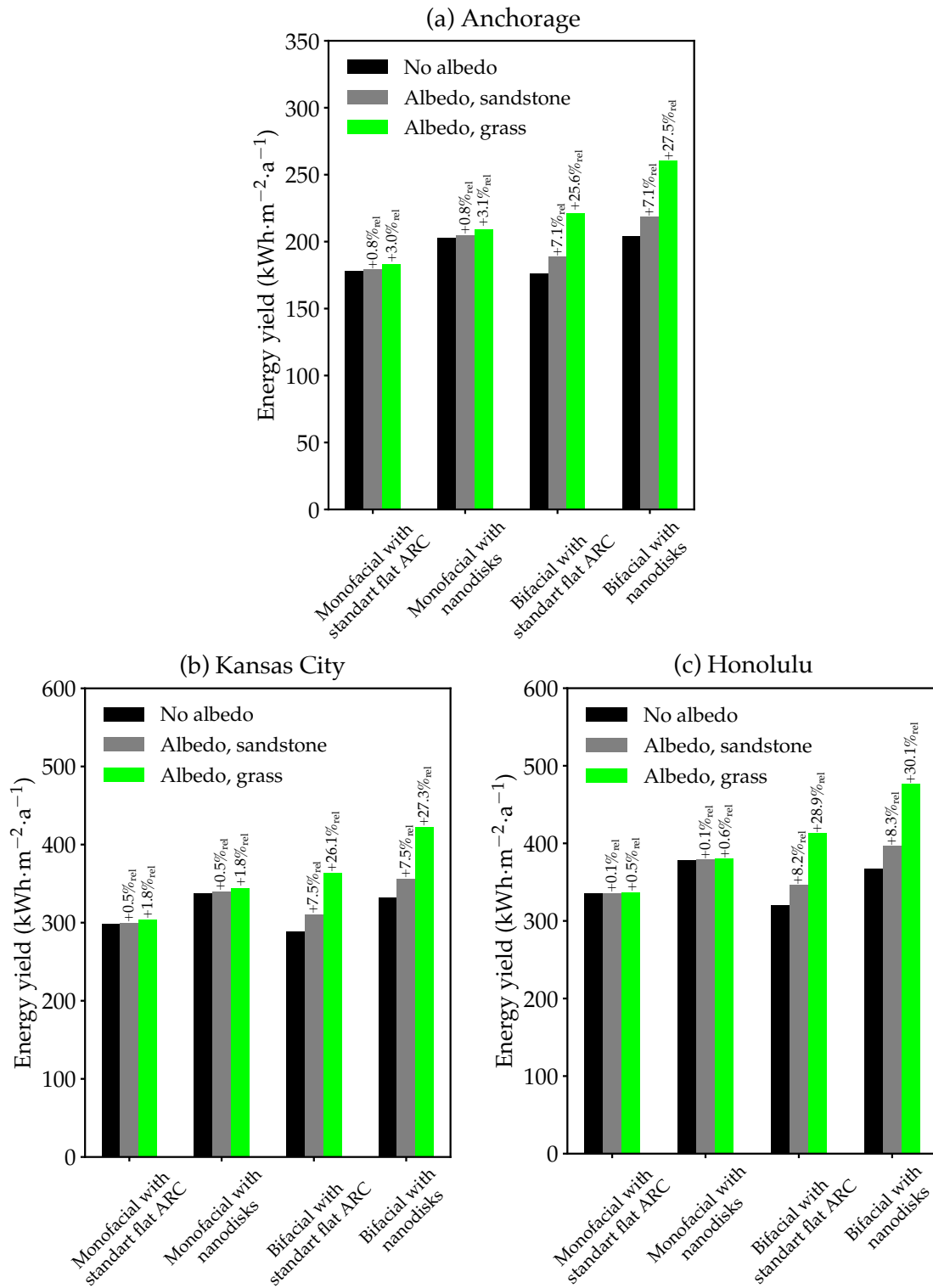
FIGURE 4.7: Annual EY of the module architectures (a)-(d) from Fig. 4.1 for different cities when albedo irradiation is taken into account. For all solar module architectures, the c-Si wafer thickness was 40 μm. Adapted with permission from [P2]. © 2021 Optical Society of America.

does not significantly influence the annual EY since the only channel for such radiation being absorbed in the c-Si wafer is through the light reflected from the ground and hits the solar module on the front. On the other hand, one can observe an excellent boost

of the annual EY as soon as albedo is considered for the bifacial solar module. The increase of the annual EY for the monofacial module architecture varies depending on the module tilt angle, and it is more significant for the locations with greater θ_m such as Anchorage. The relative improvement of the annual EY went up to approximately $0.8\,\%_{rel}$ with sandstone and $3.0\,\%_{rel}$ with grass as a ground surface for both the reference solar module with standard flat ARC and the solar module with the nanodisks with insignificant difference between them. For the bifacial solar module, a stronger boost of the annual EY is expected for the sunnier locations such as Honolulu. The relative increase of the annual EY went up to $8.2\,\%_{rel}$ with sandstone and $28.9\,\%_{rel}$ with grass as a ground surface for the reference solar module with standard flat ARC. For the solar module with the nanodisks, the relative increase of the annual EY was found to be $8.3\,\%_{rel}$ and $30.1\,\%_{rel}$ with sandstone and grass ground surface, respectively.

4.5 Conclusions

In this chapter, we analyzed the annual EY under realistic irradiation conditions for the mono- and bifacial c-Si HJT solar module architectures with AR and LT TiO_2 square nanodisk arrays introduced at the solar cell-encapsulation front and rear interfaces, respectively. We compared their performance to the annual EY of reference solar modules with the standard flat ARCs. We showed that while the c-Si wafer thickness is reduced down to $5\,\mu$m, the relative increase of the power output of the mono- and bifacial solar modules can reach up to $23.3\,\%_{rel}$ and $43.0\,\%_{rel}$, respectively, when the nanodisk arrays are introduced. This improvement is comparable for the three considered locations characterized by contrasting irradiation conditions. Moreover, consideration of albedo radiation for the bifacial solar module architecture boosts the annual EY even further. We also compared the power output of the solar modules with nanodisks to the state-of-the-art solar modules with random pyramidal texture for one location and a few selected c-Si wafer thicknesses. Although the latter outperforms the solar modules with nanodisks, the proposed designs with the TiO_2 nanodisks prove to be an excellent alternative when thinner c-Si wafers are considered, and their texturing becomes tricky.

The proposed nanodisk arrays for the front and rear solar cell-encapsulation interfaces have a substantial impact on the light absorption in the c-Si wafers. However, their AR and LT properties are decoupled. The design of the AR nanodisk coating was inspired by the results presented in chapter 3, and the size of the individual nanodisk and the lattice pitch is rather small. The broadband backscattering suppression by this square nanodisk array is closely related to the ability of the system to suppress the cross-talk between the opposite handednesses of the electromagnetic field. On the other hand, the LT nanodisk array is formed by the sparsely spaced nanodisks with larger geometrical parameters, which allows for efficient scattering into multiple scattering directions.

5. Anti-Reflective Nanostructures with Tailored Disorder

This chapter will discuss the performance of c-Si HJT solar cells coated with tailored disordered nanodisks. After a short introduction in Sec. 5.1, we will discuss the fabrication technique used to create the nanodisk coating in Sec 5.2. Section 5.3 will focus on the optical performance of the disordered nanodisk coating and how it compares to the periodic one, while Sec. 5.4 will discuss the influence of the fabrication process on the opto-electronic properties of the fabricated devices. The content of this chapter is mainly based on [P3]. This project was carried out in close collaboration with Dr. Peter M. Piechulla from the Institute of Physics at the Martin-Luther-University Halle-Wittenberg, who deposited the nanodisks on top of the solar cell samples. Additionally, he performed the calculations involving the Born approximation (shown in Figs. 5.5, 5.6 and 5.10) and generated the nanodisk pattern for the FDTD simulations (Fig. 5.4). Special thanks go to Dr. Derk Bätzner from Meyer Burger Research AG in Hauterive, Switzerland, for his support regarding the characterization of the samples, and Prerak Dhawan from TFP at KIT, who contributed with some scripts used to perform the FDTD calculations.

5.1 Introduction

Dielectric nanostructures and, in particular, nanodisks have proven to be excellent candidates as an alternative for improving light harvesting in solar cells to common strategies involving texturing of the c-Si wafer or flat ARCs [41, 43, 120]. However, the critical question is how to arrange such nanostructures. While an impressive broadband response has been shown for disordered arrangements [121–124], one can design the periodic coatings such that they suppress all off-axis scattering [41]. We will show that we can achieve the complete off-axis scattering suppression in the case of a disordered arrangement if spatial correlations are tailored appropriately [125, 126].

The disordered ARC discussed in this chapter was inspired by the similar but periodic design which we covered in chapter 3. The properties of the latter coating were analyzed concerning helicity preservation of the scattered light. We previously established that one has to fulfill two conditions to achieve a complete backscattering suppression. First, a sufficiently high degree of rotational symmetry of the system along the illumination direction is required. In addition, perfect helicity preservation is needed, which is possible only for electromagnetically dual systems that exhibit equivalent electric and magnetic responses. In a more realistic scenario, helicity preservation can be achieved for on-axis illumination of high-index nanodisks since the aspect ratio of such scatterers can be tuned to balance electric and magnetic dipolar responses.

For a periodic arrangement, such as a square or hexagonal nanodisk lattice, the condition of discrete rotational symmetry $2\pi/n$ with $n \geq 3$ is readily met. We have shown in chapter 3, that even though such designs can approach perfect helicity preservation and eradicate the backscattering at a single or at most at a few discrete wavelengths, the effect of the periodic coating is rather broadband and suitable for the spectral range relevant for solar cells. In the case of a disordered system, we can not precisely apply the concept

of discrete rotational symmetry. However, for an appropriately tailored pattern, we can speak of an effective continuous rotational symmetry ($n \to \infty$). Consequently, we can establish a one-to-one relationship between the helicity preservation and the coated solar cell's AR properties for the wavelength range where the off-axis scattering is minimized.

Despite the attractive properties of the proposed designs involving photonic nanostructures, they were hardly considered for implementation on an industrial scale. The wafer-based c-Si solar cells continue to dominate the market, and the standard pyramidal textures pose a challenging benchmark. Additionally, the fabrication of nanophotonic structures often relies on expensive and slow fabrication methods such as e-beam lithography. We also note that many techniques require specially prepared substrates such as polished surfaces. It is evident that scalability is of paramount importance for a designed nanostructure to be used for practical applications. Fabrication techniques like nanoimprint lithography [127, 128] are in principle scalable, and promising results were already reported for the solar cells in the sub-centimeter range [129]. Nevertheless, hardly any results were reported for the solar cells with multiple square centimeter areas.

In this chapter, we will show through experimental and numerical results that a dielectric high-index nanodisk ARC can visibly improve the performance of a solar cell of standard industrial design. We note that the c-Si wafers used for our samples had a non-textured, damage-etched surface, thus demonstrating the robustness of the proposed fabrication method concerning the topography of the substrate. Moreover, we will show that the processing required for the employed fabrication method does not deteriorate the electrical properties of the solar cells. We will discuss the differences of the system with disordered nanodisk coating to a similar but periodic system with equivalent nanodisk density. Additionally, we will draw a parallel between the results for a solar cell covered with disordered nanodisks and a solar cell covered by the nanodisks arranged in a square lattice in terms of the helicity preservation properties of these systems.

5.2 Sample fabrication

The nanodisks were deposited on top of industrial-type HJT rear emitter solar cells. The schematic image of such a coated cell is shown in Fig. 5.1. The solar cells employed in the experiment were fabricated from $150\,\mu$m Czochralski c-Si wafers. The mostly flat surface of the c-Si wafers was achieved through adapting the wet-chemical damage etch process. The wafers were passivated by a-Si:H, and the total thickness of the front a-Si:H (passivation intrinsic and n^+-doped layers) was the same as for the solar cells discussed in chapter 3. We used two types of front ITO contact layers. The reference devices were optimized for the highest efficiency under standard conditions and had an 80 nm front ITO layer. The TiO$_2$ nanodisks were deposited on top of the solar cells, for which the front ITO contact layer thickness was 50 nm. These adapted thinner ITO layers had higher doping levels and carrier concentration to compensate for the loss of conductivity caused by the lower thickness. Similar a-Si (passivation intrinsic and p^+-doped) and ITO layers were deposited on the rear side of the devices. The target dimensions of the individual nanodisks were the same as in the design discussed in chapter 3: the diameter was 300 nm and height was 100 nm. Refractive indices for c-Si and ITO, which we used in the calculations, were taken from literature [72, 105]. Refractive index data for a-Si:H, TiO$_2$, and Al$_2$O$_3$ were obtained by ellipsometry, and the corresponding n and k values can be found in Appendix A.

Overall, 81 samples with dimensions of 39 x 39 mm^2 were laser-cut from fully processed 156 mm HJT solar cells with silver contact fingers, such that the processing capabilities for the subsequent nanodisk fabrication process could be matched. The samples were fabricated using a novel colloid-based nanofabrication method [130], [P4], and its steps
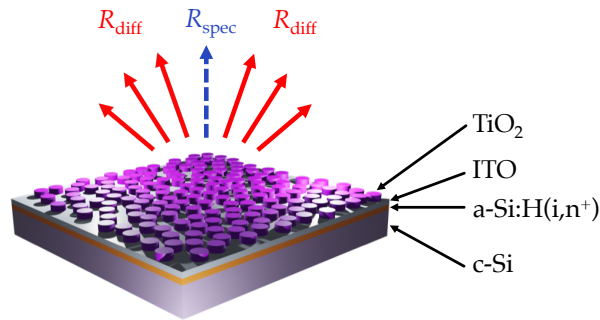
FIGURE 5.1: Schematic illustration of a HJT solar cell stack with a disordered TiO$_2$ nanodisk coating. R_{diff} and R_{spec} denote the diffuse and specular parts of reflectance, which will be discussed in Sec. 5.3.2. The nanodisks were deposited on fully processed HJT rear emitter solar cells, for which the front surface of a mostly flat unpolished c-Si wafer was coated with a-Si:H (passivation intrinsic and n^+ doped layers). A transparent conductive ITO layer served as both ARC and front contact. The devices included screen-printed silver contact fingers (not shown) but no busbars. Adapted with permission from [P3]. © 2021 American Chemical Society.

are shown in Fig. 5.2. This method is based on self-organizing colloidal particles which are deposited on top of a functionalized surface, and the patterns of these particles are subsequently transferred to a TiO$_2$ layer employing RIE. In the first step of the process, the TiO$_2$ layer of 105.5 nm thickness was deposited using ALD at 120°C using alternating pulses of titanium tetrachloride (TiCl$_4$) and water (1800 pulses each) in a Beneq TFS-200 thermal ALD tool. On top of this film, a 16.8 nm layer of aluminum oxide (Al$_2$O$_3$) was deposited at 120°C using 150 pulses of both trimethylaluminium (TMAl) and water as functionalization for the PMMA nanosphere deposition process. We used ALD since this method allows great control over the thicknesses of the deposited films and produces dense layers. The thin top Al$_2$O$_3$ served two purposes. First, the surface charges of this layer were crucial to immobilize the PMMA nanospheres in the subsequent deposition process thereof. Moreover, this layer transformed into a hard mask imprinted by the PMMA nanospheres [P4].

In the next step, our samples were exposed to an aqueous dispersion of the PMMA nanospheres (microParticles Berlin GmbH, Germany) with a diameter of 350 nm. These nanospheres formed an evenly distributed arrangement on the surface. This deposition technique exploits the electrostatic interactions of the surface-charged nanospheres with each other and with the Al$_2$O$_3$ film. The negatively charged PMMA nanospheres are driven towards the positively charged substrate. They are immobilized when they adsorb on the surface of the sample. The deposited nanospheres repel each other. This way, the probability of the location of adsorption for another nanosphere is modified. When a certain density of PMMA nanospheres attaches to the surface of the substrate, no more of these nanospheres will adsorb since the repelling forces caused by already attached nanospheres become dominant. Thus, this bottom-up fabrication process is self-limiting in addition to being self-organized, which makes this technique very cost-effective [P4]. In the subsequent step, the substrate covered with PMMA nanospheres was tempered for 30 mins at 135 °C such that the shape of the nanospheres became dome-like, improving the surface coverage, and the nanoparticles could serve as an etch mask for RIE. The increase of the disk diameter from the target dimension of 300 nm to 370 nm was most likely caused by this step. Lastly, the etching was performed in two steps. First, the Al$_2$O$_3$ film was structured employing a Chlorine-containing plasma. Next, the structured
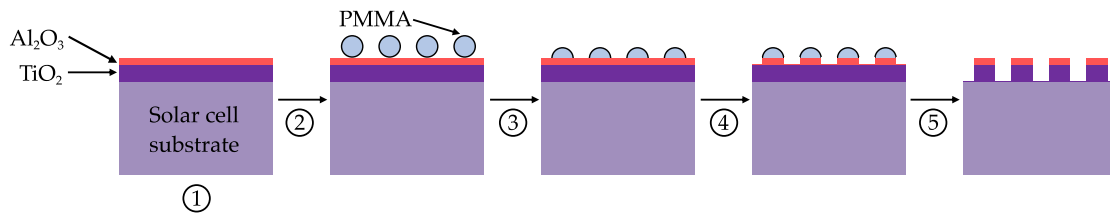
FIGURE 5.2: Illustration of the fabrication process of disordered nanodisks on top of a HJT solar cell using colloid-based nanofabrication method. The flow of the process was the following: (1) HJT solar cell precursor substrate was functionalized with TiO_2/Al_2O_3 layers; (2) the self-organized PMMA nanosphere process was applied; (3) the substrate was tempered for 30 minutes at 120 °C, which resulted in the formation of the domes serving as an etch mask; (4) first step of the etch process: the Al_2O_3 layer was structured using a Chlorine-containing plasma; (5) second step of the etch process: Al_2O_3 was used as a hard-mask in a Fluorine-based process to etch TiO_2 layer selectively. The precursors were prepared by Meyer Burger Research AG staff in Hauterive, Switzerland. The steps (1) through (5) were performed by Dr. Peter M. Piechulla from the Institute of Physics at the Martin-Luther-University Halle-Wittenberg.

Al_2O_3 layer was used as a hard-mask in a Fluorine-based process to etch TiO_2 selectively. The ITO layer under the TiO_2 film was only slightly etched in Fluorine-based plasma while serving as an etch-stop layer.
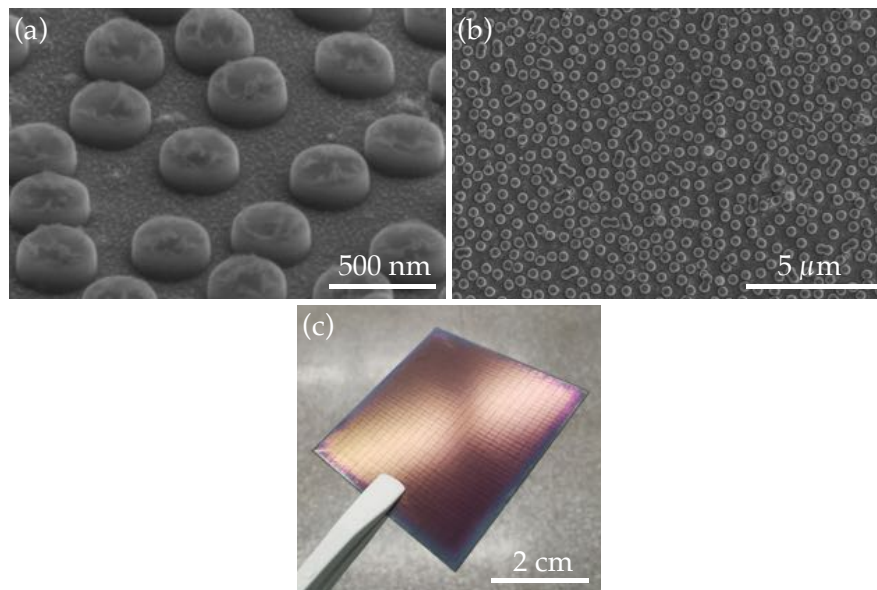
FIGURE 5.3: (a),(b) SEM images of the nanodisks deposited on top of a HJT solar cell on different magnification stages. The image in (a) highlights the features of the individual disks, while the image (b) highlights the uniformity of the samples. (c) Photograph of a 39 x 39 mm^2 coated HJT solar cell. The SEM images and the photograph were taken by Dr. Peter M. Piechulla from the Institute of Physics at the Martin-Luther-University Halle-Wittenberg. Adapted with permission from [P3]. © 2021 American Chemical Society.

The SEM images of a HJT solar cell coated with disordered TiO_2 nanodisks and its photograph are shown in Fig. 5.3. The nanodisks with a diameter of 370 nm and height

of 122 nm (with 106 nm of TiO_2 and 16 nm of Al_2O_3) covered the entire front surface of the sample in a disordered pattern [Fig. 5.3(a),(b)]. Notably, this process is not affected by any previously present structures, including an uneven surface morphology caused by the residue roughness after the damage etch process and silver contact fingers [Fig. 5.3(c)]. Although some edge effects are visible, they most likely stem from the laser-cutting of the samples from the full-size industrial-type solar cells since a single sample size was limited due to the laboratory scale fabrication tools for ALD of TiO_2 and Al_2O_3 and RIE for the structuring of these layers. We note that slow deposition of a relatively thick TiO_2 layer could be achieved faster employing PECVD [131, 132] or sol-gel [129] deposition. Additionally, the directional plasma etching processes work well in the high-throughput inline machines [133, 134]. It is important to note that this colloid-based self-organized fabrication process can be carried out using standard equipment. Using this novel technique, we fabricated multiple samples with varying nanodisk densities and subsequently analyzed their optical and electrical properties.

5.3 Optical performance of a solar cell with disordered nanodisk coating

5.3.1 Calculation of reflectance

This section will discuss in detail the optical properties of a HJT solar cell coated by disordered nanodisks and compare the measured reflectance spectrum to the simulated one. We calculated reflectance by applying different approaches. For the periodic simulation, where we assumed a lattice pitch that leads to the nanodisk density of the disordered sample, we employed FEM. Here, we calculated reflectance in the same manner as it was done in chapter 4, using the following equation:

$$R_{\text{periodic}} = \frac{\sum\limits_{k_r} |\tilde{E}(k_{r,x}, k_{r,y})|^2 \cdot \cos(\theta_r)}{|E_0|^2}.$$

(5.1)

In the equation above, the angular spectrum $\tilde{E}(k_{r,x}, k_{r,y})$ is determined through Fourier transform of the field in real space obtained from full-wave simulations. Here, k_r is the wave vector of a respective reflected electromagnetic plane wave, and θ_r is the angle between such a vector and the z-axis. The total reflected power is then divided by the incident power, with E_0 being the amplitude of a normally incident and linearly polarized plane wave. In the FEM simulations discussed in this chapter, a non-absorbing semi-infinite c-Si substrate was assumed.

For the simulation of the disordered sample, we employed the first Born approximation [53]. The Born approximation assumes the exciting light field for each nanodisk to be the unperturbed incoming light field. This approach has already been applied to the disordered arrangements of nanodisks in [P4]. Although it neglects near-field interaction and multiple scattering effects, it provided a reasonable prediction of the scattering response for our system and proved to be a useful tool of analysis. Since the nanodisks are arranged in a two-dimensional pattern in a plane perpendicular to the incident electric field propagating in z-direction, the coupling between the nanodisks is considerably lower than it would be for an equivalent three-dimensional pattern of nanodisks with a similar density. Thus, we consider the individual nanodisks to be excited only by the external illumination $E_{\text{in}} = E_0 e^{i(k_0 z - \omega t)}$ and can use the first Born approximation. The scattered electric field of an individual scatterer has the form of a spherical wave in the far field and reads as [135]

$$E_s(r) = E_0 \frac{e^{ikr}}{r} f,$$

(5.2)

where we omit the time dependence $e^{-i\omega t}$. In the equation above, the form factor $f = f(\hat{E}_0, k_0, k)$ describes the normalized field amplitude for an incident electric field with polarization $\hat{E}_0 = E_0/|E_0|$, where k_0 and k denote the wave vectors of incoming and scattered fields, respectively. We obtained f through FEM simulations by applying a model with the geometrical parameters identical to those of a periodic simulation, albeit with transparent boundary conditions for all edges of the computational domain.

Let us now consider only the components scattered perpendicular to the nanodisk plane in forward direction with $k^+ = n_{\text{c-Si}}k_0 e_z$ (silicon half-space) and backward direction $k^- = -k_0 e_z$ (air half-space) of an individual nanodisk illuminated with a linerly polarized plane wave $k_0 = k_0 e_z$. We can then use the angular spectrum representation of Eq. 5.2 in its asymptotic limit ($kr \rightarrow \infty$) to calculate specular transmission T and reflection R [136]:

$$T_{\text{spec}} = n_{\text{c-Si}} \left| t\hat{E}_0 + \rho \frac{2\pi}{i|k^+|} f(k = k^+) \right|^2, \tag{5.3}$$

$$R_{\text{spec}} = \left| r\hat{E}_0 + \rho \frac{2\pi}{i|k^-|} f(k = k^-) \right|^2, \tag{5.4}$$

where t and r correspond to the Fresnel transmission and reflection coefficients of the planar layer stack, and ρ is the density of the nanodisks. Since we neglect the interaction between the nanodisks, the transmittance and reflectance do not depend on the particular arrangement but rather on the nanodisk density ρ. The scattered fields of the individual nanodisks in the normal direction are in phase and interfere with $t\hat{E}_0$ and $r\hat{E}_0$ of the planar layer stack. This interference determines the scattered power, and if absorption within the scattering element is neglected, we will have, due to the energy conservation, the following expression:

$$1 - T_{\text{spec}} - R_{\text{spec}} = T_{\text{diff}} + R_{\text{diff}} = P_{\text{diff}}, \tag{5.5}$$

where T_{diff} and R_{diff} denote the diffusive contributions to transmission and reflection, and P_{diff} is the normalized scattered power without specular components.

At the same time, the scattered power has to be equivalent to the integral of the angular resolved scattering (ARS) over the unit sphere Ω (excluding $d\Omega = d\Omega(k = k^\pm)$) with $P_{\text{diff}} = \int_\Omega ARS \, d\Omega$. In general, the ARS of the interface containing an array of the identical scatterers such as our nanodisks depends on two properties: the arrangement of the nanodisks (e.g., periodicity or the distances between the individual nanodisks) and the properties of the individual nanodisks (size, shape, and the material they are made of). The structure factor S describes the former property, while the form factor f describes the latter. Nevertheless, either of these quantities describes the scattering response of the system containing the array of the nanodisks almost completely. The structure factor dominates the periodic arrangements, and the scattering from such an arrangement is only allowed into a small portion of all available angular directions (diffraction orders), while any other direction is prohibited with the structure factor being zero. On the other hand, in the case of an entirely random arrangement of the nanodisks, no particular scattering direction is either enhanced or suppressed due to the arrangement of the nanodisks. Thus, the scattering response of the array becomes identical to that of the individual nanodisks [P4]. The spatial configuration of the nanodisks discussed in this chapter lies in the parameter space of correlated disorder. With that, it is between the two opposed cases described above and the AR properties of the nanodisk coating are achieved by tailoring the disorder appropriately.

The ARS can be obtained by modulating the individual nanodisk scattering response $|f|^2$ with the structure factor $S(q = k_{||})$, where $k_{||}$ is the projection of the scattered wave

vector k to the plane containing the nanodisk pattern, and the ARS should be scaled to satisfy Eq.5.5:

$$ARS = \frac{P_{\text{diff}}}{\int_{\Omega} |f|^2 \, S \, d\Omega} \cdot |f(k)|^2 \, S(k_{\parallel}) \qquad k \neq k^{\pm}. \tag{5.6}$$

We obtained the structure factor $S(q = k_{\parallel})$ from digitized SEM images from where N particle positions r_i have bean extracted and reads as [130, 137]

$$S(q) = \frac{1}{N} \sum_{i,j}^{N} e^{-iq(r_i - r_j)}. \tag{5.7}$$

We note that we use the notation q for the components of the wave vectors that lie in the nanodisk array plane and k for the wave vectors of propagating free-space modes, which usually have a non-zero component perpendicular to the plane containing the nanodisks. The diffusive part of reflectance can be obtained by integrating the *ARS* over the half-sphere Ω' in air, using the following equation:

$$R_{\text{diff}} = \int_{\Omega'} ARS \, d\Omega \qquad k \neq k^{-}. \tag{5.8}$$

Additionally, we performed simulations using the FDTD method. This approach was used to calculate the scattered powers corresponding to the positive and negative helicities in analogy to the calculations in chapter 3. For this, we determined the scattered field in the frequency domain after performing the discrete Fourier transform of the field in the time domain, subsequently obtaining the angular spectrum. The helicity decomposition was performed as was described in Sec. 3.2.1. The obtained angular spectrum was also used to calculate the specular and diffuse parts of reflectance. The total reflectance was calculated from the energy flux of the backscattered field by dividing the outgoing energy flux by the energy flux of the incident plane wave.

We performed FDTD simulations for a nanodisk pattern with an optimized statistics. The resulting pattern is shown in Fig. 5.4(b). We started with a numerically generated pattern of $N = 27$ nanodisks while applying periodic boundary conditions in real space [Fig. 5.4(a)]. This initial pattern was generated using a random sequential adsorption (RSA) of soft particles [130]. The most appropriate statistical measure to characterize such a pattern concerning its scattering properties is the structure factor $S(q)$. Thus, starting with the generated pattern, we applied a collective coordinate control approach shown by Uche *et al.* [138] to force $S(q = q_x, q_y)$ to match the experimentally determined structure factor $S_0(q)$ via minimizing the potential

$$\phi(r_i, ..., r_n) = \sum_{q \in Q} [S(q) - S_0(q = |q|)]^2, \tag{5.9}$$

where r_i are the nanodisk positions. The result of such an optimization is shown in Fig. 5.4(f). We are especially interested in the range $|Q| \leq 2\pi/l$ corresponding to scattering at wavelengths $\lambda_0 > l$, where l is the lattice constant of the periodic grating leading to an equivalent nanodisk density. For wavelengths below $\lambda_0 = l$, the off-normal scattering or diffraction will occur irrespective of the nanodisk arrangement (i.e., independent of whether this arrangement is disordered or periodic). The optimized pattern shown in Fig. 5.4(b) is used for all FDTD simulations which will be discussed in this chapter. We note, that for the FDTD simulations, a semi-infinite non-absorbing c-Si substrate was assumed.
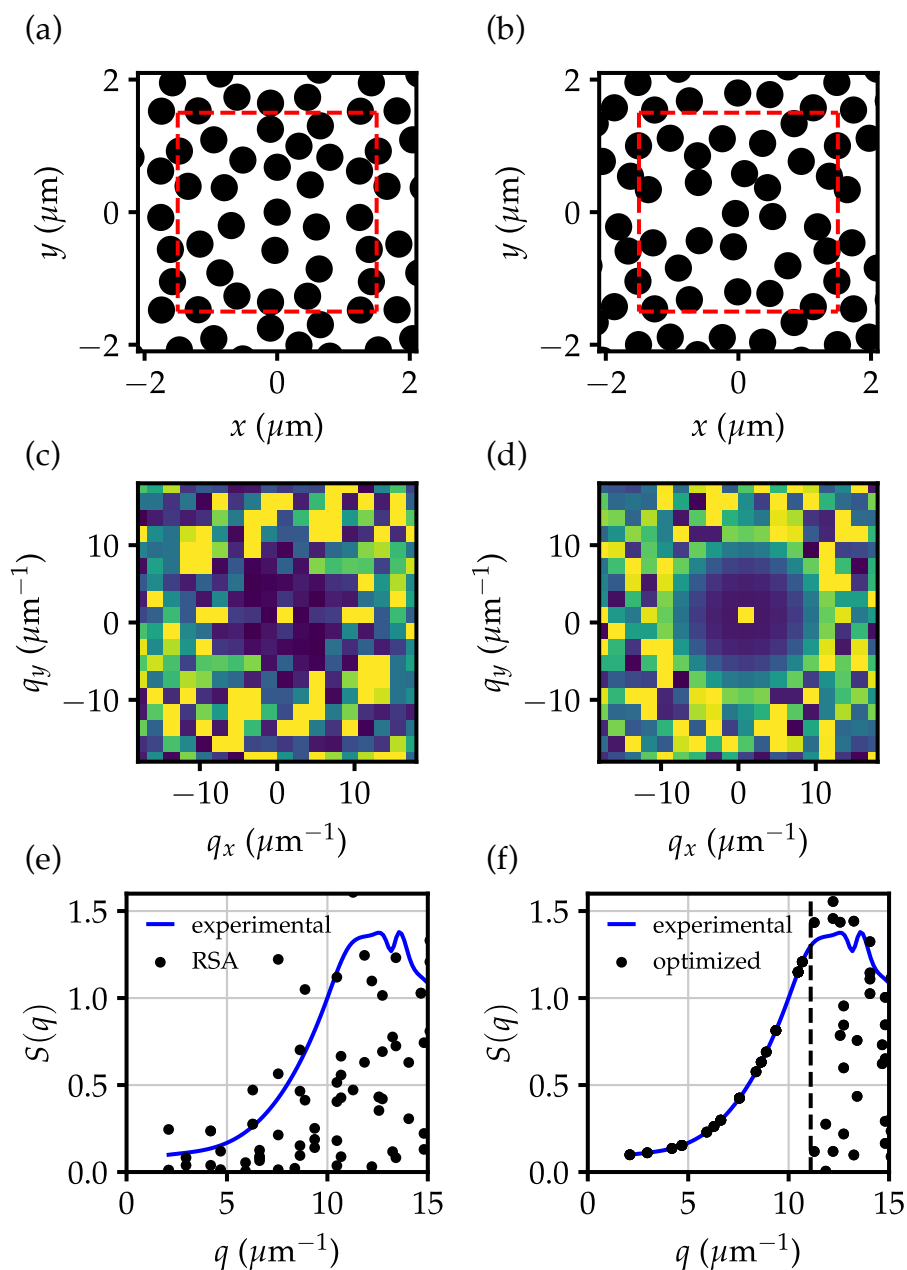
FIGURE 5.4: Left column: Pattern of 27 nanodisks on a domain of 3×3 μm^2 generated via random sequential adsorption (RSA) of soft particles under periodic boundary conditions (this yields the nanodisk density of 3.0 μm^{-2}). Right column: Optimized sample via collective coordinate control to match the structure factor obtained from the experiment. (a), (b) Real space nanodisk pattern. The unit cell is marked with red dashed lines. (c), (d) Two-dimensional structure factor. (e), (f): Spline interpolation of the angular averaged experimental structure factor and the points from two-dimensional structure factor at $q = |\boldsymbol{q}|$. The dashed black line corresponds to a periodic structure's lattice constant l with equivalent nanodisk density. Adapted with permission from [P3]. © 2021 American Chemical Society.

FIGURE 5.5: Reflectance of a HJT solar cell coated with a nanodisk pattern calculated via Born approximation and FEM simulation of a single nanodisk compared to the measured reflectance spectra (nanodisk density of 3.0 μm^{-2}). In addition to measured reflectance of a nanodisk coated sample, we 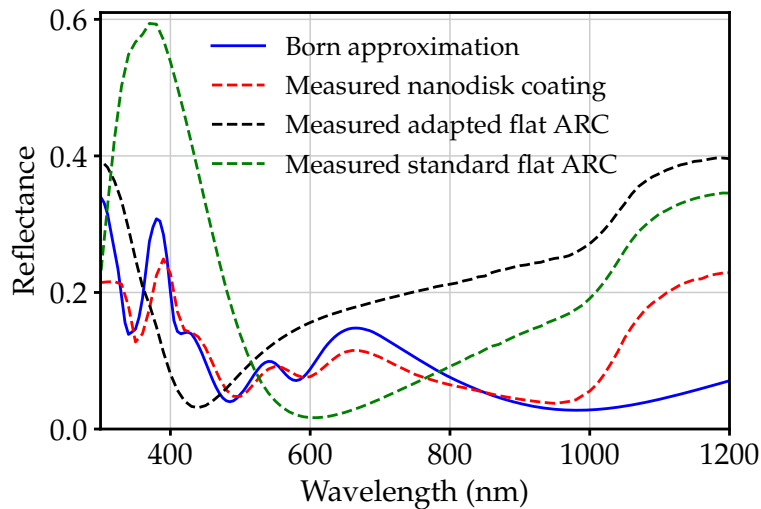also show the reflectance spectra for an adapted flat ARC (50 nm ITO) the nanodisk structure is based on and for a standard flat ARC reference (80 nm ITO) as a benchmark. Adapted with permission from [P3]. © 2021 American Chemical Society.

5.3.2 Comparison of measured and simulated reflectance

Figure 5.5 shows the result of the application of the first Born approximation discussed in Sec. 5.3.1 to a solar cell sample with disordered nanodisks and how it compares to measured reflectance in the case of the optimal nanodisk density of 3 μm^{-2}. The reflectance spectra discussed in this chapter were measured at Meyer Burger Research AG in Hauterive, Switzerland, employing the LAMBDA 750 UV/Vis/NIR tool. The measured reflectance curve for the sample with the nanodisk coating includes all the major features predicted by our theoretical model, although it shows an increased reflectance in the wavelength region above 1000 nm. This increase is present for all the measured spectra due to reflectance at the rear side of the solar cell, which was not considered in our calculations. We note that the nanodisk structure discussed here was not optimized for light trapping. Nevertheless, the simulation results discussed in chapter 4 indicate that the nanodisks of the size we use here most likely improve the absorptance in c-Si mainly through their AR rather than LT properties.

The most prominent deviation of the measured reflectance from the calculated one was found at the wavelength around 650 nm and was of about 4 %$_{abs}$. This difference was likely the result of slight differences between the model parameters of the FEM simulation for an individual nanodisk and the fabricated nanodisks. For example, the surface roughness on top of the nanodisks, which can be seen in Fig. 5.3(a), was not included in the simulation. Additionally, in the calculation employing the Born approximation, the nanodisks were assumed to lie in one plane, while in the experiment, this was not the case since the c-Si wafers were not polished. We also note that the deviation of the calculated reflectance from the measurements at wavelengths below 380 nm stems from the assumption that the nanodisks were nonabsorbing. We note that this was not a severe assumption since the imaginary part of the refractive index of TiO_2 is rather small in the considered spectral region.

The ITO front contact layer of the solar cells covered with nanodisks has been adapted

to 50 nm, as has been already done for the system discussed in chapter 3. The design of the periodic nanodisk coating presented in chapter 3 served as an inspiration for the disordered nanodisk coating analyzed here. The thickness of the ITO front contact layer of a standard flat ARC reference was 80 nm, which was optimized for the AM1.5G spectrum [66]. The measured reflectance spectra for both these references are shown in Fig. 5.5. For the sample with adapted flat ARC, the reflectance minimum was shifted to a shorter wavelength when compared to the sample with standard flat ARC. When we added the nanodisk coating on top of the sample with an adapted ITO layer, reflectance was also reduced in the long wavelength region. Even though reflectance of the sample with a standard flat ARC was measured to be lower at wavelengths around 600 nm, throughout most of the spectrum, we observed lower reflectance of the measured disk sample, which clearly shows the effect of the nanodisk coating. We note that for this design, the results shown here are expected to be robust to small changes of the nanodisks' dimensions up to around 20 % as it was for the periodic nanodisk coating considered in chapter 3. Thus, minor deviations of the sizes of the fabricated nanodisks from the target dimensions still allowed for a considerable improvement of the AR properties.

5.3.3 Specular and diffuse reflectance and helicity decomposition

We have shown in chapter 3 that the periodic arrangement of TiO$_2$ nanodisks can significantly reduce reflection losses of a HJT solar cell layer stack. Here, we employ the FEM to simulate reflectance of a periodic structure with the nanodisk density equivalent to that of the structure with a random nanodisk arrangement. The geometrical parameters of the solar cell layer stack and an individual nanodisk used in this simulation were the same as in the case of the FEM simulation of the individual nanodisk on the solar cell substrate for obtaining the form factor. In contrast to the calculation employing the first Born approximation, we considered absorbing TiO$_2$ nanodisks. The comparison of the results obtained through Born's approximation and FEM simulation of the periodic grid with equivalent nanodisk density is shown in Fig. 5.6(a). These reflectance spectra were found to be almost congruent at wavelengths below $\lambda_c = 577$ nm. This cutoff wavelength corresponds to the lattice constant of the periodic grating of an equivalent nanodisk density of 3 μm. The discrepancies in the spectra for the wavelengths below 350 nm are due to absorption in TiO$_2$ nanodisks, which is not included for the Born's approximation model and becomes significant in the short wavelength region.

The wavelength range above $\lambda_c = 577$ nm, for which we observed the strongest deviation between the Born approximation and periodic simulation, is important for the solar cell performance since the solar irradiance is quite strong in this range. To better understand the increased reflectance above λ_c, we decomposed the calculated reflectance using the first Born approximation into specular and diffuse parts as was described in Sec. 5.3.1 [Fig. 5.6(a)]. The diffusive contribution to reflectance strongly exceeded the specular, with the difference found to be particularly strong in the wavelength range between 600 nm and 1000 nm. The diffusive reflection can only occur when $S(q) \neq 0$. The structure factor $S(q)$ of our disordered nanodisk pattern [Fig. 5.6(b)] has a peak at around $q \approx 12.5$ μm^{-1} and for large q converges to 1. For smaller values of q, it decays from its peak value down to about $S_{\min} \approx 0.06$, which corresponds to the density fluctuations being suppressed on large length scales [130, 139], [P4]. In Fig. 5.6, we marked the wave vector corresponding to a vacuum wavelength λ_c. At $q = k(\lambda_c)$, the structure factor $S(q)$ is relatively large. However, for longer wavelengths, the relevant range for scattering is restricted to smaller q, and we observed reduced scattering due to $S(q)$ being small in this range. We note that for a periodic nanodisk array with a grating vector $|\boldsymbol{q}| = q_c = 2\pi/577$ nm, all $S(q < q_c)$ vanish. In contrast to our disordered sample, the periodic nanodisk arrangement from the simulation shown in Fig. 5.6(a) does not support any propagating modes apart from
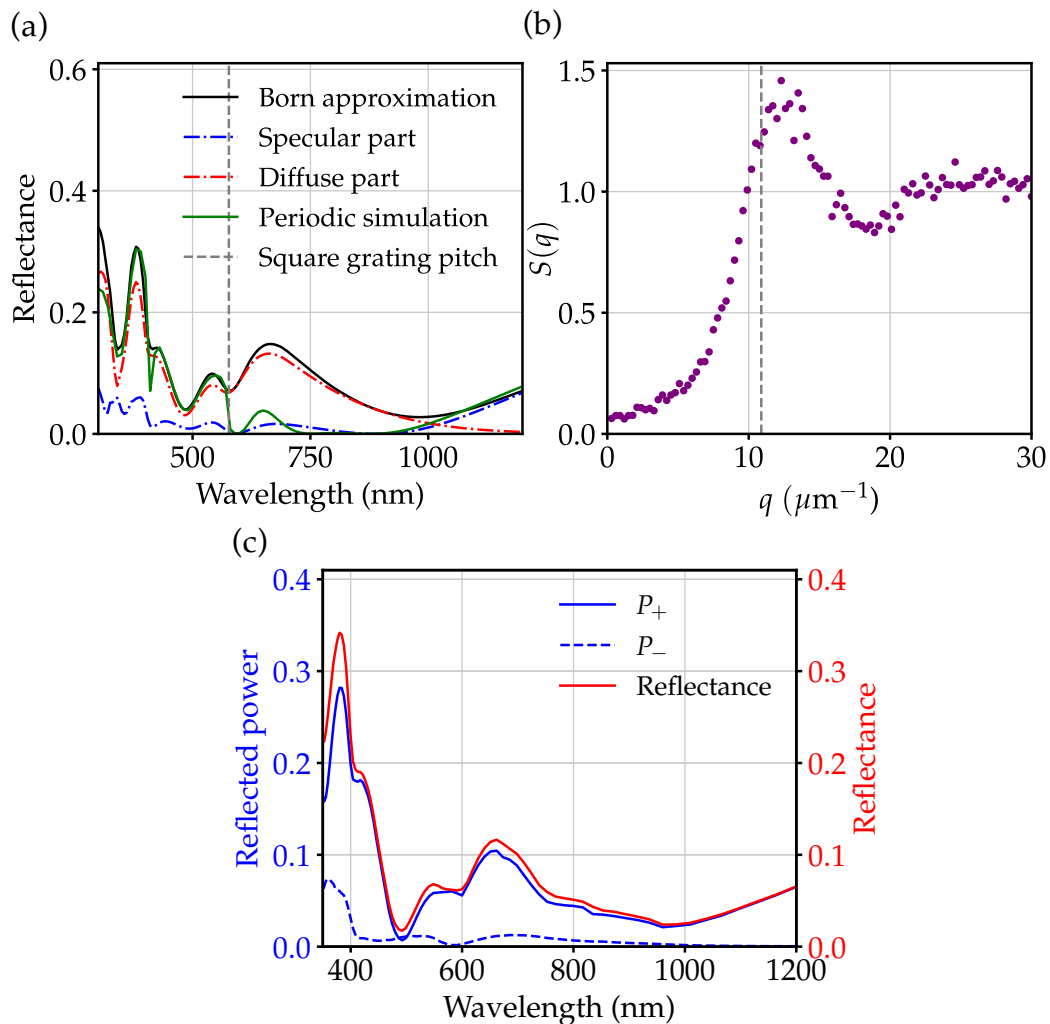
(a)

(b)

(c)

FIGURE 5.6: (a) Decomposition of the total reflectance (calculated employing the first Born approximation) into its specular and diffuse parts, and comparison to a nanodisk pattern in a square array with a grating pitch of 577 nm, which is equivalent to the nanodisk density of 3.0 μm^{-2} of the disordered pattern. (b) Structure factor of the nanodisk pattern calculated from a digitized SEM image. The dashed line marks q corresponding to 577 nm vacuum wavelength. (c) Simulated reflectance using the FDTD method of a disordered disk arrangement similar to the experiment and decomposition into normalized reflected powers of the fields of positive and negative helicity, P_+ and P_-, respectively. The incident field had negative helicity (right-handed circular polarization of incoming plane wave). The nanodisk pattern used for this simulation is shown in Fig. 5.4. Adapted with permission from [P3]. © 2021 American Chemical Society.

the zeroth diffraction order, leading to the lower reflectance starting from 577 nm.

In comparison to the periodic system discussed in chapter 3, the exact discrete rotational symmetry required for helicity preservation is lost in a disordered system, thus not meeting one of the two requirements for zero backscattering. On top of that, the non-specular scattering is allowed by $S(q) \neq 0$, although the requirement for zero reflectance is only applicable along the symmetry axis of the scatterers (see Sec. 2.1.5), i.e., for the specular component. However, if the disordered nanodisks arrangement is tailored appropriately, it can overcome both of these restrictions. There is a subclass of the particle

arrangements, for which the following equality holds:

$$S(0 < q \leq Q) = 0. \tag{5.10}$$

This is true in the range Q around the origin, which is called *stealthy hyperuniform* [125]. For ordered systems, this condition is trivially met. The disordered system can also be tailored to satisfy Eq. 5.10. Such systems are called *disordered stealthy hyperuniform*. These disordered systems do not possess Bragg peaks and are fully isotropic, thus possessing an effective continuous rotational symmetry [140]. While the diffuse reflectance component is completely suppressed, the continuous rotational symmetry $2\pi/n$ with $n \rightarrow \infty$ meets the requirement for zero specular reflection. Moreover, the condition given by Eq. 5.10 is in many cases a weaker one than the periodicity of the particle arrangement.

Equipped with the knowledge of the possibility to have an effective rotational symmetry for a particular subclass of the disordered patterns, we can now discuss the AR properties of our nanodisk coating from a helicity preservation point of view. To assess the scattering performance of our tailored disordered system from this perspective, we decomposed the backscattered power into its positive (P_+) and negative (P_-) helicity components in the same manner that we did for the periodic system in chapter 3. To make such a decomposition, we illuminated our system with right-handed polarized light. Such illumination corresponds to negative helicity. The scattered field used to perform the helicity decomposition was obtained via the FDTD method.

For wavelengths below $\lambda_c = 577$ nm, the scattering into multiple diffraction orders is allowed for the periodic system. This scattering mixes helicity of the reflected light in this wavelength range (see Fig. 3.3 in Sec. 3.2.2). A continuum of the scattering channels is open for a disordered system, which results in the contribution of both P_+ and P_- to the backscattered power, analogously to the periodic system.

The differences in the optical response of the periodic and disordered system become more pronounced in the wavelength range between $\lambda_0 = 577$ nm and $\lambda_0 = 1000$ nm. In chapter 3 (Fig. 3.3 in Sec. 3.2.2), we have shown that only the zeroth diffraction order is present and all the backscattered power possesses flipped helicity since only P_+ is non-zero and is congruent with reflectance. We note that in chapter 3 we used right-handed circularly polarized plane wave for illumination, corresponding to P_-. We expect the backscattered power to decrease as the degree of helicity preservation of the investigated system increases. Since the structure factor $S(q)$ of the disordered system is still visibly higher than zero (e.g., $S(q = 2\pi/(800 \text{ nm})) \approx 0.48$). The dominating contribution to reflectance is the diffuse component. Hence, the reflected light of the same helicity as the incident light is allowed. Despite the allowed mixture of the powers corresponding to opposite helicities, Fig. 5.6(c) demonstrates that reflectance is still mostly dominated by the backscattered power corresponding to the flipped helicity (P_+). Please be reminded that we used a right-handed circularly polarized plane wave for illumination, corresponding to P_-. The differences between the performance of the ordered and disordered systems lessen when the contribution of the specular component to reflectance to the backscattered light increases. Such an increase of the specular component occurs in the wavelength range starting from $\lambda_0 = 1000$ nm.

For these longer wavelengths, the structure factor $S(q)$ is decaying. For instance, the structure factor at $\lambda_0 = 1200$ nm is $S(q = 2\pi/(1200 \text{ nm})) \approx 0.18)$. Here, we enter the regime for which the disordered system becomes sufficiently stealthy. We can see that the reflection losses are similar at $\lambda_0 = 1200$ nm and $\lambda_0 = 800$ nm. However, at the region around the latter wavelength, the losses are almost exclusively caused by the specular contribution to reflectance. Hence, the backscattered power corresponds to flipped helicity (P_+). In this region, the backscattered power corresponding to helicity

of the incident illumination (P_-) approaches zero in a similar manner it occurred for the periodic system. At longer wavelengths, reflectance of the disordered system has a one-to-one relation to the backscattered power corresponding to helicity. From this result, we can infer that further reduction of $S(q)$ for larger values of q would help extend such one-to-one relation towards shorter wavelengths. Moreover, since the backscattered power corresponding to negative helicity is small for quite a broad spectral range, we can expect that even in the diffusive wavelength region, improving helicity preservation would help to reduce reflectance further.
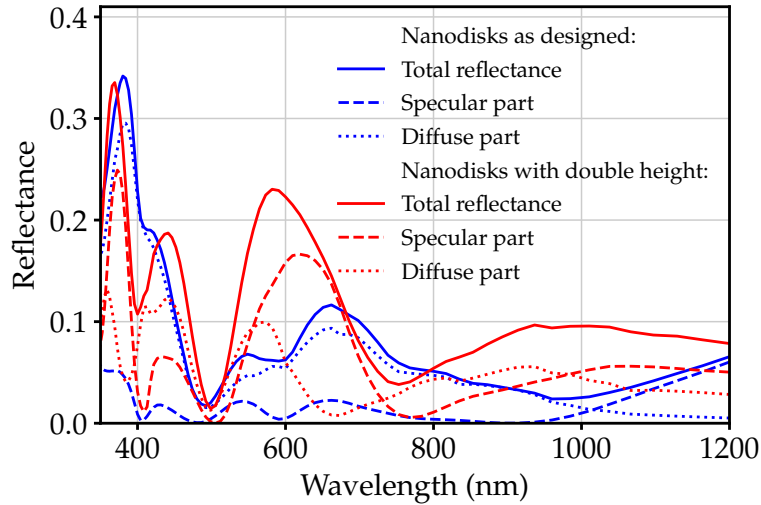

FIGURE 5.7: Calculated reflectance using FDTD of the nanodisks as designed and nanodisks of doubled TiO$_2$ height (nanodisk density of 3.0 μm^{-2}). The nanodisks pattern is identical in both cases and is shown in Figure 5.4. Adapted with permission from [P3]. © 2021 American Chemical Society.

To conclude the discussion of the optical performance of a solar cell with the nanodisk coating, we note that despite the robustness of this performance to the slight changes of the nanodisks' dimensions, a purposeful design of the nanodisks is still essential. To show the importance of keeping the geometrical parameters of the nanodisks close to the optimal design, we performed additional FDTD simulations under periodic boundary conditions for the nanodisks with increased height. The comparison of the structure with nanodisks close to the optimal design, which is extensively discussed in this chapter, to the structure with taller nanodisks is shown in Fig. 5.7. For the nanodisks as designed, we observed a similar behavior to the results from Born's approximation. In contrast, reflectance was significantly increased for the nanodisks with twice the height. This trend was observed for both the diffuse and specular parts, underlining the importance of choosing appropriate disk dimensions.

5.4 Opto-electronic properties of fabricated solar cells

5.4.1 Current-voltage characteristics and quantum efficiencies

Now we will discuss the influence of the nanodisk coating on the opto-electronic properties of the solar cells. For this, we will consider the current-voltage (*I-V*) characteristics of the untreated and coated samples and their external (EQE) and internal (IQE) quantum efficiencies. The respective measurements were conducted at Meyer Burger Research AG in Hauterive, Switzerland. Below is a brief description of the techniques and tools used for characterization:

Current-voltage characteristic:

We measured the *I-V* characteristics of the laser-cut samples under standard test conditions (STC) of $1\,kW/m^2$ mean irradiance and a solar cell temperature in the range of $25\pm1\,°C$ adjusted via calibration. We used the GridTOUCH system allowing for the accurate *I-V* measurement of the busbarless solar cells [141]. This system has 30 current wires and 5 voltage wires on either side, positioned perpendicularly to the solar cell fingers during the measurement, applying equal pressure. We note that the coated solar cells were characterized within one month after separating from the full-size industrial-type solar cells. However, the smaller than typically measured samples caused instabilities in voltage determination due to a mechanical issue with the voltage probe wire. Since the current measurement was not affected, the additional measurements that took place within four months after separation were conducted only for the samples discussed in terms of voltage. We scaled the current to account for handling of the samples, differences in calibration, and the possible degradation of the samples in the time gap between the measurements. The following equation gives the scaling factor a:

$$a = \frac{I_{SC,1m}}{I_{SC,4m}}, \tag{5.11}$$

where indices $i = 1m$ and $i = 4m$ correspond to the time spans since the the separation of the samples from the full-size industrial-type solar cells. We determined the corrected values of the current shown in Fig. 5.8 and Table 5.1 by dividing the measured values by a, which corresponds to an average change (reduction) of the short-circuit current $\Delta_{rel}I_{SC} = 1 - a = 0.64\,\%$ in the three month span between the measurements. This value is slightly above the estimated uncertainty of the current of 0.5 %.

Quantum efficiency:

We used the PV Measurements, Inc. Solar Cell Spectral Response/QE/IPCE Measurement System (Model QEX7) to perform the quantum efficiency measurements with a black back sheet as a background. In this system, light from a xenon arc lamp is filtered by a dual-grating monochromator selecting individual wavelengths before focusing on the sample. The current induced in the sample is amplified and converted to a voltage, which is subsequently measured with signal conditioning equipment and digital signal processing software. For calibration, Si and germanium (Ge) photodiodes are used. We scaled the acquired raw data concerning *I-V* measurements to account for the signal instabilities during EQE measurement. To obtain the scaling factor, we first calculated the short-circuit current density from EQE data $J_{SC,EQE}$ using the following equation:

$$J_{SC,EQE} = q \int_{300\,nm}^{1200\,nm} \phi_{AM1.5G}(\lambda_0) \cdot EQE(\lambda_0)d\lambda_0, \tag{5.12}$$

where q is the electron charge and $\phi_{AM1.5G}$ is the incident photon flux taken from [66]. Then, the scaling factor was determined as:

$$b = J_{SC,EQE}/J_{SC,IV}, \tag{5.13}$$

where the value $J_{SC,IV}$ was deduced from the respective *I-V* characteristic. Subsequently, the scaled EQE_s and IQE_s were determined employing the following equations:

$$EQE_s = EQE/b, \tag{5.14}$$

$$IQE_s = \frac{EQE_s}{1 - R}, \tag{5.15}$$

where reflectance R was measured using the Perkin Elmer Lambda 750 UV/Vis/NIR

spectrophotometer.

Figure 5.8(a) shows the measured *I-V* characteristics of the untreated and coated solar cell samples with the optimal nanodisk density of $3.0\,\mu m^{-2}$, for which we measured the highest increase in I_{SC}. Here, the reference (untreated) sample had an adapted flat ARC since this measurement was mainly done to demonstrate that our deposition process does not negatively influence the electrical properties of the device. The parameters extracted from the measurements of both cells are given in Table 5.1. The short circuit current of the solar cell coated by nanodisks was improved significantly and increased by $14.0\,\%_{rel}$ in comparison to the untreated cell. Since the current at the maximum power point I_{MP} increased upon the nanodisks deposition, the efficiency of the solar cell $\eta = P_{max}/P_{in}$ increased by $10.4\,\%_{rel}$, with the nominal incident power $P_{in} = 1.521\,W$. We found the fill factor $FF = P_{max}/(V_{OC} \cdot I_{SC})$ of the coated solar cell to be $2.7\,\%_{abs}$ lower than the one of the untreated cell. However, the difference in *FF* is not caused by the properties of the nanodisk coating but rather by the higher V_{MP} of the untreated solar cell. This difference can be related to the untreated sample not being subjected to any processing, which could potentially lead to a small reduction in V_{MP} of the sample with the nanodisk coating. Nevertheless, the solar cell parameters determined from the *I-V* characteristics highlight the overall positive effect of the nanodisk coating, boosting short-circuit current and efficiency of the solar cell.

To characterize the spectral behavior of the solar cell coated with the nanodisks concerning the untreated sample with adapted flat ARC, we measured the EQEs and IQEs of these solar cells. The results of these measurements are shown in Fig. 5.8(b). The solar cell with the nanodisk coating showed a significant improvement in EQE in the substantial part of the considered spectral region compared to the untreated reference cell. The EQE of the coated solar cell is lower than that of the untreated cell only in the wavelength region below $\lambda_0 = 500\,nm$. The wavelength region between $\lambda_0 = 350\,nm$ and $\lambda_0 = 500\,nm$ is the only part of the spectrum for which reflectance of the solar cell with the nanodisk coating is higher than the one of the adapted flat ARC reference cell (see Fig. 5.5), thus leading to a higher EQE of the latter. On top of that, the TiO_2 nanodisks introduce some
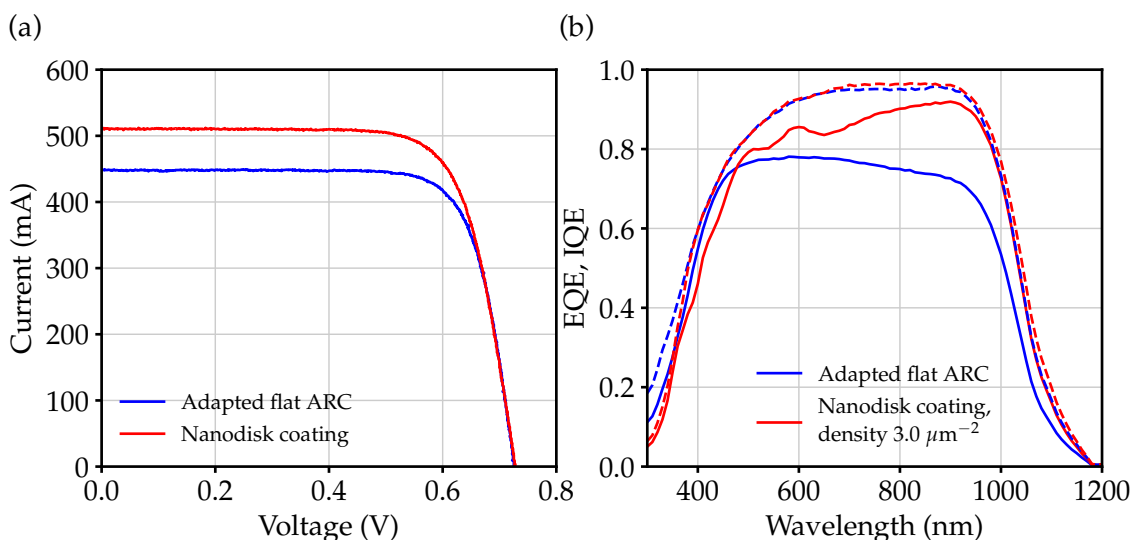

FIGURE 5.8: (a) Current-voltage characteristics of the untreated (adapted flat ARC) sample and sample coated with disordered nanodisks (optimal nanodisk density of $3.0\,\mu m^{-2}$). (b) External (solid lines) and internal (dashed lines) quantum efficiencies for these two samples. Adapted with permission from [P3]. © 2021 American Chemical Society.

TABLE 5.1: Solar cell parameters comparing untreated (adapted flat ARC) and the best nanodisk coated sample, with the estimated uncertainty for the current from repeated measurements of around 0.5 %. Reprinted with permission from [P3]. © 2021 American Chemical Society.

	Untreated sample	Nanodisk coating
$I_{SC,meas}$ (mA)	448	511
J_{SC} (mA/cm^2)	29.5	33.6
V_{OC} (V)	0.726	0.728
I_{MP} (mA)	420	473
V_{MP} (V)	0.598	0.586
P_{max} (W)	0.251	0.277
η (%)	16.5	18.2
FF (%)	77.2	74.5

parasitic absorption for wavelengths below $\lambda_0 = 380$ nm. We further considered the IQEs of these samples to exclude the influence of the reflection losses. In the spectral region starting from $\lambda_0 = 380$ nm, both solar cells show comparable performance within the measurement uncertainty. Only at shorter wavelengths, the IQE of the coated solar cell is lower than the IQE of the untreated cell due to parasitic absorption in the nanodisks.

Figure 5.9(a) shows the comparison of EQEs, IQEs, and reflectances of the coated solar cells with varying nanodisk density. While the spectral features of reflectances and EQEs are very similar for all three nanodisk density values, we can see the gradual shift of these curves, clearly showing the advantage of the optimal density of 3.0 μm^{-2}. We also measured the EQE of the standard flat ARC reference device, for which the ITO layer was 80 nm thick and the minimum of reflectance is at $\lambda_0 = 600$ nm [Fig. 5.9(b)]. The
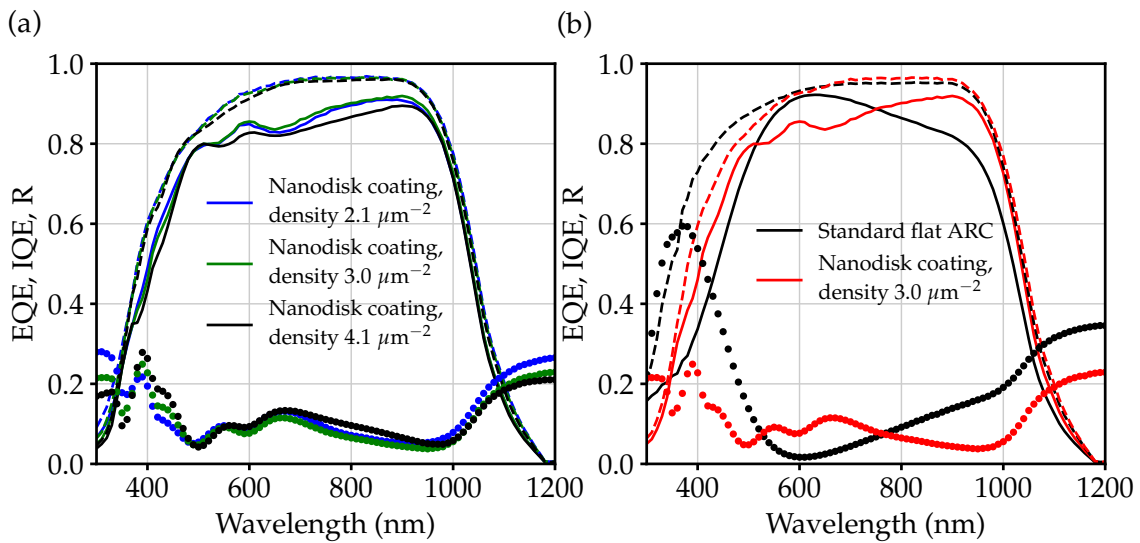

FIGURE 5.9: (a) EQE (solid lines), IQE (dashed lines), and R (circles) of coated cells with varying nanodisk density. (b) EQE (solid lines), IQE (dashed lines), and R (circles) of a coated cell with the optimal nanodisk density compared to a standard flat ARC reference cell. Adapted with permission from [P3]. © 2021 American Chemical Society.

difference between reflectance of the coated cell with the optimal nanodisk density and the standard ARC reference cell leads to the EQE of the former being lower than the EQE of the latter in the wavelength region between $\lambda = 550$ nm and $\lambda = 750$ nm. The EQE of the coated cell is also inferior to the EQE of the standard flat ARC reference cell at the wavelengths below $\lambda_0 = 380$ nm, where the nanodisks introduce some parasitic absorption.

We will now have a look at the IQEs of these two devices. For the wavelengths starting from $\lambda_0 = 550$ nm, the solar cells show comparable performance within the measurement uncertainty. However, we observed that below $\lambda_0 = 550$ nm, the standard flat ARC reference outperforms the coated cell. This performance gap can be partially attributed to the parasitic absorption in the nanodisks in the wavelength region below $\lambda_0 = 380$ nm. However, this can not explain the difference between IQEs in the spectral range from $\lambda_0 = 380$ nm to $\lambda_0 = 550$ nm. Since the IQE of the reference cell with thinner adapted ARC shown in Fig. 5.8(b) was also lower in this region, we suspect that this is an effect of a higher parasitic absorption due to the increased charge carrier concentration of the adapted ITO layer.

5.4.2 Short-circuit current density analysis

Considering that the other characteristics remain mostly intact after the processing steps required for the nanodisk fabrication, the short-circuit current is the most relevant parameter reflecting the performance of our disordered nanodisk coating. If we assume that the IQE of the coated solar cell also remains unchanged compared to an untreated solar cell with $IQE_{ref}(\lambda_0)$ [Fig. 5.8(b)], we can calculate the short-circuit current density using the following equation:

$$ J_{SC} = q \int_{300\,nm}^{1200\,nm} \phi_{AM1.5G}(\lambda_0) IQE_{ref}(\lambda_0)(1 - R(\lambda_0)) d\lambda_0. \tag{5.16} $$

The calculated values of J_{SC} from reflectance curves of the the Born approximation and periodic simulation with equivalent nanodisk density [Fig. 5.6(a)] are given in Table 5.2. As expected, the short-circuit current density is lower when we consider the disordered nanodisk arrangement since reflectance calculated using the Born approximation is higher. If we consider only the J_{SC} contribution for wavelengths $\lambda_0 > 577$ nm, we can deduce that the difference in total J_{SC} is accounted for by differences between reflectance curves in this range. We note that the current loss due to specular reflectance above $\lambda_0 = 577$ nm is comparably low for both cases, while the loss due to diffusive reflectance of the sample with disordered nanodisk arrangement is about -2.01 mA/cm^2. Thus, the main reason behind the difference in the performance of these two arrangements of the nanodisks is the non-zero structure factor components in the low q range.

We will now analyze the change in J_{SC} with varying density of the nanodisks. To calculate the short-circuit current densities for a few nanodisk densities using Eq. 5.16, we used the reflectance spectra like the Born approximation reflectance curve in Fig 5.6(a). However, instead of employing the structure factors obtained from the fabricated samples, we predicted a series of the nanodisk patterns within the bounds of the deposition technique using the algorithm proposed in [130].

Figure 5.10(a) shows the calculated short-circuit current densities of such predicted patterns with varying nanodisk density. As was discussed previously, the highest value of J_{SC} was achieved for a nanodisk density of around 3.0 μm^{-2}. We also show the short-circuit current densities determined from the measurements for comparison. The measured values of J_{SC} for a series of samples with varying nanodisk density are shown in Fig. 5.10(b) (the values for the same cells before and after nanodisk deposition are given).

TABLE 5.2: Calculated current densities and current losses for the disordered na-
nodisk arrangement (reflectance calculated via the first Born approximation) and
periodic arrangement with equivalent nanodisk density (reflectance simulated
via FEM). Reprinted with permission from [P3]. © 2021 American Chemical
Society.

	Current density (mA/cm^2)		Current loss (mA/cm^2) $\lambda_0 > 577$ nm	
	Total	$\lambda_0 > 577$nm	Specular	Diffuse
Born approximation	33.44	25.15	-0.23	-2.01
Periodic simulation	35.42	27.26	-0.30	0
ΔJ_{SC}	-1.98	-2.11	0.07	-2.01

The median short-circuit current density of a series of samples with standard flat ARC
(80 nm ITO layer) is added to Fig. 5.10(a) as a benchmark. The measured values of J_{SC} are
in good agreement with the predicted ones. However, the highest measured short-circuit
current densities are slightly lower than their predicted counterparts. These discrepancies
are caused by the differences between the measured and calculated reflectance spectra
(Fig. 5.5). Additionally, there is some degree of uncertainty in predicting the particle
patterns used to calculate reflectances. For example, the model does not consider any
nanodisks aggregation, which increases the values of $S(q)$ for small q. Thus, we can expect
higher diffuse scattering contributions at wavelengths $\lambda_0 > 600$ nm, and, consequently,
higher current losses for the measurements when compared to the predicted patterns.

For all considered nanodisk densities, the short-circuit current was found to be higher for
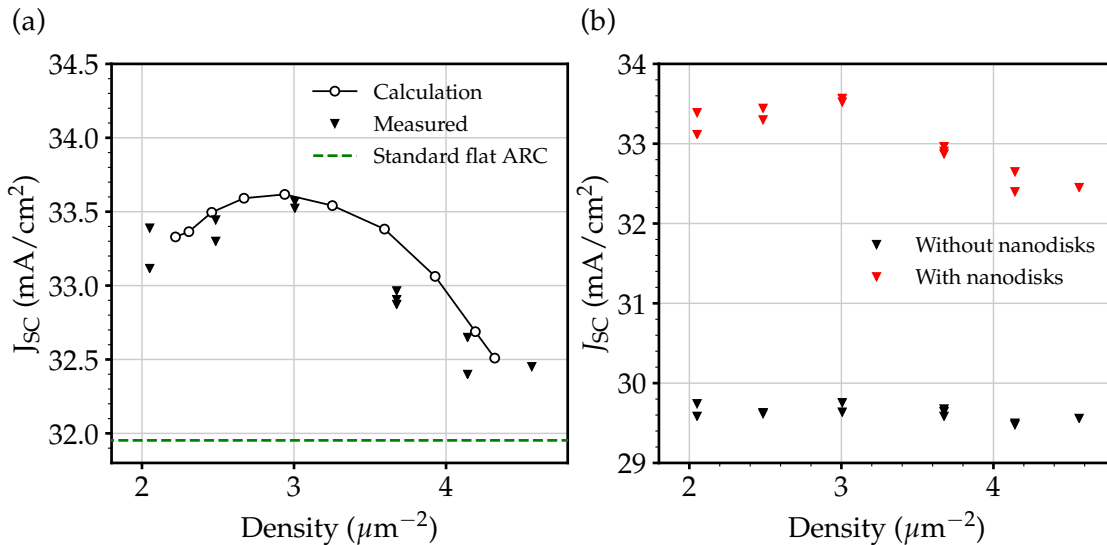
FIGURE 5.10: (a) Short-circuit current density versus nanodisk density for simu-
lated correlated disorder nanodisk patterns (open circles, solid line is a guide
for the eyes) and measured short-circuit current densities (black triangles). Ad-
ditionally, the median short-circuit current density of a series of samples with
standard flat ARC (80 nm ITO layer) is shown (green dashed line). (b) Short-
circuit current density J_{SC} for a series of samples with varying nanodisk density.
The data were obtained for the same solar cells before and after deposition of
the nanodisk coating. Adapted with permission from [P3]. © 2021 American
Chemical Society.

both calculation and measurement when compared to the standard flat ARC reference marked by a green dashed line in Fig. 5.10(a). The highest measured difference for the optimal nanodisk density of 3.0 μm^{-2} was determined to be around 1.6 mA/cm^2 (+5.1 %$_{rel}$). If we consider the change in the short-circuit current density for the solar cells before and after deposition of the nanodisks, the increase is even stronger, amounting to 4.1 mA/cm^2 (+14.0 %$_{rel}$). We use a solar cell with a double ARC as another benchmark, which yields a short-circuit current density increase of 1.5 mA/cm^2 (+4.7 %$_{rel}$) when compared to the standard flat ARC reference. The simulated reflectance spectrum of the cell with such a coating can be found in Appendix B. We note that when comparing the cells with standard and double ARCs, for the former, we used the calculated reflectance (also shown in Appendix B) since the measured reflectance of a standard ARC cell is slightly higher due to the presence of the silver contact fingers. However, introducing encapsulation diminishes the positive effect of a double ARC, while this is not the case for the nanodisks, as was shown in chapter 4.

5.5 Conclusion

We have shown that using a scalable bottom-up deposition technique, a disordered AR coating composed of TiO$_2$ nanodisks can be successfully implemented into standard industrial-type solar cells. Since this technique is robust concerning surface morphology, it does not require special substrate preparation. This robustness and scalability make this technique even more appealing for fabricating disordered nanostructure coatings. Our measurements demonstrated significant backscattering suppression in the wavelength range relevant for solar cells, which manifested itself in a 5.1 %$_{rel}$ improvement of the short-circuit current density when compared to a standard flat ARC reference cell optimized for AM1.5G irradiance.

We supported our experimental results with a theoretical model based on the first Born approximation, which considers the disordered arrangement of the nanodisks. Moreover, we decomposed the backscattered power in terms of its helicity components for a sample illuminated by a plane wave possessing particular handedness (and, by extension, helicity) employing FDTD simulations. Our results showed that the more significant portion of the backscattered light is of flipped helicity concerning helicity of the incident illumination. Even though the disordered nanodisk coating does not approach helicity preservation at the same level as the periodic one discussed in chapter 3 due to non-specular backscattering, its optical performance improves when its stealthiness increases with decreasing structure factor $S(q)$. In particular, $S(q)$ becomes small in the long wavelength region, which leads to reflectance becoming congruent with the backscattered power of the flipped helicity component.

6. Conclusions and Outlook

This work presented a holistic study of a system composed of crystalline silicon (c-Si) rear emitter heterojunction (HJT) solar cell stack coated by anti-reflective (AR) titanium dioxide (TiO_2) nanodisk arrays in different configurations. We will now summarize what we have done on theoretical and experimental sides and discuss a few possible directions for further research.

First, we numerically studied the system with periodically arranged nanodisks designed to improve the AR properties. We approached this system from a helicity preservation point of view. Namely, we based our analysis on two conditions for backscattering suppression: conservation of helicity of the incident light and a sufficiently high degree of discrete rotational symmetry along the illumination direction. Given that generally, one can achieve perfect helicity preservation only for electromagnetically dual systems, which are made of materials with equal electric permittivity and magnetic permeability, we started with a hypothetical system. To show the equal importance of both requirements, we gradually broke either duality or symmetry while the other condition was respected. After confirming that we indeed need both ingredients to suppress backscattering in a broadband manner, we continued with a realistic system corresponding to a c-Si HJT solar cell stack coated with a TiO_2 nanodisk array. For such a system, the helicity preservation condition can be relaxed if the geometrical parameters of the nanoscatterers are tailored appropriately such that the electric and magnetic responses are equal. We observed that after the incident wavelength became equal to or longer than the lattice constant and only the zeroth diffraction order was allowed, only the power associated with flipped helicity component was backscattered. Moreover, at specific wavelengths, for which the backscattering is zero, the system as a whole approached perfect helicity preservation. For this design, we achieved a significant decrease in the current density loss due to reflection. The system with optimal parameters suffered from a current density loss of 1.7 mA·cm^{-2}, while the optimized standard flat reference suffered from a loss of 5.1 mA·cm^{-2}. We also have shown for a simplified system that increasing the rotational symmetry via transitioning from the square to hexagonal lattice can further improve the AR performance of the nanodisk coating. Finally, we fabricated and characterized an optimized TiO_2 nanodisk array on top of a flat c-Si HJT rear emitter solar cell stack via electron beam (e-beam) lithography. Introducing this coating allowed us to improve the AR properties of the cell when compared to both the untreated reference sample and the sample with an optimized flat anti-reflective coating (ARC). We also demonstrated through photoluminescence (PL) imaging that placing our nanodisks on top of the solar cell substrate in an electrically decoupled manner preserves the cell's passivation.

In the next chapter, we analyzed solar modules' annual energy yield (EY) in both mono- and bifacial configurations when AR and light trapping (LT) TiO_2 square nanodisk arrays were introduced at the front and rear solar cell-encapsulation interfaces, respectively. This analysis was performed for c-Si HJT solar modules under realistic radiation conditions for a few locations with contrasting climates. The proposed nanodisk arrays for both cell-encapsulation interfaces were found to have a substantial impact on the light

absorption in the c-Si wafers. Nevertheless, their AR and LT properties were decoupled. The AR nanodisk coating was based on the optimum found in the preceding chapter, albeit it had to be adjusted due to the change of the surrounding medium from air to encapsulation, yielding a rather small individual nanodisk size and lattice constant. The LT nanodisk had considerably larger dimensions of the individual scatterers, thus allowing for efficient scattering into multiple scattering directions. We have shown that introducing an encapsulation on the top and rear sides of the cell coated with TiO_2 nanodisks does not annihilate their positive effect on the optical properties of the system. We considered the c-Si absorber thickness in the range between thin photovoltaics (PV) and conventional c-Si PV. In this range, the texturing of the c-Si wafers becomes challenging. When the c-Si wafer thickness was reduced down to 5 μm, the relative increase of the annual EY of the mono- and bifacial solar modules reached up to 23.3 $\%_{rel}$ and 43.0 $\%_{rel}$, respectively, when the nanodisk arrays were introduced. This improvement was comparable for all considered locations. We also compared the power output of the solar modules with nanodisks to the state-of-the-art solar modules with random pyramidal texture at one location and a few characteristic c-Si wafer thicknesses. Even though the latter outperforms the solar modules with nanodisk gratings, the proposed designs prove to be an excellent alternative when thinner c-Si wafers are considered.

Next, we studied the system with a tailored disordered arrangement of AR nanodisks. To fabricate the coated c-Si HJT rear emitter solar cells, we employed a scalable colloid-based deposition technique. We have shown that this fabrication method can be applied to industrial-type solar cells. This technique allowed us to avoid using polished wafers, which was the requirement for fabricating the cells with periodic nanodisk arrangement employing e-beam lithography. We characterized the fabricated devices concerning their opto-electronic properties by measuring their current-voltage (I-V) characteristics and external (EQE) and internal (IQE) quantum efficiencies. We compared their performance to the performance of the untreated reference and the standard flat optimized reference devices. Our measurements demonstrated significant backscattering suppression in the wavelength range relevant for PV devices. The improvement of the short-circuit current density, when compared to a standard flat ARC reference cell optimized for the AM1.5G irradiance, amounted to 5.1 $\%_{rel}$. We also supported our experimental results with a theoretical model based on the first Born approximation, which allowed us to consider the disordered nature of the nanodisk coating. Moreover, we analyzed the optical properties of the cell with disordered nanodisk coating from the helicity preservation point of view. Our results have shown that the more significant portion of the backscattered light is of flipped helicity with respect to helicity of the incident illumination. The disordered nanodisk ARC did not approach helicity preservation at some wavelengths as the periodic one. However, due to non-specular backscattering, its optical performance improved with decreasing structure factor. In particular, the structure factor was small at longer wavelengths, which led to reflectance becoming equivalent to the backscattered power of the flipped helicity component.

To circle back to the question we posed at the very beginning of this thesis, *what did we add to already existing knowledge when it comes to the improvement of the AR properties of solar cells when employing dielectric nanostructures?*

We used a new approach to the analysis of the backscattering performance of AR dielectric nanostructure coatings based on fundamental symmetry in electromagnetism, i.e., conservation of helicity. We demonstrated that the strict requirement for the system to be electromagnetically dual could be relaxed by tuning the nanodisk dimensions such that the electric and magnetic responses are equal, thus providing guidelines for future designs of ARCs for solar cell applications. Moreover, while for a general disordered system, we can not exactly apply the concept of discrete rotational symmetry,

for an appropriately tailored pattern, we can speak of an effective continuous rotational symmetry. We linked the backscattering suppression by the systems containing both ordered and tailored disordered nanodisks to the ability of a given system to preserve helicity, albeit for the latter one-to-one correlation occurred exclusively for the long wavelength range. We have also shown that while the periodic nanodisks have initially shown superior AR properties compared to tailored disordered nanodisks based on the numerical analysis, the fabrication of respective designs led to an opposite outcome. The nanofabrication approach we used for the periodic system had constraints that led to a reduction of optical performance improvement compared to the forecast performance.

Most importantly, while many nanophotonic concepts relying on the periodic arrangement of the scatterers were proposed over the years, at the moment, the most promising results were published only for sub-centimeter sized samples [129]. In contrast, for a disordered system, we observed a more decisive reduction of measured reflectance. The scalability of this approach and its robustness towards substrate surface morphology brings this fabrication technique very close to industrial requirements. These results highlight the importance of approaching the design of the ARCs from a few angles since it gives more flexibility concerning pushing the nanophotonic structures towards practical applications. Additionally, the annual EY analysis implies that our AR nanodisks can potentially be integrated into the solar module.

Regarding the future developments along the lines of results presented in this thesis, one can consider coated nanodisks for further suppression of the backscattered power component corresponding to flipped helicity. Additional improvement of the AR properties is suggested by the fact that core-shell spherical designs experience a boost of their helicity preservation properties compared to homogeneous spheres [142]. Such coated nanodisks should also allow to enhance the response strength by aligning together multipolar resonances beyond the dipoles [143]. Such alignment of different resonances can subsequently increase the bandwidth of helicity preservation [99, 144]. This approach can be applied to both periodic and disordered arrangements of the nanodisks. Moreover, for the disordered case, one can investigate the influence of nanodisk aggregation on the optical properties of the coated solar cell.

Concerning the fabrication methods, feasible next steps will be different for the systems with ordered and tailored disordered nanodisk coatings. For the former, instead of slow and expensive e-beam lithography, one can consider employing nanoimprint lithography, which shows promise in terms of scalability [145]. In the case of fabrication of tailored disordered nanodisk patterns, one can attempt to decrease the structure factor further. For instance, aggregation of particles during colloidal deposition is a major reason for increased structure factor values, hence improved control over aggregation should further boost the optical performance.

Concerning transition to the solar module level, the next natural step would be to fabricate mini-modules based on solar cells coated with disordered nanodisk designs and evaluate their response under standard test conditions and realistic irradiation conditions.

Bibliography

[P1] E. Slivina, A. Abass, D. Bätzner, B. Strahm, C. Rockstuhl, and I. Fernandez-Corbaton, "Insights into Backscattering Suppression in Solar Cells from the Helicity-Preservation Point of View", *Physical Review Applied*, vol. 12, no. 5, p. 054 003, 2019.

[P2] E. Slivina, D. Bätzner, R. Schmager, M. Langenhorst, J. Lehr, U. W. Paetzold, U. Lemmer, and C. Rockstuhl, "Annual energy yield of mono- and bifacial silicon heterojunction solar modules with high-index dielectric nanodisk arrays as anti-reflective and light trapping structures", *Optics Express*, vol. 29, no. 21, pp. 34 494–34 509, 2021.

[P3] P. M. Piechulla, E. Slivina, D. Bätzner, I. Fernandez-Corbaton, P. Dhawan, R. B. Wehrspohn, A. N. Sprafke, and C. Rockstuhl, "Anti-reflective huygens' metasurface with correlated disorder made from high-index disks implemented into silicon heterojunction solar cells", *ACS Photonics*, vol. 8, no. 12, pp. 3476–3485, 2021.

[P4] P. M. Piechulla, B. Fuhrmann, E. Slivina, C. Rockstuhl, R. B. Wehrspohn, and A. N. Sprafke, "Tailored light scattering through hyperuniform disorder in self-organized arrays of high-index nanodisks", *Advanced Optical Materials*, vol. 9, no. 17, p. 2 100 186, 2021.

[1] *Adoption of the Paris Agreement,* `https://unfccc.int/resource/docs/2015 /cop21/eng/l09r01.pdf`, United Nations, 2015.

[2] V. Masson-Delmotte, P. Zhai, H.-O. Pörtner, D. Roberts, J. Skea, P. R. Shukla, A. Pirani, W. Moufouma-Okia, C. Péan, R. Pidcock, *et al.*, "Special Report on the impacts of global warming of 1.5 °C", IPCC, 2018.

[3] "Climate Change 2021: The Physical Science Basis", IPCC, 6th Assessment Report, Aug. 2021.

[4] "Snapshot of Global PV markets", International Energy Agency, Photovoltaic Power Systems Programme, Apr. 2021.

[5] N. M. Haegel, H. Atwater, T. Barnes, C. Breyer, A. Burrell, Y.-M. Chiang, S. De Wolf, B. Dimmler, D. Feldman, S. Glunz, J. C. Goldschmidt, D. Hochschild, R. Inzunza, I. Kaizuka, B. Kroposki, S. Kurtz, S. Leu, R. Margolis, K. Matsubara, A. Metz, W. K. Metzger, M. Morjaria, S. Niki, S. Nowak, I. M. Peters, S. Philipps, T. Reindl, A. Richter, D. Rose, K. Sakurai, R. Schlatmann, M. Shikano, W. Sinke, R. Sinton, B. Stanbery, M. Topič, W. Tumas, Y. Ueda, J. van de Lagemaat, P. Verlinden, M. Vetter, E. Warren, M. Werner, M. Yamaguchi, and A. W. Bett, "Terawatt-scale photovoltaics: Transform global energy", *Science*, vol. 364, pp. 836–838, 2019.

[6] K. Sharma, V. Sharma, and S. Sharma, "Dye-sensitized solar cells: Fundamentals and current status", *Nanoscale Research Letters*, vol. 13, no. 381, pp. 1–46, 2018.

[7] L. Duan and A. Uddin, "Progress in stability of organic solar cells", *Advanced Science*, vol. 7, no. 11, p. 1 903 259, 2020.

[8] J. Y. Kim, J.-W. Lee, H. S. Jung, H. Shin, and N.-G. Park, "High-efficiency perovskite solar cells", *Chemical Reviews*, vol. 120, no. 15, pp. 7867–7918, 2020.

[9] Y. Rong, Y. Hu, A. Mei, H. Tan, M. I. Saidaminov, S. I. Seok, M. D. McGehee, E. H. Sargent, and H. Han, "Challenges for commercializing perovskite solar cells", *Science*, vol. 361, no. 6408, eaat8235, Sep. 2018.

[10] Y. Galagan, "Perovskite Solar Cells: Toward Industrial-Scale Methods", *The Journal of Physical Chemistry Letters*, vol. 9, no. 15, pp. 4326–4335, 2018.

[11] C. Case, N. Beaumont, and D. Kirk, "Industrial insights into perovskite photovoltaics", *ACS Energy Letters*, vol. 4, no. 11, pp. 2760–2762, 2019.

[12] *Oxford PV perovskite-silicon tandem solar cell efficinecy record*, `https://www.oxfordpv.com/news/oxford-pv-perovskite-solar-cell-achieves-28-efficiency`, 2018.

[13] S. Maldonado, "The Importance of New "Sand-to-Silicon" Processes for the Rapid Future Increase of Photovoltaics", *ACS Energy Letters*, vol. 5, no. 11, pp. 3628–3632, 2020.

[14] J. C. Goldschmidt, L. Wagner, R. Pietzcker, and L. Friedrich, "Technological learning for resource efficient terawatt scale photovoltaics", *Energy & Environmental Science*, vol. 14, no. 10, pp. 5147–5160, 2021.

[15] Z. Liu, S. E. Sofia, H. S. Laine, M. Woodhouse, S. Wieghold, I. M. Peters, and T. Buonassisi, "Revisiting thin silicon for photovoltaics: A technoeconomic perspective", *Energy & Environmental Science*, vol. 13, no. 1, pp. 12–23, 2020.

[16] W. Shockley and H. J. Queisser, "Detailed Balance Limit of Efficiency of p-n Junction Solar Cells", en, *Journal of Applied Physics*, vol. 32, no. 3, pp. 510–519, 1961.

[17] A. Richter, M. Hermle, and S. W. Glunz, "Reassessment of the Limiting Efficiency for Crystalline Silicon Solar Cells", *IEEE Journal of Photovoltaics*, vol. 3, no. 4, pp. 1184–1191, 2013.

[18] K. Yoshikawa, H. Kawasaki, W. Yoshida, T. Irie, K. Konishi, K. Nakano, T. Uto, D. Adachi, M. Kanematsu, H. Uzu, and K. Yamamoto, "Silicon heterojunction solar cell with interdigitated back contacts for a photoconversion efficiency over 26%", *Nature Energy*, vol. 2, no. 5, pp. 1–8, 2017.

[19] H. Seidel, L. Csepregi, A. Heuberger, and H. Baumgärtel, "Anisotropic Etching of Crystalline Silicon in Alkaline Solutions: I . Orientation Dependence and Behavior of Passivation Layers", *Journal of The Electrochemical Society*, vol. 137, no. 11, pp. 3612–3626, 1990.

[20] P. Papet, O. Nichiporuk, A. Kaminski, Y. Rozier, J. Kraiem, J.-F. Lelievre, A. Chaumartin, A. Fave, and M. Lemiti, "Pyramidal texturing of silicon solar cell with TMAH chemical anisotropic etching", *Solar Energy Materials and Solar Cells*, vol. 90, no. 15, pp. 2319–2328, 2006.

[21] K. Kim, S. Dhungel, S. Jung, D. Mangalaraj, and J. Yi, "Texturing of large area multi-crystalline silicon wafers through different chemical approaches for solar cell fabrication", *Solar Energy Materials and Solar Cells*, vol. 92, no. 8, pp. 960–968, 2008.

[22] "International Technology Roadmap for Photovoltaic (ITRPV)", VDMA Photovoltaic Equipment, 12th edition, Apr. 2021.

[23] K.-M. Han and J.-S. Yoo, "Wet-texturing process for a thin crystalline silicon solar cell at low cost with high efficiency", *Journal of the Korean Physical Society*, vol. 64, no. 8, pp. 1132–1137, 2014.

[24] X. Tan, W. Yan, Y. Tu, and C. Deng, "Small pyramidal textured ultrathin crystalline silicon solar cells with double-layer passivation", *Optics Express*, vol. 25, no. 13, pp. 14 725–14 731, 2017.

[25] A. A. A. Omer, Z. He, S. Hong, Y. Chang, J. Yu, S. Li, W. Ma, W. Liu, W. El Kolaly, and R. Chen, "Ultra-thin silicon wafers fabrication and inverted pyramid texturing based on cu-catalyzed chemical etching", *Silicon*, vol. 13, no. 2, pp. 351–359, 2021.

[26] E. C. Garnett, B. Ehrler, A. Polman, and E. Alarcon-Llado, "Photonics for Photovoltaics: Advances and Opportunities", *ACS Photonics*, vol. 8, no. 1, pp. 61–70, 2021.

[27] V. Neder, S. L. Luxembourg, and A. Polman, "Efficient colored silicon solar modules using integrated resonant dielectric nanoscatterers", *Applied Physics Letters*, vol. 111, no. 7, p. 073 902, 2017.

[28] S. A. Mann and E. C. Garnett, "Resonant nanophotonic spectrum splitting for ultrathin multijunction solar cells", *ACS Photonics*, vol. 2, no. 7, pp. 816–821, 2015.

[29] K. Baryshnikova, M. Petrov, V. Babicheva, and P. Belov, "Plasmonic and silicon spherical nanoparticle antireflective coatings", *Scientific Reports*, vol. 6, no. 22136, pp. 1–11, 2016.

[30] P. Yu, J. Wu, S. Liu, J. Xiong, C. Jagadish, and Z. M. Wang, "Design and fabrication of silicon nanowires towards efficient solar cells", *Nano Today*, vol. 11, no. 6, pp. 704–737, 2016.

[31] J. He, Z. Yang, P. Liu, S. Wu, P. Gao, M. Wang, S. Zhou, X. Li, H. Cao, and J. Ye, "Enhanced Electro-Optical Properties of Nanocone/Nanopillar Dual-Structured Arrays for Ultrathin Silicon/Organic Hybrid Solar Cell Applications", *Advanced Energy Materials*, vol. 6, no. 8, p. 1 501 793, 2016.

[32] H. Savin, P. Repo, G. Von Gastrow, P. Ortega, E. Calle, M. Garín, and R. Alcubilla, "Black silicon solar cells with interdigitated back-contacts achieve 22.1% efficiency", *Nature Nanotechnology*, vol. 10, no. 7, pp. 624–628, 2015.

[33] K. X. Wang, Z. Yu, V. Liu, Y. Cui, and S. Fan, "Absorption Enhancement in Ultrathin Crystalline Silicon Solar Cells with Antireflection and Light-Trapping Nanocone Gratings", *Nano Letters*, vol. 12, no. 3, pp. 1616–1619, 2012.

[34] O. Isabella, R. Vismara, D. Linssen, K. Wang, S. Fan, and M. Zeman, "Advanced light trapping scheme in decoupled front and rear textured thin-film silicon solar cells", *Solar Energy*, vol. 162, pp. 344–356, 2018.

[35] K. Catchpole and A. Polman, "Plasmonic solar cells", *Optics Express*, vol. 16, no. 26, pp. 21 793–21 800, 2008.

[36] M. A. Green and S. Pillai, "Harnessing plasmonics for solar cells", *Nature Photonics*, vol. 6, no. 3, pp. 130–132, 2012.

[37] V. E. Ferry, L. A. Sweatlock, D. Pacifici, and H. A. Atwater, "Plasmonic nanostructure design for efficient light coupling into solar cells", *Nano Letters*, vol. 8, no. 12, pp. 4391–4397, 2008.

[38] S. Morawiec, M. J. Mendes, F. Priolo, and I. Crupi, "Plasmonic nanostructures for light trapping in thin-film solar cells", *Materials Science in Semiconductor Processing*, vol. 92, pp. 10–18, 2019.

[39] C. E. Disney, S. Pillai, and M. A. Green, "The impact of parasitic loss on solar cells with plasmonic nano-textured rear reflectors", *Scientific Reports*, vol. 7, no. 12826, pp. 1–10, 2017.

[40] V. E. Ferry, A. Polman, and H. A. Atwater, "Modeling light trapping in nanostructured solar cells", *ACS Nano*, vol. 5, no. 12, pp. 10 055–10 064, 2011.

[41] P. Spinelli, M. A. Verschuuren, and A. Polman, "Broadband omnidirectional antireflection coating based on subwavelength surface Mie resonators", *Nature Communications*, vol. 3, no. 692, pp. 1–5, 2012.

[42] P. Spinelli and A. Polman, "Light trapping in thin crystalline Si solar cells using surface Mie scatterers", *IEEE Journal of Photovoltaics*, vol. 4, no. 2, pp. 554–559, 2014.

[43] P. Spinelli, F. Lenzmann, A. Weeber, and A. Polman, "Effect of EVA Encapsulation on Antireflection Properties of Mie Nanoscatterers for c-Si Solar Cells", *IEEE Journal of Photovoltaics*, vol. 5, no. 2, pp. 559–564, 2015.

[44] C. van Lare, F. Lenzmann, M. A. Verschuuren, and A. Polman, "Dielectric scattering patterns for efficient light trapping in thin-film solar cells", *Nano Letters*, vol. 15, no. 8, pp. 4846–4852, 2015.

[45] M. Elshorbagy, K. Abdel-Hady, H. Kamal, and J. Alda, "Broadband anti-reflection coating using dielectric Si_3N_4 nanostructures. Application to amorphous-Si-H solar cells", *Optics Communications*, vol. 390, pp. 130–136, 2017.

[46] A. Cordaro, J. Van De Groep, S. Raza, E. F. Pecora, F. Priolo, and M. L. Brongersma, "Antireflection high-index metasurfaces combining Mie and Fabry-Pérot resonances", *ACS Photonics*, vol. 6, no. 2, pp. 453–459, 2019.

[47] S. Yalamanchili, E. Verlage, W.-H. Cheng, K. T. Fountaine, P. R. Jahelka, P. A. Kempler, R. Saive, N. S. Lewis, and H. A. Atwater, "High Broadband Light Transmission for Solar Fuels Production Using Dielectric Optical Waveguides in TiO_2 Nanocone Arrays", *Nano Letters*, vol. 20, no. 1, pp. 502–508, 2020.

[48] J. Grandidier, R. A. Weitekamp, M. G. Deceglie, D. M. Callahan, C. Battaglia, C. R. Bukowsky, C. Ballif, R. H. Grubbs, and H. A. Atwater, "Solar cell efficiency enhancement via light trapping in printable resonant dielectric nanosphere arrays", *physica status solidi (a)*, vol. 210, no. 2, pp. 255–260, 2013.

[49] P. Spinelli and A. Polman, "Light Trapping in Thin Crystalline Si Solar Cells Using Surface Mie Scatterers", *IEEE Journal of Photovoltaics*, vol. 4, no. 2, pp. 554–559, 2014.

[50] Y. J. Donie, M. Smeets, A. Egel, F. Lentz, J. B. Preinfalk, A. Mertens, V. Smirnov, U. Lemmer, K. Bittkau, and G. Gomard, "Light trapping in thin film silicon solar cells via phase separated disordered nanopillars", *Nanoscale*, vol. 10, no. 14, pp. 6651–6659, 2018.

[51] D. J. Jackson, *Classical Electrodynamics*, 3rd edition. John Wiley & Sons, Inc., 1999.

[52] L. Novotny and B. Hecht, *Principles of Nano-Optics*, 2nd edition. Oxford University Press, 2012.

[53] M. Born, E. Wolf, A. B. Bhatia, P. C. Clemmow, D. Gabor, A. R. Stokes, A. M. Taylor, P. A. Wayman, and W. L. Wilcock, *Principles of Optics: Electromagnetic Theory of Propagation, Interference and Diffraction of Light*, 7th ed. Cambridge University Press, 1999.

[54] I. Fernandez-Corbaton, "Helicity and duality symmetry in light matter interactions: Theory and applications", PhD thesis, Macquarie University, Faculty of Science, Engineering, Department of Physics, and Astronomy, 2014.

[55] I. Fernandez-Corbaton and G. Molina-Terriza, "Role of duality symmetry in transformation optics", *Physical Review B*, vol. 88, no. 8, p. 085 111, 2013.

[56] I. Bialynicki-Birula, "Photon wave function", *Progress in Optics*, vol. 36, pp. 245–294, 1996.

[57] I. Bialynicki-Birula and Z. Bialynicka-Birula, "The role of the Riemann-Silberstein vector in classical and quantum theories of electromagnetism", *Journal of Physics A: Mathematical and Theoretical*, vol. 46, no. 5, p. 053 001, 2013.

[58] I. Fernandez-Corbaton, "Forward and backward helicity scattering coefficients for systems with discrete rotational symmetry", *Optics Express*, vol. 21, no. 24, pp. 29 885–29 893, 2013.

[59] A. H. M. Smets, K. Jäger, O. Isabella, R. A. C. M. M. van Swaaij, and M. Zeman, *Solar Energy: The Physics and Engineering of Photovoltaic Conversion, Technologies and Systems*. UIT Cambridge Ltd., 2016.

[60] P. Würfel and U. Würfel, *Physics of Solar Cells: From Basic Principles to Advaned Concepts*, 3rd edition. Wiley-VCH, 2016.

[61] S. De Wolf, A. Descoeudres, Z. C. Holman, and C. Ballif, "High-efficiency Silicon Heterojunction Solar Cells: A Review", *Green*, vol. 2, no. 1, pp. 7–24, 2012.

[62] A. Descoeudres, Z. C. Holman, L. Barraud, S. Morel, S. De Wolf, and C. Ballif, ">21% Efficient Silicon Heterojunction Solar Cells on n- and p-Type Wafers Compared", *IEEE Journal of Photovoltaics*, vol. 3, no. 1, pp. 83–89, 2013.

[63] D. Macdonald and L. J. Geerligs, "Recombination activity of interstitial iron and other transition metal point defects in p- and n-type crystalline silicon", *Applied Physics Letters*, vol. 85, no. 18, pp. 4061–4063, 2004.

[64] Yibin Bai, J. Phillips, and A. Barnett, "The roles of electric fields and illumination levels in passivating the surface of silicon solar cells", *IEEE Transactions on Electron Devices*, vol. 45, no. 8, pp. 1784–1790, 1998.

[65] M. Bivour, H. Steinkemper, J. Jeurink, S. Schröer, and M. Hermle, "Rear Emitter Silicon Heterojunction Solar Cells: Fewer Restrictions on the Optoelectrical Properties of Front Side TCOs", *Energy Procedia*, vol. 55, pp. 229–234, 2014.

[66] C. A. Gueymard, D. Myers, and K. Emery, "Proposed reference irradiance spectra for solar energy systems testing", *Solar Energy*, vol. 73, no. 6, pp. 443–467, 2002.

[67] *IEC 60904-3, Measurement principles for terrestrial photovoltaic (PV) solar devices with reference spectral irradiance data*, 2019.

[68] H. Nagel, A. G. Aberle, and R. Hezel, "Optimised Antireflection Coatings for Planar Silicon Solar Cells using Remote PECVD Silicon Nitride and Porous Silicon Dioxide", *Progress in Photovoltaics: Research and applications*, vol. 7, no. 4, pp. 245–260, 1999.

[69] S.-Y. Lien, D.-S. Wuu, W.-C. Yeh, and J.-C. Liu, "Tri-layer antireflection coatings $(SiO_2/SiO_2 –TiO_2/TiO_2)$ for silicon solar cells using a sol–gel technique", *Solar Energy Materials and Solar Cells*, vol. 90, no. 16, pp. 2710–2719, 2006.

[70] H. Shimomura, Z. Gemici, R. E. Cohen, and M. F. Rubner, "Layer-by-layer-assembled high-performance broadband antireflection coatings", *ACS Applied Materials and Interfaces*, vol. 2, no. 3, pp. 813–820, 2010.

[71] X. Yan, N. Chen, F. B. Suhaimi, L. Zhang, X. Gong, X. Zhang, and S. Duttagupta, "Design, fabrication, and analysis of double-layer antireflection coatings (ARC) for industrial bifacial n-type crystalline silicon solar cells", *Applied Optics*, vol. 58, no. 15, E1–E6, 2019.

[72] C. Schinke, P. Christian Peest, J. Schmidt, R. Brendel, K. Bothe, M. R. Vogt, I. Kröger, S. Winter, A. Schirmacher, S. Lim, H. T. Nguyen, and D. MacDonald, "Uncertainty analysis for the coefficient of band-to-band absorption of crystalline silicon", *AIP Advances*, vol. 5, no. 6, p. 067 168, 2015.

[73] R. B. Wehrspohn, U. Rau, and A. Gombert, *Photon Management in Solar Cells*. Wiley-VCH, 2015.

[74] C. S. Solanki and H. K. Singh, *Anti-reflection and Light Trapping in c-Si Solar Cells*, ser. Green Energy and Technology. Singapore: Springer Singapore, 2017.

[75] M. A. Green, "Lambertian light trapping in textured solar cells and light-emitting diodes: Analytical solutions", *Progress in Photovoltaics: Research and Applications*, vol. 10, no. 4, pp. 235–241, 2002.

[76] E. Yablonovitch, "Statistical ray optics", *Journal of the Optical Society of America*, vol. 72, no. 7, pp. 899–907, 1982.

[77] H. Kim, J. Park, and B. Lee, *Fourier modal method and its applications in computational nanophotonics*. CRC Press, 2012.

[78] U. S. Inan and R. A. Marshall, *Numerical Electromagnetics: The FDTD Method*. Cambridge University Press, 2011.

[79] Y. Shi, W. Shin, and S. Fan, "Multi-frequency finite-difference frequency-domain algorithm for active nanophotonic device simulations", *Optica*, vol. 3, no. 11, pp. 1256–1259, 2016.

[80] J.-M. Jin, *The Finite Element Method in Electromagnetics*, 3rd edition. Wiley, 2014.

[81] P. Monk, *Finite element methods for Maxwell's equations*. Oxford University Press, 2003.

[82] J. Pomplun, S. Burger, L. Zschiedrich, and F. Schmidt, "Adaptive finite element method for simulation of optical nano structures", *Physica Status Solidi B*, vol. 244, no. 10, pp. 3419–3434, 2007.

[83] J.-P. Berenger, "A perfectly matched layer for the absorption of electromagnetic waves", *Journal of Computational Physics*, vol. 114, no. 2, pp. 185–200, 1994.

[84] *JCMsuite parameter reference*, `https://www.docs.jcmwave.com/JCMsuite/html/ParameterReference/2a798650cd7175e5990b42811e7248a3.html?version=3.18.9`.

[85] *EYcalc - energy yield calculator for multi-junction solar modules with realistic irradiance data and textured interfaces*, `https://github.com/PerovskitePV/EYcalc`.

[86] R. Schmager, M. Langenhorst, J. Lehr, U. Lemmer, B. S. Richards, and U. W. Paetzold, "Methodology of energy yield modelling of perovskite-based multi-junction photovoltaics", *Optics Express*, vol. 27, no. 8, A507–A523, 2019.

[87] J. Eisenlohr, N. Tucher, O. Höhn, H. Hauser, M. Peters, P. Kiefel, J. C. Goldschmidt, and B. Bläsi, "Matrix formalism for light propagation and absorption in thick textured optical sheets", *Optics Express*, vol. 23, no. 11, A502–A518, 2015.

[88] F. I. Baida and A. Belkhir, *Finite difference time domain method for grating structures*, 2012.

[89] K. Yee, "Numerical solution of initial boundary value problems involving maxwell's equations in isotropic media", *IEEE Transactions on antennas and propagation*, vol. 14, no. 3, pp. 302–307, 1966.

[90]   A. F. Oskooi, D. Roundy, M. Ibanescu, P. Bermel, J. D. Joannopoulos, and S. G. Johnson, "Meep: A flexible free-software package for electromagnetic simulations by the FDTD method", *Computer Physics Communications*, vol. 181, no. 3, pp. 687–702, 2010.

[91]   M. Kerker, D.-S. Wang, and C. Giles, "Electromagnetic scattering by magnetic spheres", *Journal of the Optical Society of America A*, vol. 73, no. 6, pp. 765–767, 1983.

[92]   I. V. Lindell, A. Sihvola, P. Yla-Oijala, and H. Wallen, "Zero backscattering from self-dual objects of finite size", *IEEE Transactions on Antennas Propagation*, vol. 57, no. 9, pp. 2725–2731, 2009.

[93]   M. Nieto-Vesperinas, R. Gomez-Medina, and J. J. Saenz, "Angle-suppressed scattering and optical forces on submicrometer dielectric particles", *Journal of the Optical Society of America A*, vol. 28, no. 1, pp. 54–60, 2011.

[94]   X. Zambrana-Puyalto, I. Fernandez-Corbaton, M. Juan, X. Vidal, and G. Molina-Terriza, "Duality symmetry and Kerker conditions", *Optics Letters*, vol. 38, no. 11, pp. 1857–1859, 2013.

[95]   T. Coenen, F. B. Arango, A. F. Koenderink, and A. Polman, "Directional emission from a single plasmonic scatterer", *Nature Communications*, vol. 5, no. 3250, pp. 1–8, 2014.

[96]   R. Alaee, R. Filter, D. Lehr, F. Lederer, and C. Rockstuhl, "A generalized Kerker condition for highly directive nanoantennas", *Optics Letters*, vol. 40, no. 11, pp. 2645–2648, 2015.

[97]   J. M. Geffrin, B. García-Cámara, R. Gómez-Medina, P. Albella, L. S. Froufe-Pérez, C. Eyraud, A. Litman, R. Vaillon, F. González, M. Nieto-Vesperinas, J. J. Sáenz, and F. Moreno, "Magnetic and electric coherence in forward- and back-scattered electromagnetic waves by a single dielectric subwavelength sphere", *Nature Communications*, vol. 3, p. 1171, 2012.

[98]   S. Person, M. Jain, Z. Lapin, J. J. Sáenz, G. Wicks, and L. Novotny, "Demonstration of zero optical backscattering from single nanoparticles", *Nano Letters*, vol. 13, no. 4, pp. 1806–1809, 2013.

[99]   M. I. Abdelrahman, C. Rockstuhl, and I. Fernandez-Corbaton, "Broadband suppression of backscattering at optical frequencies using low permittivity dielectric spheres", *Scientific Reports*, vol. 7, no. 14762, pp. 1–8, 2017.

[100] I. Fernandez-Corbaton, X. Zambrana-Puyalto, N. Tischler, X. Vidal, M. L. Juan, and G. Molina-Terriza, "Electromagnetic duality symmetry and helicity conservation for the macroscopic Maxwell's equations", *Physical Review Letters*, vol. 111, no. 6, p. 060 401, 2013.

[101] I. Kim, D. S. Jeong, W. S. Lee, W. M. Kim, T.-S. Lee, D.-K. Lee, J.-H. Song, J.-K. Kim, and K.-S. Lee, "Silicon nanodisk array design for effective light trapping in ultrathin c-Si", *Optics Express*, vol. 22, no. 106, A1431–A1439, 2014.

[102] I. Staude, A. E. Miroshnichenko, M. Decker, N. T. Fofang, S. Liu, E. Gonzales, J. Dominguez, T. S. Luk, D. N. Neshev, I. Brener, and Y. Kivshar, "Tailoring directional scattering through magnetic and electric resonances in subwavelength silicon nanodisks", *ACS Nano*, vol. 7, no. 9, pp. 7824–7832, 2013.

[103] K. E. Chong, L. Wang, I. Staude, A. R. James, J. Dominguez, S. Liu, G. S. Subramania, M. Decker, D. N. Neshev, I. Brener, and Y. S. Kivshar, "Efficient polarization-insensitive complex wavefront control using Huygens metasurfaces based on dielectric resonant meta-atoms", *ACS Photonics*, vol. 3, no. 4, pp. 514–519, 2016.

[104] *Filmetrics database, TiO₂ Rutile,* `https://www.filmetrics.com/refractive-index-database`.

[105] Z. C. Holman, M. Filipič, A. Descoeudres, S. De Wolf, F. Smole, M. Topič, and C. Ballif, "Infrared light management in high-efficiency silicon heterojunction and rear-passivated solar cells", *Journal of Applied Physics*, vol. 113, no. 1, p. 013 107, 2013.

[106] A. B. Evlyukhin, C. Reinhardt, and B. N. Chichkov, "Multipole light scattering by nonspherical nanoparticles in the discrete dipole approximation", *Physical Review B*, vol. 84, p. 235 429, 23 2011.

[107] M. Singh, R. Santbergen, I. Syifai, A. Weeber, M. Zeman, and O. Isabella, "Comparing optical performance of a wide range of perovskite/silicon tandem architectures under real-world conditions", *Nanophotonics*, p. 20 200 643, 2021.

[108] M. T. Hörantner and H. J. Snaith, "Predicting and optimising the energy yield of perovskite-on-silicon tandem solar cells under real world conditions", *Energy & Environmental Science*, vol. 10, pp. 1983–1993, 9 2017.

[109] N. Tucher, O. Höhn, J. N. Murthy, J. C. Martinez, M. Steiner, A. Armbruster, E. Lorenz, B. Bläsi, and J. C. Goldschmidt, "Energy yield analysis of textured perovskite silicon tandem solar cells and modules", *Optics Express*, vol. 27, no. 20, A1419–A1430, 2019.

[110] J. Lehr, M. Langenhorst, R. Schmager, F. Gota, S. Kirner, U. Lemmer, B. S. Richards, C. Case, and U. W. Paetzold, "Energy yield of bifacial textured perovskite/silicon tandem photovoltaic modules", *Solar Energy Materials and Solar Cells*, vol. 208, p. 110 367, 2020.

[111] F. Gota, M. Langenhorst, R. Schmager, J. Lehr, and U. W. Paetzold, "Energy yield advantages of three-terminal perovskite-silicon tandem photovoltaics", *Joule*, vol. 4, no. 11, pp. 2387–2403, 2020.

[112] M. Jošt, E. Köhnen, A. B. Morales-Vilches, B. Lipovšek, K. Jäger, B. Macco, A. Al-Ashouri, J. Krč, L. Korte, B. Rech, R. Schlatmann, M. Topič, B. Stannowski, and S. Albrecht, "Textured interfaces in monolithic perovskite/silicon tandem solar cells: Advanced light management for improved efficiency and energy yield", *Energy & Environmental Science*, vol. 11, no. 12, pp. 3511–3523, 2018.

[113] T. C. R. Russell, R. Saive, A. Augusto, S. G. Bowden, and H. A. Atwater, "The Influence of Spectral Albedo on Bifacial Solar Cells: A Theoretical and Experimental Study", *IEEE Journal of Photovoltaics*, vol. 7, no. 6, pp. 1611–1618, 2017.

[114] Y. Jiang, S. Pillai, and M. A. Green, "Realistic Silver Optical Constants for Plasmonics", *Scientific Reports*, vol. 6, no. 30605, pp. 1–7, 2016.

[115] K. R. McIntosh, J. N. Cotsell, J. S. Cumpston, A. W. Norris, N. E. Powell, and B. M. Ketola, "An optical comparison of silicone and EVA encapsulants for conventional silicon PV modules: A ray-tracing study", in *2009 34th IEEE Photovoltaic Specialists Conference (PVSC)*, Philadelphia, PA, USA: IEEE, 2009, pp. 000 544–000 549.

[116] J. M. Siqueiros, R. Machorro, and L. E. Regalado, "Determination of the optical constants of MgF₂ and ZnS from spectrophotometric measurements and the classical oscillator method", *Applied Optics*, vol. 27, no. 12, pp. 2549–2553, 1988.

[117] K. Jäger, G. Köppel, M. Hammerschmidt, S. Burger, and C. Becker, "On accurate simulations of thin-film solar cells with a thick glass superstrate", *Optics Express*, vol. 26, no. 2, A99–A107, 2018.

[118] Z. C. Holman, A. Descoeudres, L. Barraud, F. Z. Fernandez, J. P. Seif, S. De Wolf, and C. Ballif, "Current Losses at the Front of Silicon Heterojunction Solar Cells", *IEEE Journal of Photovoltaics*, vol. 2, no. 1, pp. 7–15, 2012.

[119] M. C. Peel, B. L. Finlayson, and T. A. McMahon, "Updated world map of the Köppen-Geiger climate classification", *Hydrology and Earth System Sciences*, vol. 11, no. 5, pp. 1633–1644, 2007.

[120] L. Stevens, N. Tucher, O. Höhn, H. Hauser, C. Müller, and B. Bläsi, "Broadband antireflection Mie scatterers revisited—a solar cell and module analysis", *Optics Express*, vol. 27, no. 8, A524–A535, 2019.

[121] A. Oskooi, P. A. Favuzzi, Y. Tanaka, H. Shigeta, Y. Kawakami, and S. Noda, "Partially disordered photonic-crystal thin films for enhanced and robust photovoltaics", *Applied Physics Letters*, vol. 100, no. 18, p. 181 110, 2012.

[122] M.-C. van Lare and A. Polman, "Optimized Scattering Power Spectral Density of Photovoltaic Light-Trapping Patterns", *ACS Photonics*, vol. 2, no. 7, pp. 822–831, 2015.

[123] F. Pratesi, M. Burresi, F. Riboli, K. Vynck, and D. S. Wiersma, "Disordered photonic structures for light harvesting in solar cells", *Optics Express*, vol. 21, no. 103, A460–A468, 2013.

[124] N. Tavakoli, R. J. Spalding, G. Gkantzounis, C. Wan, R. Röhrich, E. Kontoleta, M. Florescu, R. Sapienza, F. Koenderink, and E. A. Lladó, "Hyperuniform designs for enhanced light trapping in ultrathin single and tandem solar cells (Conference Presentation)", in *Photonics for Solar Energy Systems VIII*, 2020, 113660A.

[125] S. Torquato, "Hyperuniform States of Matter", *Physical Reports*, vol. 745, pp. 1–95, 2018.

[126] M. A. Klatt, J. Lovrić, D. Chen, S. C. Kapfer, F. M. Schaller, P. W. A. Schönhöfer, B. S. Gardiner, A.-S. Smith, G. E. Schröder-Turk, and S. Torquato, "Universal hidden order in amorphous cellular geometries", *Nature Communications*, vol. 10, no. 811, pp. 1–9, 2019.

[127] T. Bottein, T. Wood, T. David, J. B. Claude, L. Favre, I. Berbézier, A. Ronda, M. Abbarchi, and D. Grosso, ""Black" Titania Coatings Composed of Sol–Gel Imprinted Mie Resonators Arrays", *Advanced Functional Matererials*, vol. 27, no. 2, p. 1 604 924, 2017.

[128] M. A. Verschuuren, M. Megens, Y. Ni, H. van Sprang, and A. Polman, "Large area nanoimprint by substrate conformal imprint lithography (SCIL)", *Advanced Optical Technologies*, vol. 6, no. 3-4, pp. 243–264, 2017.

[129] D. Visser, D. Y. Chen, Y. Désières, A. P. Ravishankar, and S. Anand, "Embossed Mie resonator arrays composed of compacted TiO_2 nanoparticles for broadband anti-reflection in solar cells", *Scientific Reports*, vol. 10, no. 1, p. 12 527, 2020.

[130] P. M. Piechulla, L. Muehlenbein, R. B. Wehrspohn, S. Nanz, A. Abass, C. Rockstuhl, and A. Sprafke, "Fabrication of Nearly-Hyperuniform Substrates by Tailored Disorder for Photonic Applications", *Advanced Optical Matererials*, vol. 6, no. 7, p. 1 701 272, 2018.

[131] G. A. Battiston, R. Gerbasi, A. Gregori, M. Porchia, S. Cattarin, and G. A. Rizzi, "PECVD of amorphous TiO2 thin films: Effect of growth temperature and plasma gas composition", *Thin Solid Films*, vol. 371, no. 1, pp. 126–131, 2000.

[132] W. G. Lee, S. I. Woo, J. C. Kim, S. H. Choi, and K. H. Oh, "Preparation and properties of amorphous TiO_2 thin films by plasma enhanced chemical vapor deposition", *Thin Solid Films*, vol. 237, no. 1, pp. 105–111, 1994.

[133] A.-K. Volk, N. Tucher, J. Seiffe, H. Hauser, M. Zimmer, B. Blasi, M. Hofmann, and J. Rentsch, "Honeycomb Structure on Multi-crystalline Silicon Al-BSF Solar Cell With 17.8% Efficiency", *IEEE Journal of Photovoltaics*, vol. 5, no. 4, pp. 1027–1033, 2015.

[134] P. Piechulla, J. Seiffe, M. Hofmann, J. Rentsch, and R. Preu, "Increased ion energies for texturing in a high-throughput plasma tool", in *Proc. of 26th European Photovoltaic Solar Energy Conference and Exhibition*, Hamburg, 2011.

[135] J. Keller, "Stochastic equations and wave propagation in random media", *Proceedings of Symposia in Applied Mathematics*, vol. 16, pp. 145–170, 1964.

[136] L. Mandel and E. Wolf, *Optical Coherence and Quantum Optics*. Cambridge University Press, 1995.

[137] H. Liu and S. J. Paddison, "Direct calculation of the x-ray structure factor of ionic liquids", *Physical Chemistry Chemical Physics*, vol. 18, no. 16, pp. 11 000–11 007, 2016.

[138] O. U. Uche, F. H. Stillinger, and S. Torquato, "Constraints on collective density variables: Two dimensions", *Physical Review E*, vol. 70, no. 4, p. 046 122, 2004.

[139] S. Torquato, O. U. Uche, and F. H. Stillinger, "Random sequential addition of hard spheres in high Euclidean dimensions", *Physical Review E*, vol. 74, no. 6, p. 061 308, 2006.

[140] S. Yu, C.-W. Qiu, Y. Chong, S. Torquato, and N. Park, "Engineered disorder in photonics", *Nature Review Materials*, vol. 6, no. 3, pp. 226–243, 2021.

[141] N. Bassi, C. Clerc, Y. Pelet, J. Hiller, V. Fakhfouri, C. Droz, M. Despeisse, J. Levrat, A. Faes, and D. Bätzner, "GridTouch: Innovative solution for accurate IV measurement of busbarless cells in production and laboratory environments", in *Proc. of 29th European Photovoltaic Solar Energy Conference and Exhibition*, 2014, pp. 1180–1185.

[142] A. Rahimzadegan, C. Rockstuhl, and I. Fernandez-Corbaton, "Core-shell particles as building blocks for systems with high duality symmetry", *Physical Review Applied*, vol. 9, p. 054 051, 5 2018.

[143] Z. Ruan and S. Fan, "Superscattering of light from subwavelength nanostructures", *Physical Review Letters*, vol. 105, p. 013 901, 1 2010.

[144] M. I. Abdelrahman, H. Saleh, I. Fernandez-Corbaton, B. Gralak, J.-M. Geffrin, and C. Rockstuhl, "Experimental demonstration of spectrally broadband Huygens sources using low-index spheres", *APL Photonics*, vol. 4, no. 2, p. 020 802, 2019.

[145] V. J. Einck, M. Torfeh, A. McClung, D. E. Jung, M. Mansouree, A. Arbabi, and J. J. Watkins, "Scalable Nanoimprint Lithography Process for Manufacturing Visible Metasurfaces Composed of High Aspect Ratio TiO_2 Meta-Atoms", *ACS Photonics*, vol. 8, no. 8, pp. 2400–2409, 2021.

[146] G. E. Jellison and F. A. Modine, "Parameterization of the optical functions of amorphous materials in the interband region", *Applied Physics Letters*, vol. 69, no. 3, pp. 371–373, 1996.

[147] B.-M. Meiners, S. Holinski, P. Schäfer, S. Hohage, and D. Borchert, "Investigation of anti-reflection-coating stacks for silicon heterojunction solar cells", in *Proceedings of 29th European Photovoltaic Solar Energy Conference and Exhibition*, 2014.

[148] K. R. McIntosh and S. C. Baker-Finch, "OPAL 2: Rapid optical simulation of silicon solar cells", in *2012 38th IEEE Photovoltaic Specialists Conference*, 2012, pp. 000 265–000 271.
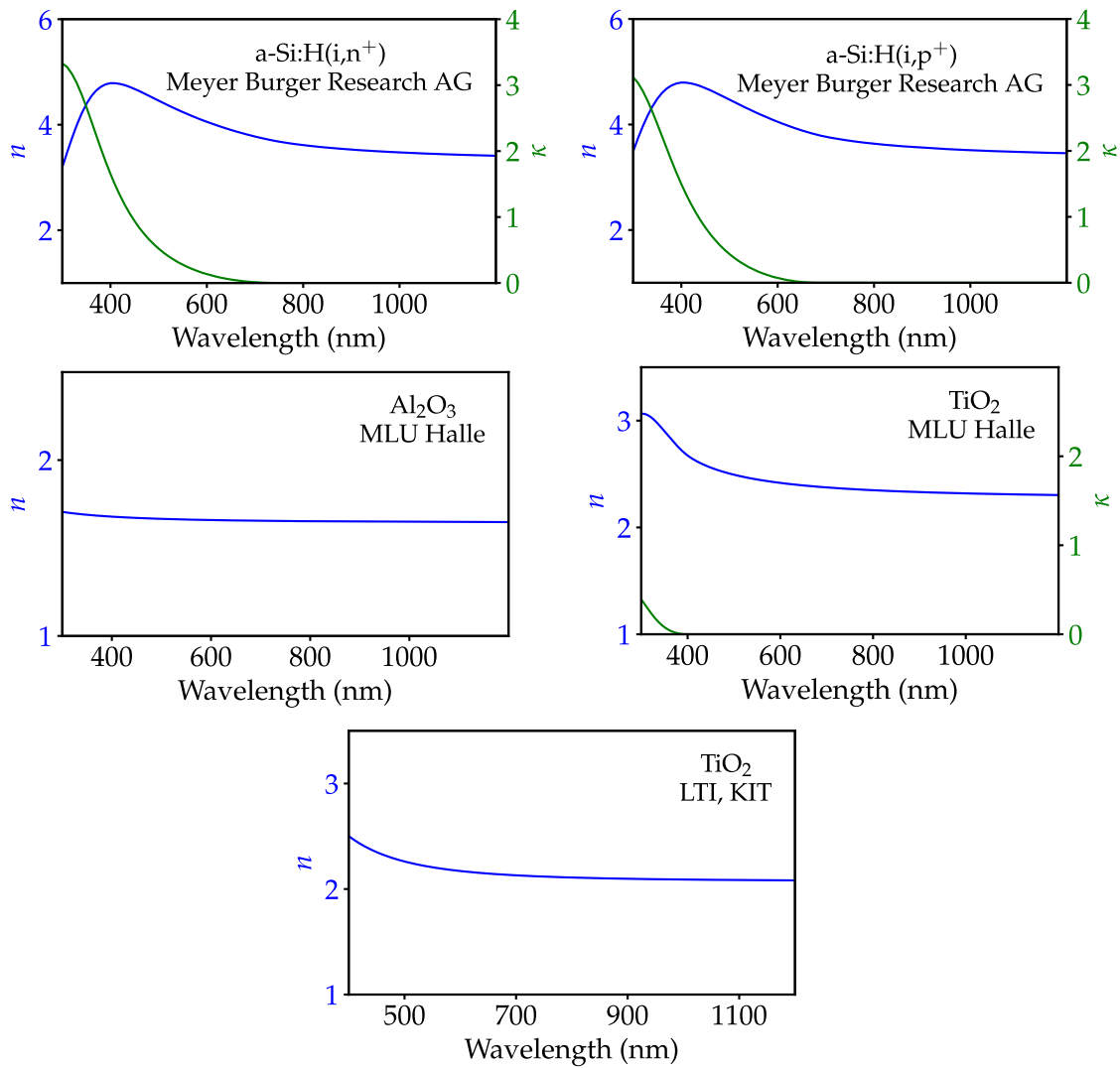
Appendix

A Material properties

FIGURE A.1: Refractive indices of materials used throughout the thesis, which were determined employing ellipsometry. The institutions where the respective measurements were done are indicated in the legends. The measurd data for a-Si:H (Meyer Burger Research AG) and TiO₂ (MLU Halle) were fitted using Tauc-Lorentz model [146]. For Al₂O₃ (MLU Halle), absorption was neglected and the ellipsometric data was fitted to the Cauchy equation.

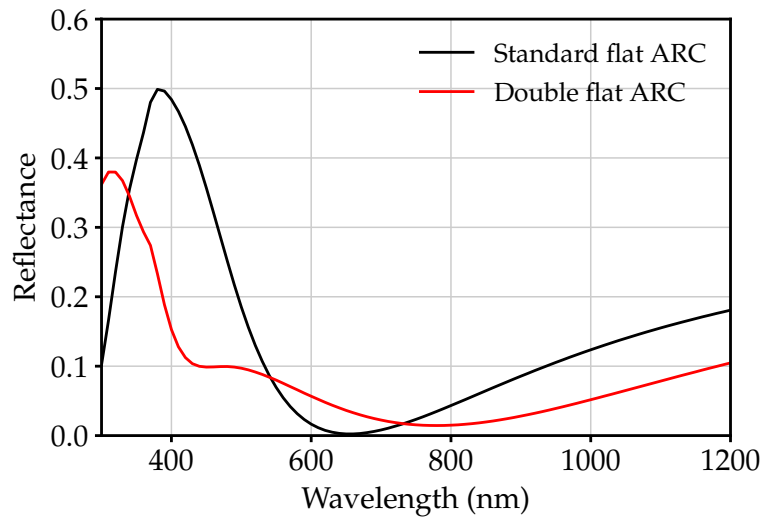# B Comparison of double flat ARC with standard flat ARC

FIGURE B.2: Calculated reflectance for a c-Si HJT solar cell coated with a standard flat ARC (80 nm ITO [105]) and a double flat ARC (95 nm MgF$_2$ [116] on top of 65 nm ITO). The design of the double flat ARC was inspired by the work of Meiners *et al.* [147]. The calculation as well as the optimization of film thicknesses were performed using the OPAL 2 tool [148].

Acknowledgements

First of all, I would like to thank Prof. Carsten Rockstuhl for giving me an opportunity to take on such an exciting and challenging project. I would also like to sincerely thank him for all the support, insightful discussions, and patience while guiding me through this PhD project over the last years. He also proofread this thesis, for which I am very grateful.

I would also like to thank Prof. Ulrich W. Paetzold for being the second referee of this doctoral thesis. I also had the pleasure to collaborate with the members of his group on a few projects. In this respect, I would like to extend my thanks to Dr. Malte Langenhorst, Dr. Raphael Schmager, and Dr. Somayeh (Sara) Moghadamzadeh, who contributed to this joint work.

I also want to thank Dr. Aimi Abass, who supervised me in the very beginning of this doctoral project and was always there to answer my questions. I warmly thank Dr. Ivan Fernandez-Corbaton, who introduced me to the concepts central to my thesis and always was open for discussions. His enthusiasm for the topic always charged me with a positive attitude and motivated me to carry on with my research.

I would also like to thank the staff of Meyer Burger Research AG in Hauterive (Neuchâtel), Switzerland, where I have spent fruitful one and a half years. I always felt welcome there and very much enjoyed the stay in Neuchâtel. I want to thank Dr. Benjamin Strahm, who welcomed me to Meyer Burger when I had just started my PhD journey. Special thanks go to Dr. Derk Bätzner who supervised me while I was in Hauterive. He was always open to scientific (and also more lighthearted) discussions, especially regarding the practical aspects of my research. Derk also was very kind to proofread some parts of this thesis. I want to thank the whole staff of Meyer Burger for the support they gave for my experimental work and the readiness with which they helped me realize my projects. I would also like to warmly thank Dr. Walter Frammelsberger and Ludovic Vuithier. They made me feel at home in Neuchâtel during my multiple visits.

Next, I would like to thank our experimental partners from the Martin-Luther-University Halle-Wittenberg, particularly Dr. Peter M. Piechulla and Dr. Alexander N. Sprafke. It was a pleasure to work with them in the last months of my PhD. I have expanded my knowledge quite a lot during the many conversations we had regarding our joint project.

I thank all the group members at KIT for having a great time not only during insightful discussions but many lunch breaks, dinners, bike rides, and whatnot. We shared many nice moments and laughs during these years, which helped me to forget the stress and pressure accumulating in tough moments. I want to also thank my office mates, Prerak Dhawan and Aris Lamprianidis. It was nice to share a room with you, even though in the past year we were not there all together. Special thanks go to our B(ike) team, who made the worst Covid days more bearable.

Last but not least, I want to thank my closest friends and family. I thank my mother, Alexandra, for always being there for me with supporting words but also a harsh dose of reality and criticism (which motivated me even more during the hard times). I thank

my closest friends Sveta, Nana, and Yana for always being able to make me laugh and believing in me no matter how hard I got on myself. Finally, I thank Antoine for his love and support, and especially for his patience during many tough moments I had in the past year.